Fabrication and Characterisation of Ultrafast Direct Laser Written Waveguides

Leilei Huang

Jesus College

University of Oxford

A thesis submitted for the degree of

Doctor of Philosophy

Trinity 2015

//
Abstract

A novel ultrafast direct laser writing (DLW) system using adaptive optics is proposed and demonstrated. This system has the potential to generate high-quality three-dimensional (3D) optical waveguides and components. The experimental setup and procedures for the DLW process are studied, after which various optical waveguides are fabricated in different transparent materials. The resulting waveguides are characterised by the measurement of the near-field laser coupling profiles in combination with optical microscopy techniques. Quantum random number generation (QRNG) and the potential application of the DLW technique in quantum information is also discussed.

To completely understand the fabrication procedures for the DLW system, the experimental equipment and effects of different fabrication parameters are studied and analysed. With the use of a liquid-crystal spatial light modulator (SLM) in the DLW system, dynamic control of phase modulation can be provided to correct aberrations adaptively. An SLM can also make the cross-sectional profile of the written waveguides more circular and facilitate the fabrication of more complex 3D structures. Experiments reveal that the shape of the focal spot can be improved dramatically with adaptive optics, resulting in higher-quality optical waveguides.

The refractive-index information of the written waveguides and their optical properties are measured using the propagation-mode near-field method

(PMNFM). Simulation results and experimental measurements of a commercial single-mode fiber and a waveguide sample are demonstrated and compared. Quantitative phase measurement is also applied via the transport of intensity equation (TIE) to monitor the refractive-index change during fabrication. The propagation losses of the waveguides are measured and discussed.

Different optical waveguides are fabricated using DLW in fused silica, potassium dihydrogen phosphate (KDP), and lithium niobate ($LiNbO_3$) crystals. Different materials have different characteristics and properties, requiring different fabrication parameters and resulting in waveguides exhibiting different properties. Waveguides at various depths are demonstrated both with and without effects of adaptive optics. Experimental results indicate great improvements in the quality of the written waveguides after aberration correction. With an understanding of the optical properties of the straight waveguides using the characterisation methods, modelling and fabrication of bend waveguides and y-splitters are presented and studied.

A high-speed QRNG system is also demonstrated in this thesis, with potential implementation using the DLW technique for a more compact and stable system. Finally, the possibility of the DLW fabrication of complex 3D optical components and their applications are discussed for future work.

I would like to dedicate this thesis to my loving parents,

husband, son and daughter.

Acknowledgements

First, I would like to express my sincere gratitude and appreciation to my supervisor Prof. Frank Payne for his inspiration, vision, guidance and encouragement during my study.

I am very grateful to Dr. Patrick Salter for his creative advice, helpful comments and encouragement concerning my experiment.

I would like to express my thanks to Prof. Martin Booth for his great suggestions and help during my project.

Thanks to my collaborators, Dr. Michal Karpiński, Dr. Brian Smith, Youqi Nie, Prof. Jun Zhang, and Prof. JianWei Pan, for the interesting discussions and sharing ideas in the last few years.

I am also grateful to all previous and current members of the communication group and the scanning optical microscopy group for their indispensable support and valuable friendships.

Last but not least, I would like to thank my parents for their spiritual support and encouragement. I am deeply grateful to my husband for his love, understanding and patience over the past ten years.

Publications

[1] L. Huang and P. S. Salter and F. Payne and M. J. Booth, "Aberration correction for direct laser written waveguides in a transverse geometry", *Opt. Express*, vol. 24, no. 10, pp. 10565, May 2016.

[2] L. Huang, P. S. Salter, M. Karpiński, B. Smith, F. Payne, and M. J. Booth, "Waveguide fabrication in KDP crystals with femtosecond laser pulses", *Applied Physics A*, vol. 118, no. 3, pp. 831, March 2015.

[3] Y.-Q. Nie, L. Huang, Y. Liu, F. Payne, J. Zhang, and J.-W. Pan, "The generation of 68 Gbps quantum random number by measuring laser phase fluctuations", *Review of Scientific Instruments*, vol. 86, no. 6, pp. 063105, June 2015.

[4] L. Huang and F. Payne, "Determination of the Equivalent Step Index of Direct Laser Written Waveguides", *The XXII International Workshop on Optical Wave & Waveguide Theory and Numerical Modelling*, June 2014.

[5] P. S. Salter, A. Jesacher, L. Huang, X. Liu, M. Baum, I. Alexeev, and M. J. Booth, "Structural analysis of direct laser written waveguides", *Proc. SPIE 8968, Laser-based Micro- and Nanoprocessing VIII*, March 2014.

[6] M. Karpiński, L. Huang, P. S. Salter, B. Smith, F. Payne, and M. J. Booth, "Second Harmonic Generation of Optical Waveguides in KDP Crystals", *Manuscript in Preparation.*

Contents

1 Introduction **1**

1.1 Motivation 1

1.2 Project Summary 4

1.3 Dissertation Organization 5

2 Background on Waveguide Fabrication and Characterisation **8**

2.1 Refractive-Index Modification 8

2.2 Fabrication Methods and Parameters 11

2.3 Optical Devices Fabricated by Ultrafast Lasers 16

2.4 Characterisation of Optical Waveguides 21

2.4.1 Geometric Measurement 22

2.4.2 Coupling into Waveguides 23

2.4.3 Refractive-Index Measurement 24

2.4.4 Propagation Loss 28

3 Ultrafast Direct Laser Writing System with Adaptive Optics **34**

3.1 Introduction 34

3.2 Spatial Light Modulator (SLM) 36

3.2.1 Slit Beam-shaping 36

3.2.2 Beam Steering and Splitting 40

3.2.3 Adaptive Aberration Correction 48

3.3 Direct Laser Writing Setup and Procedures 51
3.3.1 Experimental System Setup with the SLM 51
3.3.2 Experimental Procedures 52
3.4 Aberration Correction Sensing Methods Using an SLM 59
3.4.1 Shack–Hartmann Wavefront Sensing 59
3.4.2 Plasma Emission Aberration Sensing 64
3.5 Conclusion 66

4 Characterisation of Optical Waveguides 68

4.1 Introduction 69
4.2 Cross-section Measurement 69
4.3 Propagation-Mode Near-Field Method (PMNFM) 70
4.3.1 Theoretical Study 71
4.3.2 Simulation Results 72
4.4 PMNFM Experimental Measurements 75
4.4.1 Experimental Setup 75
4.4.2 Reduction of Noise 76
4.4.3 Experimental Results 77
4.5 Equivalent-Step-Index (ESI) Profile 80
4.6 Quantitative Phase Microscopy 83
4.7 Insertion and Propagation Loss 86
4.8 Conclusion 90

5 Fabrication of Optical Waveguides in Fused Silica 93

5.1 Introduction 94
5.2 Waveguide Fabrication at Various Depths 94
5.3 Design and Fabrication of Y-splitters 104
5.3.1 Bend Losses 105

5.3.2 Modelling of Y-splitters 110
5.3.3 Fabrication of Y-splitters 111
5.4 Parallel Fabrication 114
5.5 Conclusion 116

6 Ultrafast Laser Fabrication in KDP Crystal 117

6.1 Introduction 118
6.2 Experimental Setup 119
6.3 Experimental Results and Discussion 120
6.3.1 Type I Waveguide 122
6.3.2 Type II Waveguide 125
6.4 Ultrafast Laser Fabrication in $LiNbO_3$ 130
6.5 Conclusion 133

7 Quantum Random Number Generation 134

7.1 Introduction 135
7.2 Experimental Realisation 137
7.3 Analysis and Data Post-processing 140
7.4 Randomness Test 146
7.5 Conclusion 149

8 Summary 151

8.1 Conclusion 151
8.2 Outlook 153

Bibliography 155

List of Figures

2.1 Type I and type II waveguides 12

2.2 Direct laser writing geometries 15

2.3 Circular and elliptical Gaussian focus 15

2.4 Schematic diagram of a typical DLW system 16

2.5 First demonstration of a 1×2 y-splitter fabricated using DLW 17

2.6 Schematic diagrams of a 1×8 optical splitter fabricated using DLW . 17

2.7 A 3D 1×4 splitter fabricated using DLW 19

2.8 Type I and type II waveguides fabricated in $LiNbO_3$ using DLW . . . 20

2.9 A type I y-splitter fabricated in $LiNbO_3$ using DLW 21

2.10 Observation of fabricated waveguides under the microscope 23

2.11 Mode coupling between two waveguides 23

2.12 End-fire coupling and butt coupling 24

2.13 Experimental setup for the reflection method 25

2.14 Schematic diagrams of the interferometric slab method 27

2.15 Measurement results of a single-mode fiber using the PMNFM 29

2.16 Major sources of propagation loss 30

2.17 Scattered light measurement 32

3.1 Schematic diagram of the wavefront modification on an SLM 37

3.2 Phase modulation imitating a blazed grating on an SLM 37

3.3 Fabrication focus with and without slit beam-shaping 38

3.4 Direct laser writing with slit beam-shaping 39
3.5 Phase pattern imitating a physical slit on an SLM 40
3.6 SLM phase patterns and their resulting focus dimensions 41
3.7 Single beam-steering using the phase grating 43
3.8 Beam splitting using multiple phase gratings 44
3.9 Beam splitting with gratings partially blocked 44
3.10 Schematic diagram of the multi foci generation using an SLM 45
3.11 A 3×3 multi-foci array using a phase hologram 47
3.12 A hexagonal multi-foci array using a phase hologram 47
3.13 Schematic diagram of a DLW system with an SLM 51
3.14 Experimental setup of a DLW system with an SLM 53
3.15 Lab layout of a DLW system 54
3.16 The SLM cross phase pattern for alignment 55
3.17 Main control user interface of the Labview program for DLW 56
3.18 Different user interfaces of the Labview program for DLW 57
3.19 Cross-sectional and top-down views of nonworking waveguides 59
3.20 Schematic diagram of the Shack–Hartmann sensor 60
3.21 SLM with the Shack–Hartmann array 60
3.22 SLM with the whole aperture 61
3.23 Shack–Hartmann array with astigmatism aberration 62
3.24 Effect of phase wrapping and randomised phase pattern 62
3.25 Different shapes of small apertures applied on an SLM screen 63
3.26 Aberration correction result 63
3.27 Plasma emission intensity changes with different Zernike modes . . . 65
3.28 Plasma emission sensing for different Zernike modes 66

4.1 Different cross-sections with different SLM phase patterns 70
4.2 Flowchart of the PMNFM simulation 73

4.3 Refractive-index simulation for the step and graded-index fiber 74
4.4 Intensity measurement setup for refractive-index evaluation 75
4.5 Refractive-index calculation of an SM600 fiber using the original PMNFM 76
4.6 Single and multiple CCD images 78
4.7 Curve-fitting of the intensity distribution of an SM600 fiber 79
4.8 Refractive-index calculation of an SM600 fiber using the improved PM-NFM 80
4.9 Refractive-index calculation of a laser-written waveguide using the improved PMNFM 81
4.10 Refractive-index calculation of an SM600 fiber using the ESI method 83
4.11 Refractive-index calculation of a laser-written waveguide using the ESI method 84
4.12 Experimental setup and measurement using quantitative phase microscopy 86
4.13 CCD images and the ROI of the waveguide input and output 88
4.14 Waveguide-coupling setup 90
4.15 Calculation of mode-coupling efficiency 91

5.1 Schematic of the aberration generated during laser fabrication 96
5.2 Relationship between 1/s and NA 97
5.3 SLM phase pattern for waveguide fabrication 98
5.4 Refractive-index calculation of an SM600 fiber using the ESI method 99
5.5 Waveguides at different depths without aberration correction 100
5.6 Waveguides at different depths with aberration correction 101
5.7 Position offsets of waveguides 102
5.8 The near-field intensity distributions of the fabricated waveguides . . 103
5.9 Refractive-index calculation of an aberration-corrected waveguide using the PMNFM 104

5.10 Bend radius (mm) vs. loss (dB/cm) using the Mercue's modelling . . 106
5.11 Bend radius (mm) vs. loss (dB/cm) using FIMMWAVE 107
5.12 Bend loss vs. radius simulation at a wavelength of 800 nm 108
5.13 Bend loss vs. radius simulation at a wavelength of 600 nm 109
5.14 Bend radius calculation 110
5.15 Design of a y-splitter 111
5.16 BPM-CAD simulation results of a y-splitter 111
5.17 Shift of two arms in a y-splitter 112
5.18 Microscope images of a y-splitter 113
5.19 Optical near-field mode of y-splitter1 with inter-scan shift 113
5.20 Optical near-field mode of y-splitter2 without inter-scan shift 114
5.21 Parallel writing of two multi-spot waveguides 115

6.1 Schematic diagram of the ultrafast laser fabrication system 119
6.2 Two types of waveguides in crystalline materials 121
6.3 Four-line waveguide structures 121
6.4 Type I single-line waveguide 123
6.5 Optical mode of type I single-line waveguide at different polarisation . 123
6.6 Edge view of the waveguides 124
6.7 Refractive-index modification of type I single-line waveguide 125
6.8 Type II double-line waveguides 126
6.9 Type II waveguides with different structures 127
6.10 Type II elongated double-line waveguide after annealing 128
6.11 Optical mode of type II double-line waveguide at different polarisations 129
6.12 Refractive-index modification of type II double-line waveguide after annealing 130
6.13 Non-reciprocal phenomenon 131
6.14 Type II waveguide in $LiNbO_3$ before and after aberration correction . 132

7.1 QRNG experimental setup and interferometer phase fluctuations with feedback 139
7.2 The PD amplitude variance as a function of LD power 142
7.3 The quantum signal to classical noise ratio γ as a function of LD power 144
7.4 Min-entropy and the optimal values of γ 145
7.5 The autocorrelation of raw data before and after the Toeplitz hashing 147

List of Tables

2.1 Measurement results for optical waveguide splitters 18

3.1 The first 22 Zernike polynomials 50

5.1 Fabricated waveguides with different pulse energies and writing speeds 100

5.2 Pulse energy requirement at different depths 102

7.1 The theoretical fitting values of the parameters at four sampling rates 143

7.2 The results of the standard NIST tests for final random bits 148

Chapter 1

Introduction

This chapter provides an overview of the research projects and accomplishments during my D. Phil. program, with a focus on understanding and demonstrating the ultrafast direct laser writing (DLW) technique. The motivation behind the research work is discussed, followed by a summary of the challenges. Finally, the organization of the dissertation is presented.

1.1 Motivation

Currently, most optical waveguides are fabricated using silica-on-silicon for integrated optics. The main challenge of this fabrication technique is its difficult formation process of high-quality silica layer. Ultrafast direct laser writing (DLW) [1–3], which can be used to generate three-dimensional (3D) waveguides and related optical elements in a single monolithic transparent substrate, has recently attracted enormous research interest. With its advantages of low cost, high flexibility and 3D capability, ultrafast DLW has emerged as one of the most powerful micro-fabrication techniques for 3D optical waveguides.

Typically, when an intense ultra-short pulse is focused into a transparent substrate, the extremely-high focused energy causes a refractive-index change in the

material. This pulse-induced modification caused by nonlinear absorption is highly confined in the focal region and deposits energy precisely within a sample regardless of its geometry. As a result, waveguides can be fabricated at arbitrary position which is impossible with traditional methods. Compared with other methods, the DLW technique eliminates the requirements for accurate alignment and other complicated manufacturing steps, facilitates the writing of complex structures and enables a truly 3D waveguide-fabrication process.

The DLW technique also avoids the use of expensive photolithography and cleanroom facilities. Despite the size reduction of optical devices and integrated circuits over the past decade, the equipment used in the traditional fabrication process is incredibly complex, large and expensive. The traditional equipment also requires high energy consumption for the material processes and inconvenient maintenance of a cleanroom. In contrast, the DLW approach is more efficient, using production facilities that are less complex and have much lower costs. In addition, unlike the fixed prototyping of other techniques, patterns used in DLW fabrication can be easily changed by modifying the shapes or traces of the foci. This results in reduced cost of the prototype masks and greater flexibility for the design of integrated optical circuits.

Similar ultrafast laser effects can be induced in different transparent materials, making the DLW technique flexible for fabrication in many substrates. The fabrication parameters, such as the wavelength, pulse width, pulse energy, repetition rate, focusing conditions and translation speed of the substrate, might vary among materials. But they can be easily controlled and adjusted by software instead of changing the hardware setup. Therefore, waveguide fabrication in compound substrates becomes feasible with the DLW technique.

Despite its obvious advantages, the ultrafast DLW technique did not receive much attention in the early years (before the 1990s). The development of the technique

was mainly limited by the ultrafast laser technology and a lack of understanding of the underlying mechanisms. With the fast development of femtosecond lasers in the 1990s, a laser-induced breakdown experiment in fused silica was first reported in 1994 [4], whereas the first DLW waveguide structures in glass were later demonstrated in 1996 [1]. In the past decades, with advances in laser technology and increasing interest in integrated circuits and microelectronics, significant progress has been made in the field of ultrafast laser processing. Numerous high-quality optical waveguides and components have been demonstrated using DLW [5–10], with comparable propagation losses and mode profiles to those obtained with standard methods. The industrial application of DLW becomes feasible. Advanced DLW facilities wider applications, such as optical communications and biophotonic applications [11], optical interconnects [12], optical storage and memory [13, 14], and quantum circuits [15–17], have been explored in the past years. Ultrafast DLW offers a potential option for more efficient manufacture of optoelectronics in the future.

Fabrication difficulties aside, another major challenge of DLW technique is the characterisation of written waveguides. This provides important information for system evaluation and is used to confirm whether the fabricated waveguides exhibit properties as designed. The main characteristics include refractive index, optical coupling, optical loss, polarisation, and nonlinear properties. Experimental evaluation and validation are necessary because these characteristics are rather difficult to determine theoretically. Characterisation results normally serve as feedback to the design and the fabrication process, which is crucial for the modification and optimization of the written waveguides. The characteristics of the waveguides can also be used to select appropriate fabrication parameters and to evaluate the performance of the designed DLW system.

1.2 Project Summary

The objective of the research is to fabricate and characterise optical waveguides with the DLW technique using adaptive optics, to improve the fabrication quality in different materials and to explore potential applications of the written waveguides. My research focuses on the design and improvement of the DLW fabrication system with aberration correction, modelling and fabrication of optical waveguides in transparent materials and using different analytical tools to well-characterise the written waveguides. The research aims to better understand the DLW fabrication system with proper control parameters and to continuously improve its performance. The major challenges of the project are as follows:

1. Understanding the DLW system with adaptive optics

   A novel DLW system with adaptive optics is proposed to further improve the quality of fabricated waveguides. Different qualities and characteristics of the written waveguide can be demonstrated through the effects of different fabrication parameters, and a full understanding of the DLW system is required. The objective of building a modelling-fabrication-characterisation cycle for the fabrication process is restricted to the performance of the existing DLW system and may also be affected by the accuracy of refractive-index prediction.

2. Characterisation of the waveguides

   It is essential to characterise the refractive-index information of the written waveguides, as they determine many important physical and transmission properties and give information about the fabrication process. Characteristics of most published waveguides are estimated on the basis of the simple numerical aperture (NA) method and cannot provide accurate refractive-index information. Other properties such as geometric dimensions, optical coupling modes and propagation loss are also very important and should be carefully investi-

gated.

3. Fabrication of optical waveguides in different materials

   The shape of a focal spot is impaired by aberrations that greatly affect the DLW quality. Aberration correction is needed to achieve improved-quality waveguides at various depths with different geometries. Waveguides fabricated in different materials require different parameters that should be carefully designed and controlled during the process. The resulting waveguides normally display different properties and characteristics, which are important to know for further fabrication.

4. Potential applications

   There are numerous applications of the DLW technique in information technology, including optical communications, optical interconnects and data storage. Meanwhile, DLW also has the potential to allow miniaturisation of quantum devices. For example, interferometers are widely used in quantum information tasks such as quantum key distribution and quantum random number generation. With the DLW technique, interferometers can be fabricated as integrated quantum devices on chips via waveguides. It is of great interest to investigate the possible implementations of the DLW approach in quantum information.

In summary, the DLW fabrication system with adaptive optics eliminates aberrations inside different materials, thereby greatly improving the quality of the generated waveguides. The DLW technique simplifies manufacturing complexity, showing a promising future for mass production and commercialisation in the long term.

1.3 Dissertation Organization

Chapter 2 reviews the background of the ultrafast DLW technique and evaluation methods of optical waveguides. It contains necessary information for a better un-

derstanding of the DLW technique and its underlying mechanisms. An overview of related and important DLW work is given, followed by detailed background information on the methods characterising the fabricated waveguides.

Chapter 3 describes the DLW system with adaptive optics. It provides background information for SLM-based aberration correction in the DLW system. Descriptions of the experimental setup and procedures are presented, together with a discussion of the related system parameters. The concepts of plasma sensing and Shack–Hartmann wavefront correction are then explained and their experimental results are discussed.

Chapter 4 presents the measurement procedures for the characterisation of the direct laser written waveguides. Accurate characterisation is essential for the fabrication of high-quality optical waveguides. To better understand the optical properties of the written waveguides, different measurement methods (including propagation-mode-near-field, equivalent-step-index and quantitative phase microscopy) for refractive-index estimation are studied and compared. In addition, the experimental setup and procedures for waveguides analysis are described. The simulation and experimental verification of the refractive-index information can be used to determine the transmission properties of optical waveguides and provide useful information for the fabrication process.

Chapter 5 presents the fabrication of different waveguides in fused silica. Aberration correction has been applied for waveguides deep into the surface. Bend waveguides and y-splitters are then modelled and fabricated in silica glasses, with a discussion of bend losses at different radii. Finally, multi-spot DLW results are presented and discussed.

Chapter 6 demonstrates waveguides fabricated in the potassium dihydrogen phosphate (KDP) crystal, which has different properties from those of fused silica. Two types of optical waveguides are introduced, with a discussion in their structures and characteristics. This is then followed by a description of the experimental setup and

processes that are applied to create two types of structures capable of guiding light. A brief demonstration of optical waveguides in $LiNbO_3$ reveals that the adaptive optics offers an improved quality in materials with high refractive indices.

Chapter 7 describes a quantum random number generation (QRNG) system with a speed that is one order of magnitude higher than the current state-of-the-art. The implementation of a stable interferometer is crucial in the design, which pushes the random bit rate up to 68 Gbps. Proper data post-processing algorithms are presented and discussed. Although there is no direct link between the proposed QRNG system and the DLW technique, QRNG can eventually be integrated onto a chip using DLW to realize a more compact and stable interferometer.

Chapter 8 summarises the dissertation and presents its conclusions. Suggestions and ideas are proposed and discussed for future research in the field of ultrafast laser writing in various transparent dielectric materials.

Chapter 2

Background on Waveguide Fabrication and Characterisation

This chapter begins with a description of modification mechanisms of the ultrafast direct laser writing (DLW). The underlying physics is explained, including how refractive-index change is induced by the laser pulses. Different laser fabrication methods and fabrication parameters are reviewed and compared, followed by an overview of optical waveguides and devices using DLW in different materials. Finally, a review of characterisation techniques and measurement procedures for optical waveguides is described, with a focus on the methods for measuring the refractive-index profile.

2.1 Refractive-Index Modification

Laser-induced refractive-index changes in transparent materials were first discovered in the early-to-mid 1970s [18, 19]. The experimental demonstration by Hill's group showed that the photosensitivity obtained in the Ge-doped optical fibers could be manifested by a blue laser and could be employed to fabricate a distributed Bragg reflector as a laser mirror. Later, more studies revealed that the refractive-index change induced by laser was mainly caused by a nonlinear absorption process. Un-

fortunately, strong laser absorption was needed for the effect to take place, which limited the fabrication process to certain materials. In addition, the refractive-index change was too small to be used for practical applications at that time.

Much higher refractive-index changes were able to be induced by the DLW technique in the 1990s with the fast development of ultrafast lasers. Compared with the earlier laser processing technique, an ultrafast laser - normally in the range of femtosecond with nonlinear laser processing effect - has advantages in creating less collateral damage, fabricating devices inside bulk specimens and being able to work in more materials. Ultrafast laser micromachining was first reported in 1994 [4], when a femtosecond laser was used to demonstrate laser-induced breakdown experiments in fused silica. Despite the success in fabricating various devices using a femtosecond laser, the underlying mechanisms are very complex and remain uncertain. Normally, the mechanisms of the refractive-index change induced by a femtosecond laser can be divided into two steps: energy absorption and energy dissipation.

The energy absorption process can be described as follows. At the beginning, electrons in dielectrics are normally strongly-bounded to their parent atoms. However, when an intense ultrashort (normally tens or hundreds of femtoseconds) laser pulse is focused onto the surface of a transparent dielectric material, a number of electrons will be freed from the valence band through the nonlinear ionization. These pulses have very high peak power with relatively low total energies, allowing efficient, highly-nonlinear processing. There are two classes of excitation mechanisms: photoionization and avalanche ionization. Photoionization is a mixture of multiphoton and tunneling ionization. Multiphoton ionization normally occurs at higher laser frequencies with simultaneous absorption of m photons. Tunneling ionization appears at strong laser field when valence electrons tunnel to the conduction band because of the suppressed Coulomb potential energy barrier. Depending on the laser frequency and intensity, multiphoton ionization usually dominates over tunneling ionization in femtosecond

laser interaction with dielectrics.

Once the initial free electrons are generated, more electrons are freed followed by the avalanche process. A free electron continues to gain more energy to higher energy states in the conduction band by absorbing photons through inverse Bremsstrahlung. When its total energy exceeds the minimum conduction band by more than the band gap energy, the initial free electron can ionize another electron from its valence band. This results in two free electrons that can continue absorbing more energy and generate more free electrons.

The electronic plasma formed by multiphoton and avalanche ionization can absorb the laser energy efficiently if its density exceeding some critical value. A large portion of the laser energy will be absorbed in the focal volume, which leads to ultrafast ablation in the material with minimal thermal affection to the surrounding area.

The energy absorption process is well-understood [20–22] while the energy dissipation process is not. There are a few possible explanations, but none of them is fully accepted. The dissipation process is very complex and highly depends on the material and laser parameters. Thermal diffusion is widely believed to be one of the main cooling mechanisms in the case of high repetition rate laser-writing.

The energy deposited by the laser first melts the material in the focal area. Subsequently, rapid re-solidification dynamics cools the material in the high temperature state. This leads to density and refractive-index changes in the material [22].

For low repetition-rate laser-writing, it is possible that there is too much time between laser pulses for the temperature of the surrounding material to increase. A coulomb explosion may be introduced by the laser pulses [23], which may generate a shockwave [24] within the material. The shockwave would then take energy away from the focal region, compress the surrounding material and result in refractive-index changes. Unfortunately, these explanations are far from certain, and the underlying principles of the energy dissipation process have not been confirmed.

2.2 Fabrication Methods and Parameters

The refractive-index modifications induced by ultrafast lasers depend both on the irradiation parameters (focusing conditions, wavelength, pulse energy, repetition rate, pulse duration, etc.) and on the material properties (band gap, dispersion, ionization rates, thermal conductivity, etc.). The main parameters during the fabrication process are the laser wavelength, pulse repetition rate, width and energy, writing speed and focusing conditions.

There are normally two types of refractive-index changes induced by femtosecond lasers. A type I waveguide produces weak damage at the focal area, leading to a smooth refractive-index modification while maintaining uniformity and good optical quality (Figure 2.1). As the refractive-index change is created in the focal volume, the optical mode is guiding through the fabricated track (Figure 2.1(c)). Type I waveguides can be obtained simply by scanning the sample with ultrafast laser pulses and have been demonstrated in a number of different materials. However, type I waveguides in some crystals ($LiNbO_3$ or ZnSe for example) can deteriorate or even be removed completely after heating. This might be because the refractive-index change typically requires an increase in the material density, which is difficult to achieve in some materials with crystalline structure due to the large positional order of the lattice.

A type II waveguide comprises the generation of a severe damage track along the propagation direction with a longer focal volume (Figure 2.1). Unlike those of type I, refractive-index changes of type II waveguides are obtained adjacent to the modification area. A double-line structure is widely used for type II waveguides, confining the guiding light between the two fabricated lines (Figure 2.1(f)). Type II waveguides have been reported in a number of crystals (Nd:YAG, $LiNbO_3$ and Nd:GGG, etc.) and are shown to be stable at high temperatures.

Pulse repetition rate is an important parameter for the DLW fabrication. Nor-

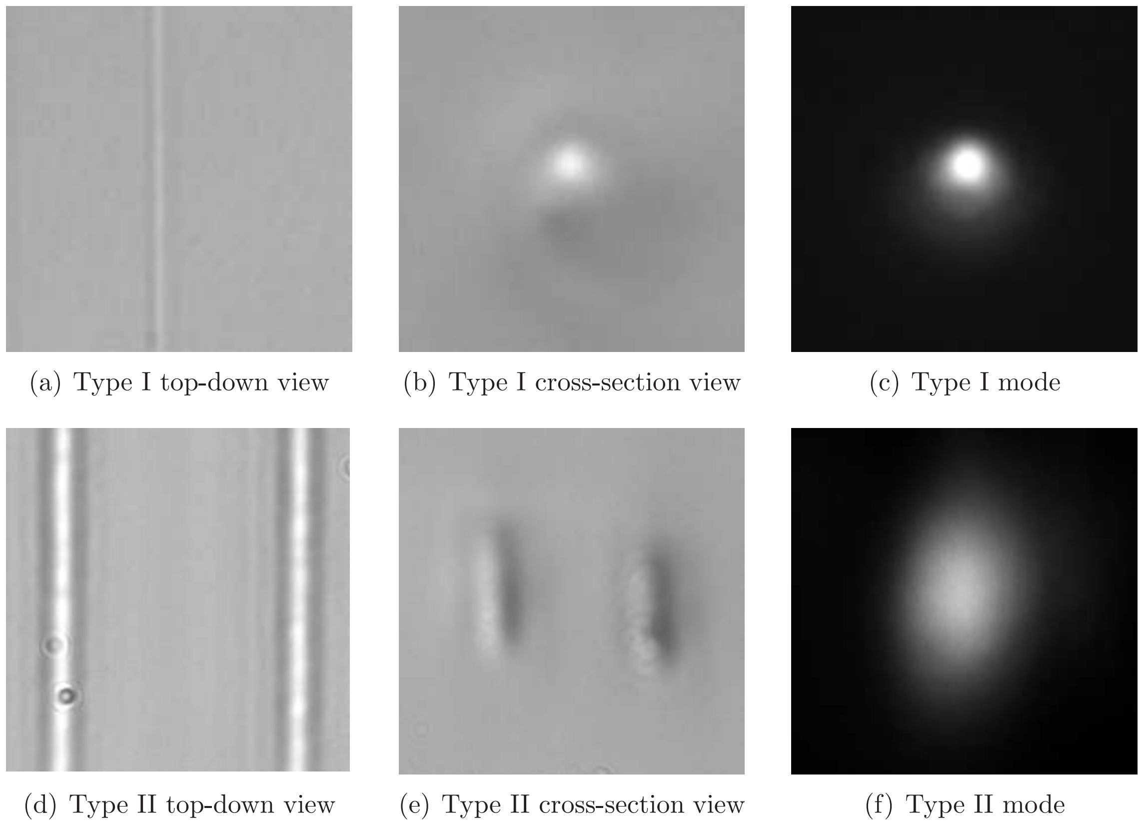
(a) Type I top-down view (b) Type I cross-section view (c) Type I mode
(d) Type II top-down view (e) Type II cross-section view (f) Type II mode

Figure 2.1: Microscope and mode images of type I and type II waveguides under transmission microscope (with slight defocus). (a)(d) fabricated waveguide top-down view; (b)(e) fabricated waveguide cross-section view; (c)(f)the coupling optical mode at the end of the waveguide.

mally, high-repetition rate is defined as laser writing in which "substantial thermal accumulation occurs between subsequent laser pulses, affecting the modification process." However, it is difficult to clarify "substantial thermal accumulation". Also, the definition of repetition rate is material-dependent and changes with other writing parameters. Generally speaking, megahertz systems are considered as high-repetition rate whereas kilohertz system is low-repetition rate. Although the underlying reason is still unclear, different repetition rates result in different effects in different materials. For example, megahertz systems have better performances in some materials, whereas kilohertz systems are preferred in others. Thus, the laser type should be carefully chosen depending on the material and experimental observations.

For pulses longer than tens of picoseconds, more time is allowed for exponential growth of the electron density for avalanche ionization. In this case, photoionization induced by high laser intensity is not required to obtain the initial seed electrons. Conversely, for short pulses, nonlinear absorption occurs on a short time scale before the energy transfer, and the initial electrons mainly come from photoionization. Demonstrations have shown that short-pulse (femtosecond) lasers can generate more confined waveguides and deposit less energy than long-pulse ones. Thus, femtosecond lasers are normally used nowadays for DLW.

The pulse energy should also be carefully adjusted during DLW fabrication. The refractive-index modification has a highly nonlinear relationship with the intensity, I, which is related to the pulse energy, E, as follows:

$$E = I\tau A \tag{2.1}$$

where τ is the temporal pulse width, A is the exposed area. Sometimes, the pulse fluence (J/cm^2), F, is used to describe the fabrication pulse energy instead of E:

$$F = \frac{E}{A} = I\tau \tag{2.2}$$

Sufficient pulse energy (fluence) should be applied in order to modify the material. However, severe damage may occur if the pulse energy (fluence) is too high, resulting in limited light-guiding. The required pulse energy varies from material to material, and a typical energy for a 100 fs laser is approximately a few μJ.

There are two writing geometries for the DLW system: longitudinal and transverse, depending on whether the sample is moved parallel or perpendicularly to the beam-propagation direction. DLW was first developed using the longitudinal writing direction, i.e. along the z-axis, as shown in Figure 2.2. The cross-section of the fabricated waveguide is circular (on the x and y-axes) because a focused Gaussian beam is initially symmetric (Figure 2.3(a)). However, the writing length of the waveguide along the z-axis is limited by the working distance of the microscope objective. Transverse writing, on the other hand, allows arbitrary waveguide writing length in the plane (along the x or y-axis) perpendicular to the laser beam, giving more flexibility to the DLW fabrication of three-dimensional (3D) waveguides. However, transverse writing usually has an elliptical profile, resulting from the difference between the Gaussian beam waist (the x or y-axis) and the confocal parameter (the z-axis). This elongation leads to an asymmetric cross-section (Figure 2.3(b)) that can be reduced using high numerical aperture (NA) objectives. Unfortunately, the working distance of the microscope objectives decreases as the NA increases. Moreover, high NA results in tightly focused-beam, leading to smaller waveguide sizes. Therefore, there is normally a trade-off between the symmetry of the cross-section and the NA.

Other parameters such as writing speed, writing patterns and focusing conditions are all essential for the DLW system, and should be carefully chosen during the fabrication process. The most popular and widely used lasers for DLW are regeneratively amplified 100-200 fs Ti:sapphire lasers with 1-200 kHz repetition rate. These low-frequency systems can fabricate waveguides in many different materials, but have

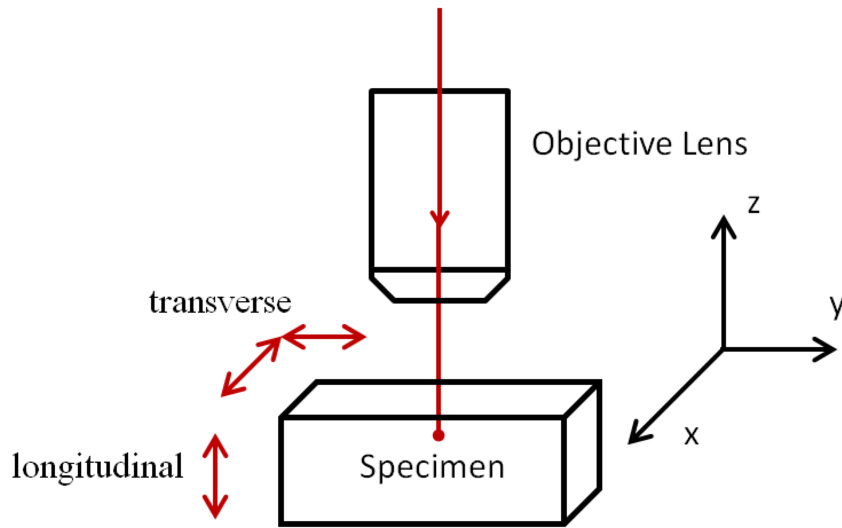

Figure 2.2: Direct laser writing geometries: longitudinal writing along z-axis and transverse writing along x or y-axis.

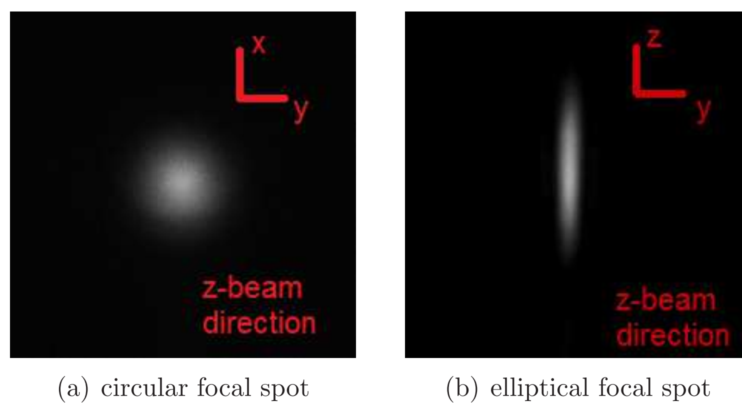

(a) circular focal spot (b) elliptical focal spot

Figure 2.3: Circular and elliptical Gaussian focal spot of longitudinal and transverse writing.

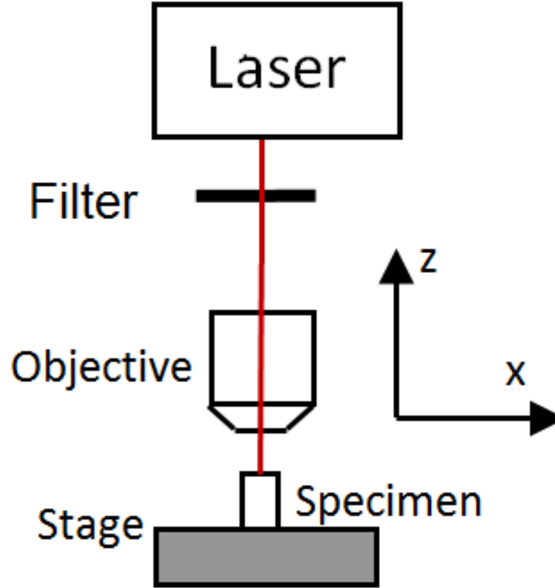

Figure 2.4: Schematic diagram of a typical DLW system.

limited writing speed (10-100 μm/s) and small refractive-index changes (1-2$\times 10^3$).

2.3 Optical Devices Fabricated by Ultrafast Lasers

A diagram of a typical DLW setup is shown in Figure 2.4. A refractive-index change in the focal region occurs when an intense ultra-short pulse is focused into a transparent material. By moving the focal point inside the substrate, refractive index can be modified in 3D accordingly, and can be used for the fabrication of optical lenses, gratings and other components.

Many different DLW systems and fabrication procedures [5–7, 9, 10, 25] have been reported in the past decade. The first 1×2 y-splitter was presented in [26], in which refractive-index changes of 3×10^{-3} in pure fused silica and 5×10^{-3} in boron-doped fused silica were obtained. The demonstrated splitter with an angle of 0.5° could split approximately equal amounts of input signal at 514.5 nm into two arms (shown in Figure 2.5). However, no details such as the transmission loss, exact splitting ratio, or transmission modes of the written y-splitter were provided in the paper.

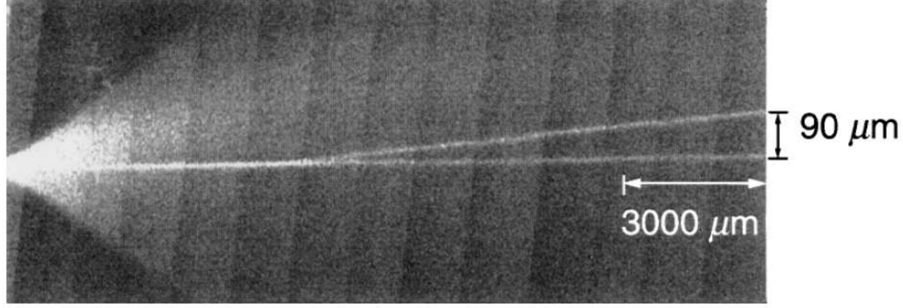

Figure 2.5: First demonstration of a 1×2 y-splitter fabricated using DLW in pure fused silica guiding 514.5 nm light. Reprint with permission from [26].

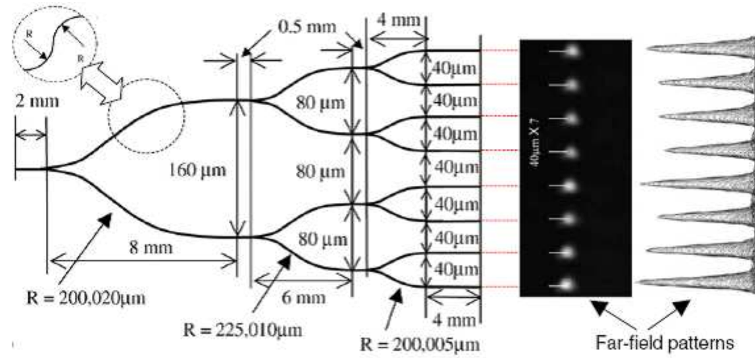

Figure 2.6: Schematic diagrams of a DLW 1×8 optical splitter and its far-field patterns. Reprint with permission from [6].

Liu et al. reported high-quality power splitters in fused silica by implementing a multi-scan technique [6]. Figure 2.6 shows the schematic design of a 1×8 splitter, consisting of three cascading 1×2 splitters. All the radii of curvature (R) were carefully designed to avoid significant bend loss. Double-scan writing with an inter-scan shift of 1.5 μm was applied in the fabrication of the splitters. The written y-splitter was operating in a single mode at 1,550 nm and the additional splitting loss per junction was estimated to be 0.5 dB. An average insertion loss (IL) of 16.39 dB was measured for a 1×8 splitter and 6.72 dB for a 1×2 splitter, as displayed in Table 2.1. The far-field patterns of the written splitter were neither very circular nor uniform, which could be a serious concern for the design of a high-quality splitter.

A 3D DLW 1×4 splitter was first demonstrated in a glass by Sakakura et al. [10], in which $L_{AB} = 5$ mm, $L_{BC} = 10$ mm and $L_{CD} = 5$ mm (Figure 2.7). Multiple focal spots

Type	Average IL (dB)	IL uniformity (maximum) (dB)
1×8 splitter	16.39	1.09
1×4 splitter	10.10	1.56
1×2 splitter	6.72	0.12
Straight waveguide	3.45	

Table 2.1: Measurement results for 1×2, 1×4 and 1×8 optical waveguide power splitters with the double-scan writing. Reprint with permission from [6].

were generated by phase modulation using a spatial light modulator (SLM), as shown in Figure 2.7(c). The transversal separation of the splitter was approximately 86 μm, while the vertical separation was approximately 91 μm, as shown in Figure 2.7(d). Note that the waveguide structure was highly elongated, which greatly reduced the quality of the guiding mode (Figure 2.7(e)). Losses of this 1×4 splitter were not evaluated in the paper and further investigation was needed to optimise the structure of the splitter.

The DLW technology has also been successfully applied to the fabrication of waveguide Bragg grating (WBG). A weak WBG was fabricated in [27] with −3.5 dB transmission, where a phase mask was used to generate the interference fringe pattern. The channel waveguide was exposed under the fringe pattern to fabricate the grating. Reference [7] demonstrated the feasibility of −12 dB transmission Bragg gratings with a reflection bandwidth of 0.76 nm.

Waveguides fabricated using DLW have also been demonstrated in many different materials, such as lithium niobate ($LiNbO_3$), potassium titanyl phosphate (KTP), bismuth germanate (BGO), etc. $LiNbO_3$ is a well-known nonlinear crystal with many photonic applications and one of the first-investigated crystals for the DLW technique. The origins of DLW modification in $LiNbO_3$ were studied and discussed in [28], where two different types of waveguides (type I and type II) were demonstrated. Figure 2.8 shows the refractive-index modification profiles and guided optical modes of type I

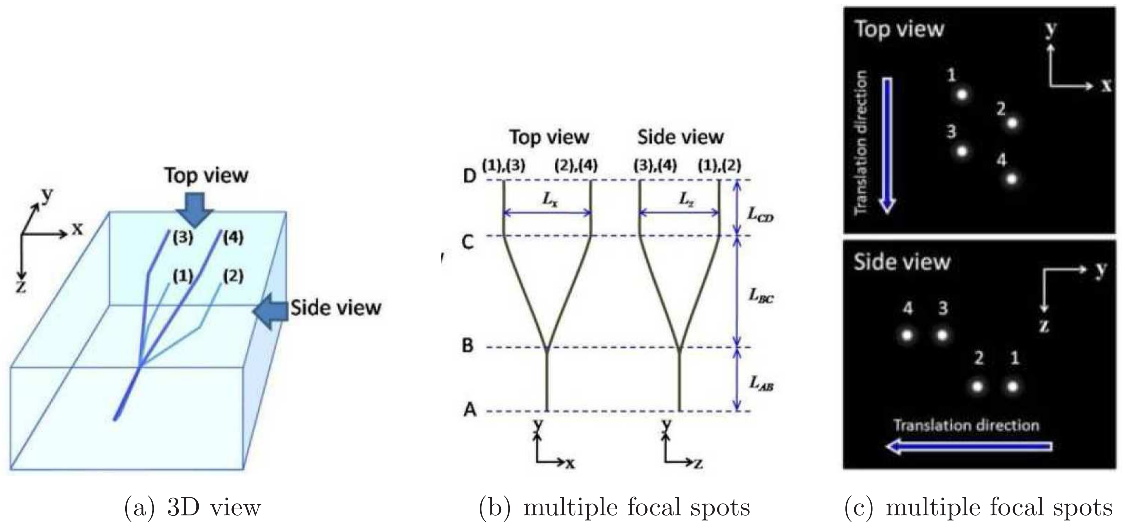

(a) 3D view (b) multiple focal spots (c) multiple focal spots

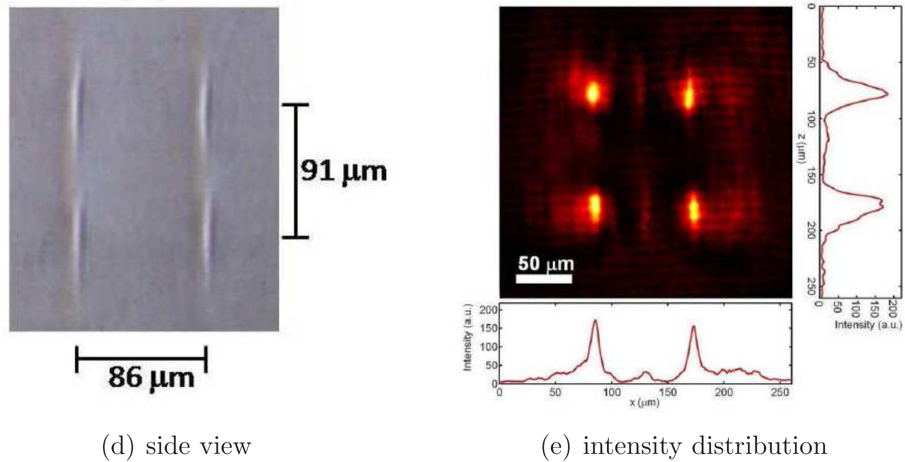

(d) side view (e) intensity distribution

Figure 2.7: A 3D 1×4 splitter fabricated using DLW. (a) 3D view of the fabricated 1×4 splitter; (b) multiple focal spots for writing the splitter; (c) cross-section image of the splitter; (d) the intensity distribution of the guided mode. Reprint with permission from [10].

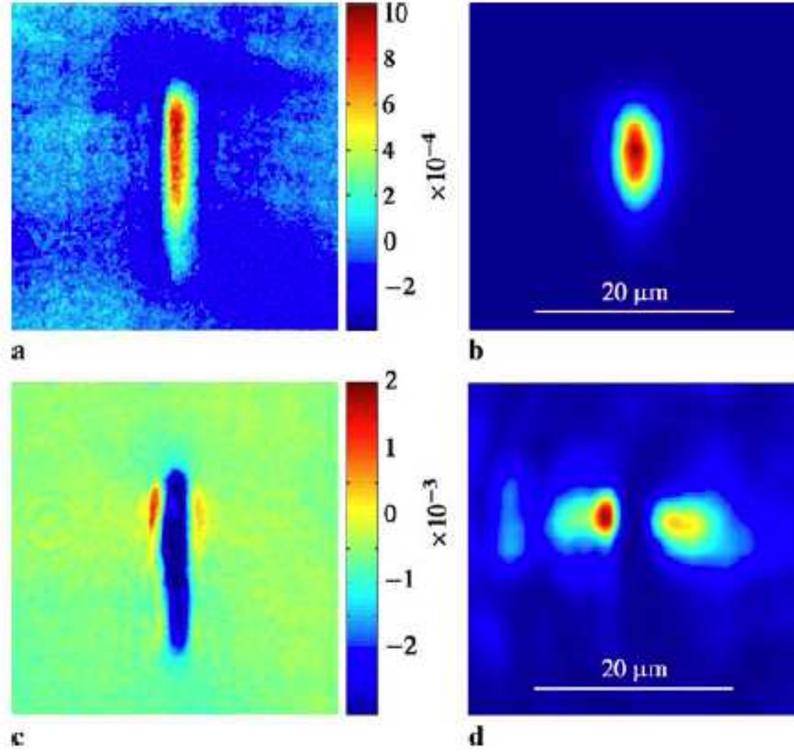

Figure 2.8: Type I and type II waveguides fabricated in $LiNbO_3$ using DLW at a fixed pulse energy of 0.2 μJ. (a) type I extraordinary refractive-index profile; (b) guided mode at 633 nm for a pulse duration of 220 fs (type I); (c) type II extraordinary refractive-index profile; (d) guided mode at 633 nm for a pulse duration of 1.1 ps (type II). Reprint with permission from [28].

and type II waveguides in $LiNbO_3$.

A type I y-splitter was fabricated in $LiNbO_3$ in [29], with a loss of $\sim$ 1 dB/cm at 632.8 nm and a splitting ratio of 1.1:1. However, as the refractive index of the $LiNbO_3$ crystal (n $\approx$ 2.2 at 790 nm) is significantly higher than that of fused silica, the spherical aberration is more severe, causing significant defocus and focal distortion. As shown in Figure 2.9, the cross-section of the written splitter was highly elongated, resulting in poorly-guided modes.

As type I waveguides in $LiNbO_3$ are not stable after low-temperature annealing or even at room temperature, type II waveguides have also been investigated in $LiNbO_3$ and other crystals [28–31]. Type II waveguides normally have larger refractive-index variation than type I waveguides, and the guiding region is located

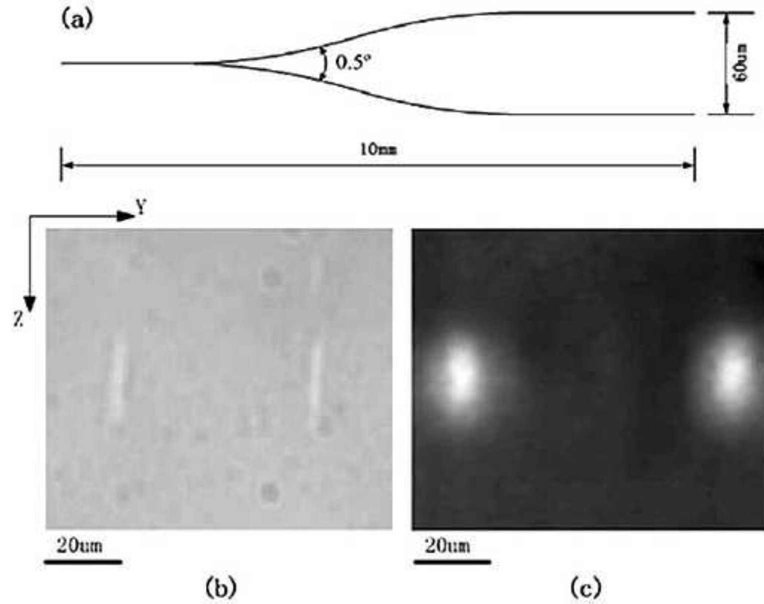

Figure 2.9: A type I y-splitter fabricated in $LiNbO_3$ using DLW. (a) schematic layout of the y-splitter; (b) cross-section image of the y-splitter; (c) guided modes of the y-splitter. Reprint with permission from [29].

within the refractive-index change between two parallel traces.

In addition, extensive research has triggered the development of the DLW technique in different applications, such as optical interconnects [12], quantum circuits [15–17], optical communications [11], etc.

2.4 Characterisation of Optical Waveguides

Optical waveguides are normally defined as structures that guide optical signals in a confined region, which usually has higher refractive index than its surrounding area. Different characterisation methodologies have been implemented to better understand the properties of the fabricated waveguides, such as geometric dimensions, optical coupling modes, refractive-index profiles and propagation losses. Theoretical simulation and experimental measurements can provide important data to evaluate a DLW system and fabricated waveguides. The evaluation results can then be used as the basis

for further simulation and modelling of devices, and can also be applied as feedback signals to the fabrication process. Characterisation results can help to improve the performance of the DLW system and optimise the quality of the waveguides.

2.4.1 Geometric Measurement

The dimensions and structure of a fabricated waveguide are important characteristics to determine the light propagation inside a guiding region. Both the material conditions (flatness, cleanness, surface defects, side wall roughness, etc.) and waveguide dimensions (thickness, depth, cross-section, length, etc.) greatly affect the performance of the waveguide. For example, the surface flatness (cleanness) contributes to the scattering loss, whereas the thickness of the waveguide (together with the refractive-index difference) limits the cutoff wavelength. The dimensions of a waveguide also determines the properties of its guiding modes.

Waveguides fabricated by DLW usually have dimensions of a few μm, which should be inspected by equipment with a high resolution and magnification. Because the stylus of a surface profiler may scratch the waveguide during its scanning, without high-accuracy requirement, an optical microscope is normally used for waveguide observation and measurement.

A sample written with optical waveguides is first inspected under a high-quality microscope for its physical appearance, such as the surface cleanness, flatness, scratches and jaggedness at the edges (Figure 2.10). In most cases, these defects can be removed by cleaning or polishing the surface. However, some of the surface defects may result in more scattered light and cause additional losses. Once the surface and edges are inspected and cleaned, the thickness, depth, length and cross-section of the fabricated waveguide should be carefully measured under the microscope. These measurement and inspection results provide useful information for the understanding of the waveguides.

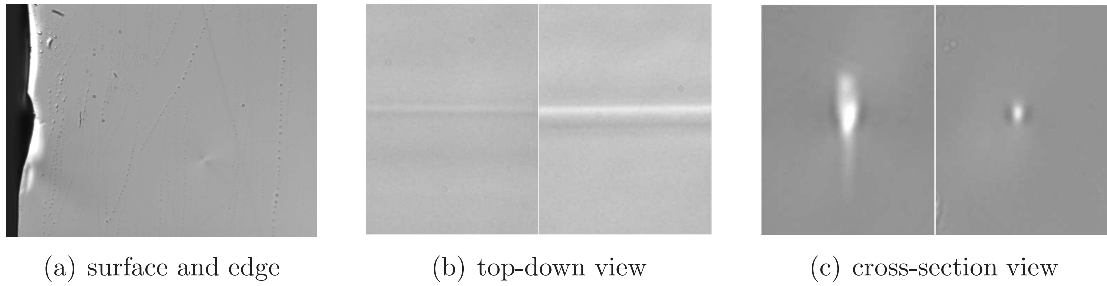

(a) surface and edge (b) top-down view (c) cross-section view

Figure 2.10: Microscope images of fabricated waveguides. Observation of the surface and edge quality, top-down and cross-sectional views.

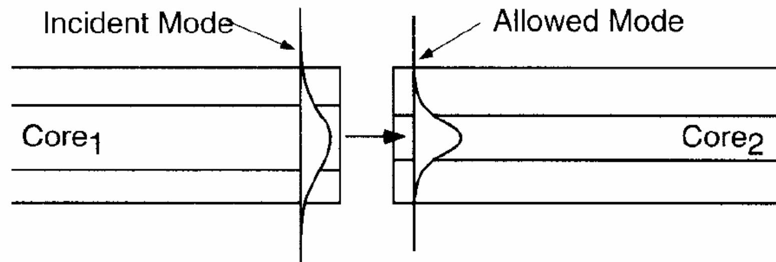

Figure 2.11: Mode coupling between two waveguides. Reprint with permission from [32].

2.4.2 Coupling into Waveguides

Coupling light into an optical waveguide is widely used to evaluate the characteristics and performance of a waveguide. The fundamental mode of a weakly-guiding waveguide is approximately Gaussian in shape. Normally, it is called end-fire coupling when the Gaussian beam is coupled from a laser into a waveguide, and butt coupling from one waveguide mode into another. In most cases, the input mode has different dimensions from the output one, as shown in Figure 2.11. The coupling efficiency is determined by the overlapping of the two modes.

When the output mode of the laser is not Gaussian-shaped, the light can be coupled into fiber first, reshaping the beam into Gaussian mode. The reshaped output is then coupled into a waveguide sample, either by using an objective lens focused onto the waveguide end or by direct butt-coupling (Figure 2.12). Note that the end surface of the waveguide should be carefully polished to ensure minimum loss.

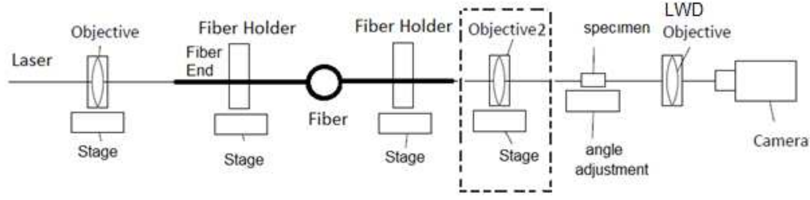

Figure 2.12: End-fire coupling and butt coupling between laser, fiber and a waveguide sample. The fiber end can coupled into the waveguide with or without Objective2 in the dotted box. The output mode is then captured by the CCD camera.

The output mode of the waveguide is finally captured by using a long-working distance (LWD) microscope objective lens attached to a charge-coupled device (CCD) camera, as shown in Figure 2.12. The measured near-field mode from the CCD camera can be used for the refractive-index evaluation. Coupling between different modes is very sensitive to angles and position alignments. Therefore, in the experimental setup, all the objectives, the fiber and the waveguide sample should be mounted on top of high-precision stages in order to achieve stable and accurate alignment.

2.4.3 Refractive-Index Measurement

The refractive-index distribution of an optical waveguide plays an important role in determining its physical and transmission properties. Many different methods and techniques have been proposed for determining index profiles on the basis of different principles [33–37]. The reflection method, which was first proposed in [38], is simple and straightforward. The reflectivity, R, is defined as the ratio of reflected light power, P_r, to incident light power, P_i:

$$R = \frac{P_r}{P_i} = (\frac{n_r - 1}{n_r + 1})^2 \tag{2.3}$$

where n_r is the refractive-index distribution to be measured.

The reflected power P_r from the surface of the sample is directly related to the refractive index n_r. If the reflectivity of the cladding, R_c, is known, it can be used as

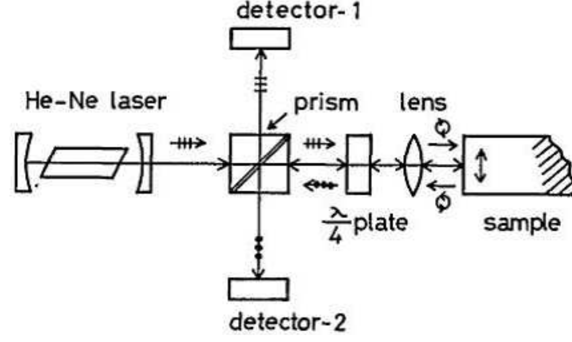

Figure 2.13: Experimental setup for the reflection method. Reprint with permission from [38].

a reference:

$$R_c = \frac{P_c}{P_i} = (\frac{n_0 - 1}{n_0 + 1})^2 \tag{2.4}$$

where P_c and n_0 are the reflected light power and refractive index of the cladding.

From Equation (2.3) and (2.4), the refractive-index difference Δn_r can be calculated as:

$$\Delta n_r = n_r - n_0 = \frac{(n_0^2 - 1)(\sqrt{\frac{P_r}{P_c}} - 1)}{(n_0 + 1) - (n_0 - 1)\sqrt{\frac{P_r}{P_c}}} \tag{2.5}$$

Figure 2.13 shows the experimental setup for the reflection method. If the light powers from different spots on the sample end are scanned and measured, the refractive-index profile can be obtained. The prism and $\lambda/4$ waveplate are used to eliminate the reflected light from surfaces other than the sample's, which helps to collect the reflected light from the sample's surface more effectively.

The theory behind the reflection method is simple but not applicable in practice. According to the method, first, the end face of the sample needs to be well-cut and shaped. The method is also very sensitive to any dust or dirt on the surface. Because of the small refractive-index change between the core and the cladding, the amount of power change is also small. The reflection method requires very high accuracy in the measurement of the reflected light.

The interferometric slab method is also widely used because of its high accu-

racy [33, 36]. When the light passes through a sample, the phase retardation ϕ_r can be written as follows:

$$\phi_r = k_0 L = k_0 n_r d \tag{2.6}$$

where k_0 is the free space wavenumber, L is the optical path length and d is the slab thickness. For the measurement shown in Figure 2.14(a), two arms form an interferometer: one of the arms passes through a slab sample, and the other arm passes through a reference slab with a refractive index n_0 equivalent to that of the cladding. Because the two paths go through different optical lengths (with different refractive indices), an interference fringe is created, as shown in Figure 2.14(b). The fringe spacing, D, corresponds to a relative phase shift, 2π. Therefore, for a fringe shift S_r,

$$\frac{2\pi}{D} = \frac{k_0(n_r - n_0)d}{S_r} \tag{2.7}$$

The resulting refractive-index difference Δn_r can be calculated as follows:

$$\Delta n_r = n_r - n_0 = \frac{k_0 S_r}{2\pi D d} = \frac{\lambda_0 S_r}{D d} \tag{2.8}$$

where λ_0 is the laser vacuum wavelength.

The thickness of the entire slab needs to be within a fraction of the wavelength, because of its sensitivity to phase change. Unfortunately, this is difficult to achieve in practice and is the major drawback of the interferometric slab method.

A more practical technique for refractive-index measurement is the propagation-mode near-field method (PMNFM) [37,39,40], which was first proposed in [37]. This method is effective for small and weakly-guiding waveguides, especially for single-mode waveguides. The method can also be applied to multimode waveguides if only the fundamental mode is excited. By applying the PMNFM, the refractive-index profile can be obtained from the measurement of the near-field pattern of a propagating mode, which has a field distribution of ψ, from the output end face of the waveguide.

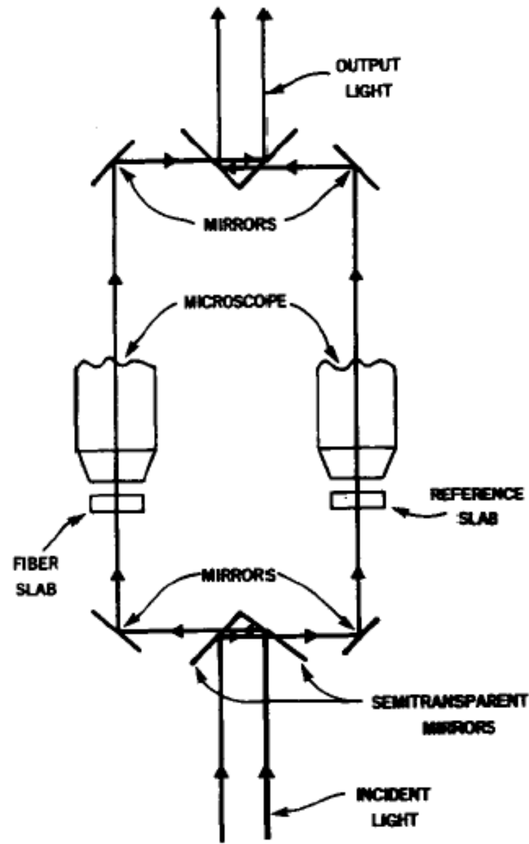

(a) experimental setup

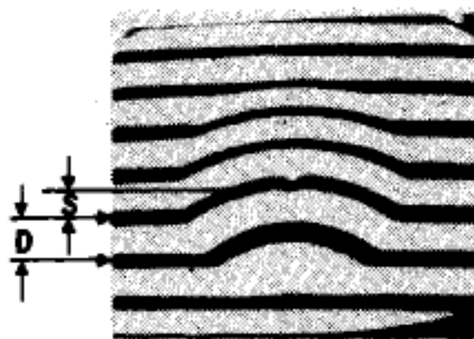

(b) interference fringe

Figure 2.14: Schematic diagrams of the interferometric slab method. Reprint with permission from [36].

For a weakly-guiding waveguide, if the refractive index depends only on the distance from the center axis, if the permeability of the medium is homogenous and equal to that of vacuum, and if only the fundamental mode is excited, n_r is a function of ψ_r and r [37, 39]:

$$n_r = -\frac{1}{2n_0 k_0^2 \psi_r}\left(\frac{1}{r}\frac{d\psi_r}{dr} + \frac{d^2\psi_r}{dr^2}\right) + C \tag{2.9}$$

where n_r is the refractive-index distribution, n_0 is the substrate refractive index, k_0 is the wavenumber in vacuum, ψ_r is the near-field mode distribution, r is the distance from center axis, and C is a constant that can be measured by experiment. The details of the PMNFM theory are discussed in Chapter 4. The measured intensity distribution is smoothed by a local least-squares method using a curve of third-order in [37]. The refractive-index profile is calculated from the smoothed intensity distribution and shown in Figure 2.15(a). The dot-dash curve in Figure 2.15(b) displays the difference between the measured intensity distribution and the calculated intensity distribution for the refractive-index profile in Figure 2.15(a). The results indicate that there is only approximately a 0.5% difference between the measured intensity and the calculated one.

After comparing different techniques used for refractive-index profile evaluation, it is concluded that the PMNFM is the simplest and most practical method. However, because of its high-sensitivity to noise, further data post-processing algorithms are still required for better smoothing.

2.4.4 Propagation Loss

The propagation loss of an optical waveguide is one of its most important characteristics. Obviously, a highly-lossy waveguide cannot be used in practical applications. In general, three major mechanisms contribute to the propagation loss of a waveguide: light radiation (mode conversion), material absorption and scattering loss [41].

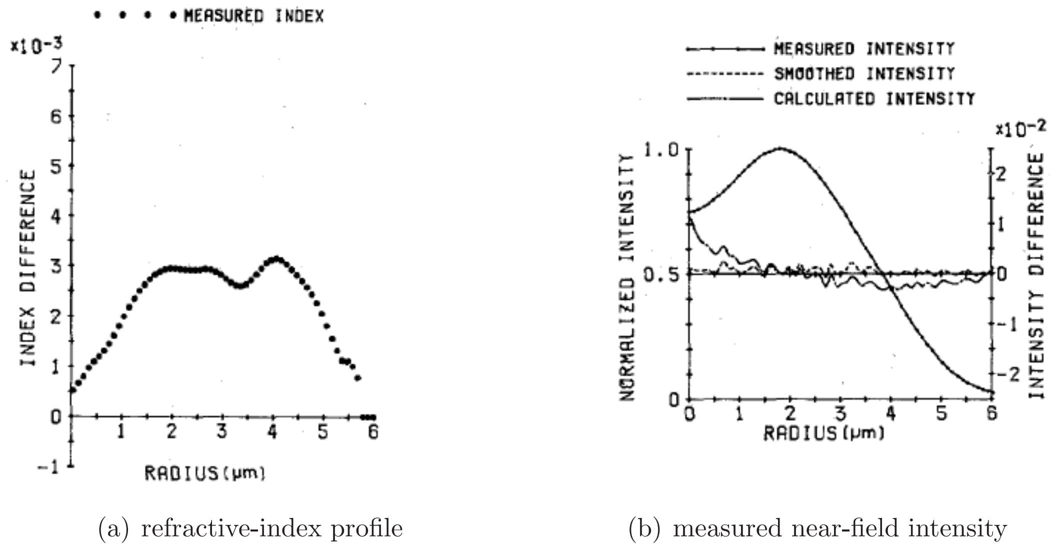

(a) refractive-index profile

(b) measured near-field intensity

Figure 2.15: Measurement results of a single-mode fiber using the propagation-mode near-field method (PMNFM). Reprint with permission from [37].

The electromagnetic field can be confined in the center core when the propagation constant of the guided mode β is much larger than that of the substrate (β_0). If $\beta \approx \beta_0$, the light radiation occurs and the energy is dispersed from the core into the surrounding substrate. Normally, light radiation loss takes place when the refractive-index difference or the waveguide thickness is too small to meet the condition of $\beta \gg \beta_0$. Energy loss also occurs when there is mode transformation during the propagation, such as bend waveguides or the inhomogeneity of the refractive index.

In addition, the imparities, defects, or doped ions inside materials of waveguides may absorb the light during propagation. The absorption loss sometimes is limited to certain wavelength ranges by different types of materials. The scattering loss mainly comes from the imperfections between the interfaces or inside the waveguides. As shown in Figure 2.16, defects of the material, such as surface roughness, cracks, dust, imperfections between substrate and waveguide interface, all contribute to the propagation loss.

The power remaining when propagating through an optical waveguide along the

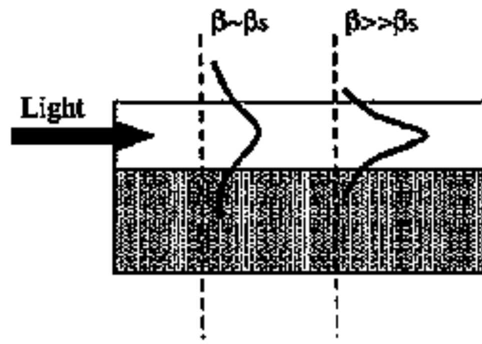

(a)

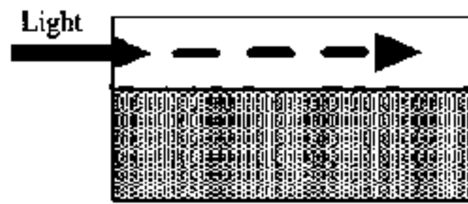

(b)

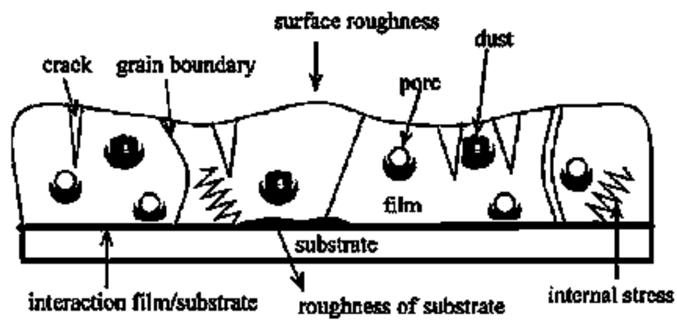

(c)

Figure 2.16: Major sources of propagation loss. (a) propagation loss by light radiation; (b) propagation loss by absorption; (c) propagation loss by scattering. Reprint with permission from [41].

beam propagation direction (the z-axis) can be defined as follows:

$$I(z) = I_0 \times 10^{\frac{-\alpha z}{10}} \tag{2.10}$$

Here, I_0 is the initial input power, I(z) is the power transmitted through the waveguide along the z-axis (cm), and α is the attenuation coefficient of the waveguide, presented in decibels per centimeter (dB/cm). The loss, L, is defined as follows (in dB):

$$L(dB) = -10\log(\frac{I(z)}{I_0}) \tag{2.11}$$

The cutback method is the most commonly used technique for attenuation measurement in optical waveguides. This method couples the light into a waveguide, and measures the output intensity of the light emitted from its end-face. The waveguide is then cleaved or end-polished to obtain a shorter waveguide and the same measurement is repeated. Based on the length difference between several measurements, the propagation loss can be estimated. The cutback method is quite accurate and stable, however, is a destructive method.

Scattered-light measurement is a non-destructive method for measuring the propagation loss. A high-powered laser beam is coupled into a waveguide, and a high-precision camera is used to take the top-down view of the sample (Figure 2.17(a)). The scattered light intensity can be recorded and plotted as a function of distance along the beam-propagation direction (an example shown in Figure 2.17(b)). An experimental image is shown in Figure 2.17(c). However, this method is extremely sensitive to errors that may cause the change of scattered light, such as the imperfections inside the waveguide, surface roughness or dust. Therefore, multiple measurements should be applied to minimise the errors. Note that the camera should have high quality in order to capture the intensity difference and eliminate the background noise.

A straightforward method for propagation-loss estimation is direct measurement

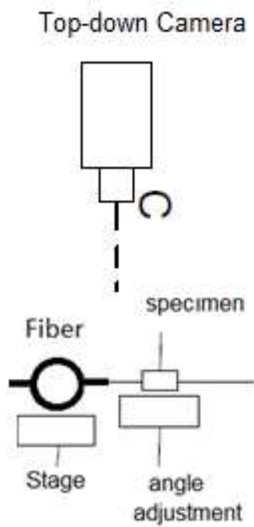

(a) schematic diagram

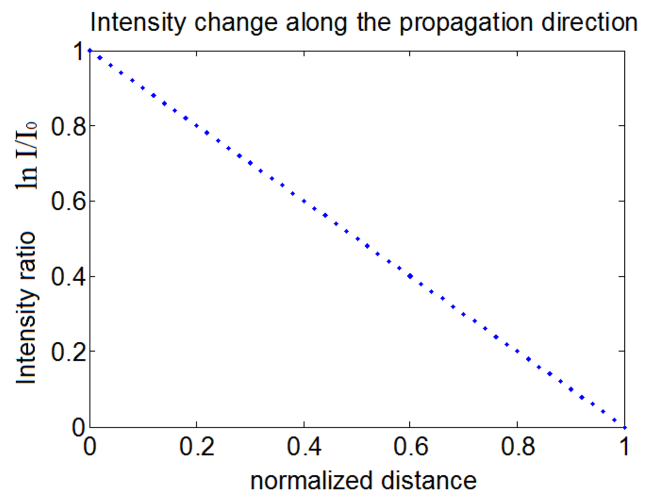

(b) intensity ratio change

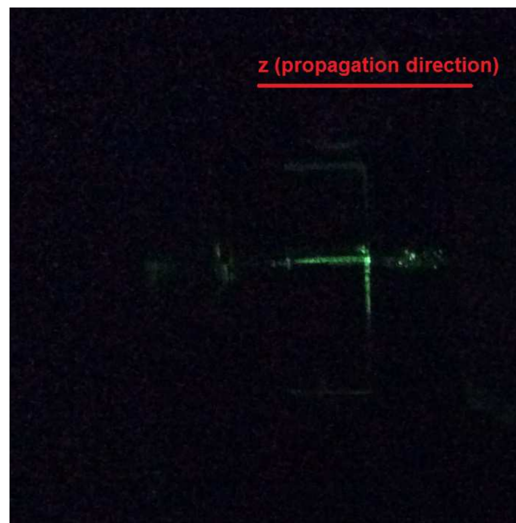

(c) experimental setup

Figure 2.17: Scattered light measurement. (a) Schematic diagram of the scattered light measurement; (b) Intensity ratio change along the beam-propagation direction; (c) Experimental setup for the scattered light measurement.

of the intensity difference between the input and output. Limited by the size of the guided mode, measurement may be sensitive to background noises and other scattering losses. Careful calibration and data processing are required for this method.

Chapter 3

Ultrafast Direct Laser Writing System with Adaptive Optics

This chapter begins with a brief introduction to the use of a spatial light modulator (SLM), which provides dynamic control of phase modulation to correct aberrations adaptively. The SLM also helps to improve the cross-section of the written waveguides and facilitates the fabrication of more complex waveguide structures by beam-shaping and steering. After a detail description of the adaptive direct laser writing (DLW) system with the SLM, the experimental fabrication procedures are described. Two different SLM-based methods for aberration correction, namely Shack–Hartmann wavefront sensing and plasma emission aberration sensing, are introduced in this chapter together with their experimental results. It is demonstrated that the quality of the focal spot is improved dramatically by applying the plasma emission aberration sensing method, which allows the fabrication of high-quality waveguides.

3.1 Introduction

Over the past decade, with the rapid development of ultrafast lasers and improved understanding of the laser fabrication mechanisms, different ultrafast DLW systems

have been proposed and demonstrated for the fabrication of various optical waveguides and other devices in different materials. The properties of the written waveguides are dependent on numerous parameters of the DLW system, such as its pulse energy, repetition rate, pulse duration, wavelength, fabrication speed, and the properties of the substrate material.

For all types of DLW systems, aberration correction is always essential during the fabrication process because the quality of waveguides is greatly affected by the focal spot. Ideally, a small and symmetric focus should be used for laser fabrication, but in many cases the shape of the focus is impaired by aberrations. The most common cause of aberrations is the refractive-index mismatch between the objective immersion medium and the processed material.

An aberrated focus leads to asymmetric cross-section of the waveguide. This asymmetry should be avoided as it directly affects the number, shapes and field distributions of the guided modes. An asymmetric cross-section also induces form birefringence, resulting in polarisation-dependent properties of the waveguide. Therefore, various techniques have been developed to obtain appropriate waveguide profiles. For example, the astigmatic beam-shaping technique [42] can be used to adjust the shape of the writing beam. However, high demagnification telescope and complicated alignment are required for the adjustment. Slit beam-shaping technique is also proposed to reshape the beam profile, which is realised by inserting a physical slit before the objective to reduce the numerical aperture (NA) in one dimension [43]. This technique is simple to implement but lacks flexibility – the cross-section is fixed during DLW fabrication unless mechanical adjustment is applied to the physical slit. Multi-scan technique [44] is another option to obtain more symmetric cross-section of the written waveguide, shifting the beam by certain distance between each scan. But this approach results in square cross-sections rather than circular ones, and needs much longer fabrication time.

In this chapter, the use of an SLM in the DLW system for adaptive beam-shaping and aberration correction is demonstrated to create waveguides with better profiles and higher quality. A deformable mirror can also be used for beam-shaping [45], but is less accurate and flexible, especially for aberration correction. Beam shaping with an SLM is straightforward and adjustable during DLW fabrication. This offers a better control of the writing beam and facilitates fabrication of more complicated three-dimensional (3D) waveguides.

3.2 Spatial Light Modulator (SLM)

An SLM comprises an array of pixels (Figure 3.1) whose refractive indices can be controlled individually by applied voltages. When light travels through the device, it is modulated by different optical paths of each pixel on the wavefront. One example is shown in Figure 3.2(a), where a typical phase modulation (modulo 2π) imitates a blazed grating that deflects the light. The actual pattern applied to the phase screen of the SLM is shown in Figure 3.2(b). By applying different patterns, an SLM can be used to achieve more complex phase modulations. SLMs are commonly utilized for beam splitting and shaping. In the demonstrated DLW system, the SLM has three major functions: (1) adaptive slit beam-shaping to achieve optimal focus dimensions for DLW; (2) beam steering and splitting for parallel DLW; and (3) adaptive aberration correction to eliminate the aberration introduced in the system to the writing focus.

3.2.1 Slit Beam-shaping

As discussed in Chapter 2, transverse writing has attracted more attention recently because of its flexibility in writing distance and structures. If the laser beam propagates along the z-axis, take a Gaussian beam for example, the transverse beam waist

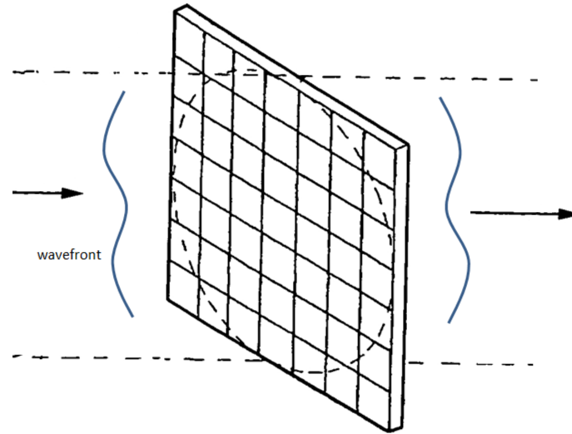

Figure 3.1: Schematic diagram of the wavefront modification on an SLM.

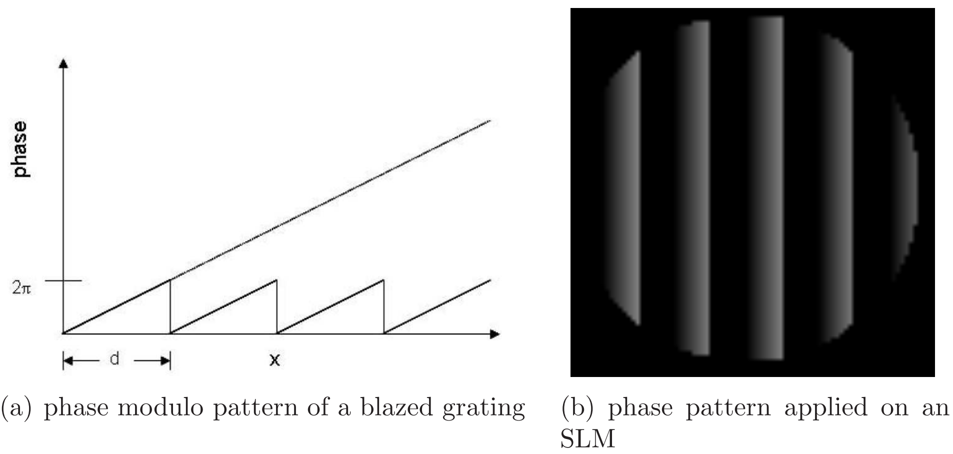

(a) phase modulo pattern of a blazed grating

(b) phase pattern applied on an SLM

Figure 3.2: Phase modulation imitating a blazed grating on an SLM.

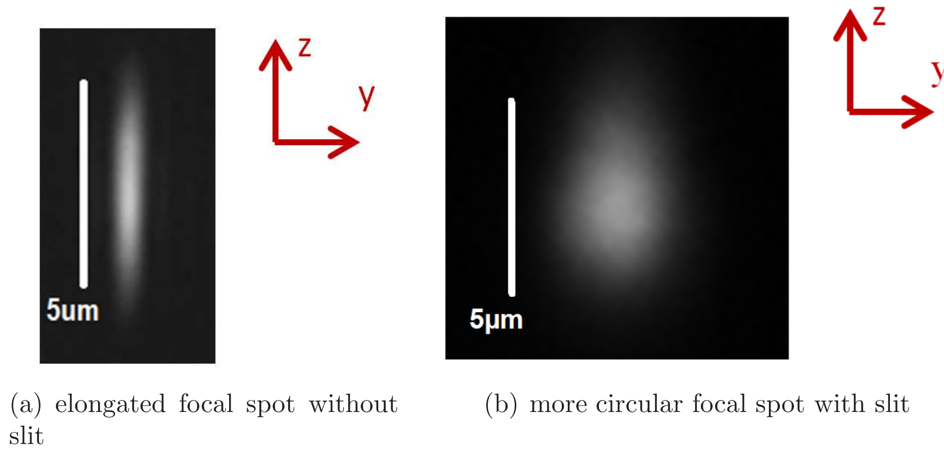

(a) elongated focal spot without slit

(b) more circular focal spot with slit

Figure 3.3: Plasma emission images of a focal spot used for fabrication with and without slit beam-shaping during the DLW process.

(the x or y-axis) of the focus (diffraction-limited) can be presented as follows:

$$w_0 = \frac{\lambda_0}{\pi \cdot NA} \tag{3.1}$$

Here w_0 is the beam waist radius, λ_0 is the laser vacuum wavelength, and NA is the numerical aperture of the focusing lens.

Meanwhile, the Rayleigh distance along the propagation direction (the z-axis) is:

$$z_R = \frac{\pi n w_0^2}{\lambda_0} \tag{3.2}$$

As a result, the waveguide cross-section for transverse writing is elongated by a ratio of:

$$\frac{w_0}{z_R} = n\frac{\lambda_0}{n\pi w_0} = \frac{NA}{n} \tag{3.3}$$

Normally for an NA of 0.6, the cross-section of the waveguide is roughly symmetric (where n is in the range of ∼1.5 such as fused silica). For lower NA values, the cross-section of the waveguide become elongated and highly asymmetric (Figure 3.3(a)).

By inserting a slit before the objective lens (Figure 3.4), the NA of the objective

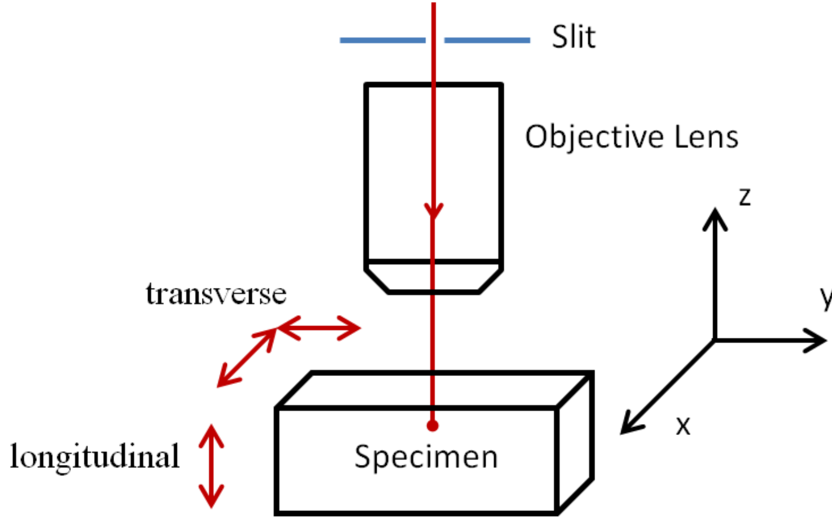

Figure 3.4: Direct laser writing with physical slit before the objective lens.

is effectively reduced in the y-axis. Therefore, the width (y-axis) of the focal spot can be elongated to match its dimension in depth (z-axis). The use of slit normally results in a larger but more circular waveguide cross-section, as shown in Figure 3.3(b).

Instead of using a physical slit, an SLM can be used to achieve adaptive slit beam-shaping for circular waveguides [46]. As there is a background phase profile that corrects the initial flatness for the SLM (Figure 3.5(a)), the actual phase pattern imitating a slit on the SLM is shown in Figure 3.5(b). Compared with a physical slit, the use of the SLM eliminates the requirement for mechanical adjustment and allows the width and orientation of the focus to be changed adaptively, thus greatly improving the flexibility of waveguide fabrication.

However, if only the slit pattern is applied on the SLM, it is observed in the experiment that the resulting laser writing focus has interference with the unmodulated light from the SLM. To avoid this interference, the writing beam is shifted to first diffracted order by a blazed grating. The grating can also be realised using the SLM and is employed to ensure maximum diffraction of light into the first order. A pinhole is inserted on the Fourier plane of the SLM to block the zeroth order. By adjusting the position of the pinhole, only the first diffracted order passes through the pinhole

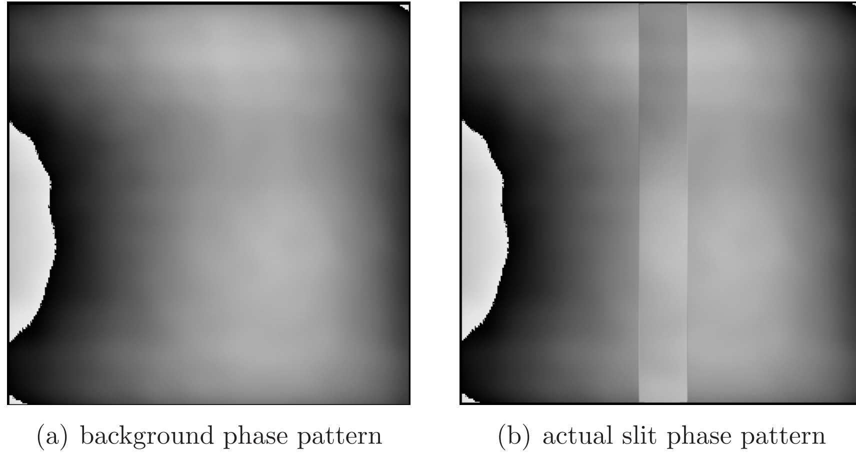

(a) background phase pattern (b) actual slit phase pattern

Figure 3.5: Background phase pattern and actual phase pattern applied to an SLM imitating a physical slit before the objective lens.

and enters the objective lens. As a result, the interference effects are eliminated and more stable writing focus can be obtained.

By adding the phase pattern of the grating to the background phase profile and the phase pattern of a slit, one example of the phase pattern applied to the SLM is shown in Figure 3.6(a). The resulting laser writing focus (Figure 3.6(b)) has a more circular profile than the original focus in Figure 3.3(a).

Different focus dimensions can be generated by varying the width and length of the slit pattern on the SLM. For example, if the slit width is increased and the length is decreased from the dimensions in Figure 3.6(a) to those in Figure 3.6(c), a focus narrower along the y-axis and longer along the z-axis can be obtained (Figure 3.6(d)). As the phase pattern of the SLM is controlled by software, this adjustment can be made during fabrication.

3.2.2 Beam Steering and Splitting

By applying different phase patterns to an SLM, light passes through the system can be steered and/or split. Matlab programs are developed to generate a series of phase patterns in the form of bitmap graphics, which are loaded onto the SLM screen by a

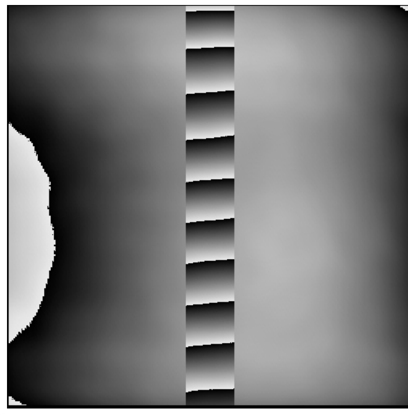

(a) one example of a phase pattern

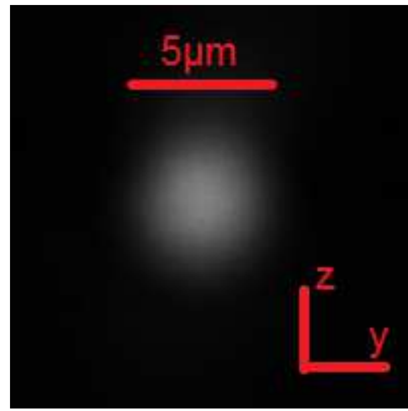

(b) resulting focus of a phase pattern

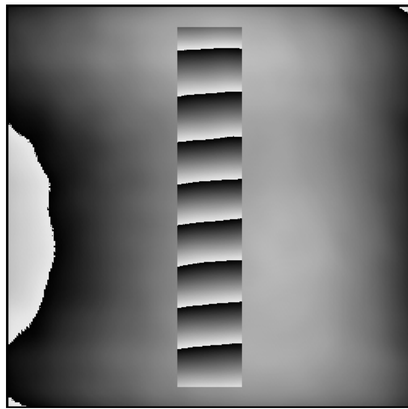

(c) a wider and shorter phase pattern

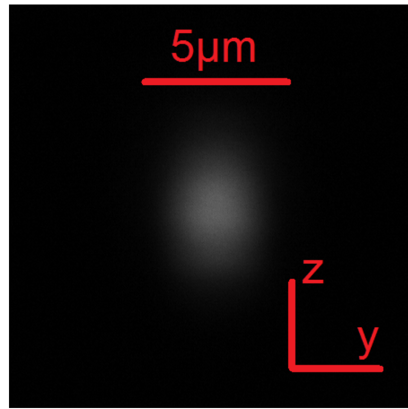

(d) resulting focus of a wider and shorter phase pattern

Figure 3.6: Two different phase patterns applied on the SLM and their resulting focus dimensions.

Labview program.

Two different methods can be used to calculate the required phase patterns for beam steering and beam splitting. The first technique is using phase gratings to steer and split the beam. The period of the grating, Λ, is determined by:

$$\Lambda = \frac{m\lambda_0}{\sin\theta_m - \sin\theta_i} \tag{3.4}$$

where λ_0 is the laser vacuum wavelength, m specifies the order of the various principal maxima, $\sin\theta_m$ is the angle between the diffracted ray and the grating's normal vector, and $\sin\theta_i$ is the angle of incidence.

When light is normally incident on the grating ($\sin\theta_i = 0$), the first order diffracted light has maxima at angles $\sin\theta$:

$$\Lambda = \frac{\lambda_0}{\sin\theta} = \lambda_0 \frac{f}{D} \tag{3.5}$$

where D $(= \sqrt{D_x^2 + D_y^2})$ is the distance between the first order maxima $(D_x,\ D_y)$ and the zeroth order(0, 0).

The angle of the grating, Θ, can be presented as follows:

$$\Theta = \arctan\frac{D_y}{D_x} \tag{3.6}$$

Thus, if a single beam needs to be steered to a position of $(D_x,\ D_y)$, the design of the phase pattern can be calculated from Equation (3.5) and Equation (3.6). Figure 3.7 displays one example of single beam-steering.

Instead of one single writing focus, an SLM can also be used to generate multiple foci for parallel DLW fabrication. To split a beam into multiple ones, the SLM phase screen should be equally divided into the number of desired foci. Each subdivision has a unique phase pattern to steer its corresponding beam to the desired direction.

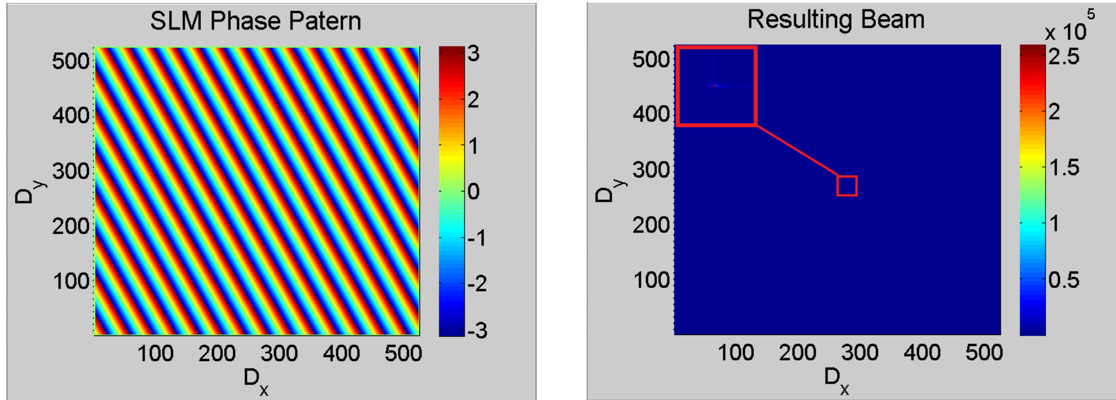

(a) SLM phase pattern for single beam-steering (b) resulting beam after single beam-steering

Figure 3.7: Single beam-steering using the phase grating: (a) the SLM phase pattern, calculated from the desired diffraction offset (D_x, D_y); (b) the resulting intensity distribution, using the designed phase pattern in (a). The x and y-axes present the 525×525 pixels that make up the face of the SLM (the phase screen).

An example of a 3×3 grating-array is shown in Figure 3.8. Note that the intensity of each beam can be modified by adjusting the size of each subdivision (area on the SLM face) or by changing the modulation depth ($[0, 2\pi]$) of each grating.

The use of multiple gratings on the SLM screen is simple and straightforward but has two major drawbacks for practical application. First, each subdivision in the SLM phase screen corresponds to one diffracted focal spot. If certain portion of the SLM screen is not illuminated, the corresponding focal spot will be weakened or disappeared whereas the intensity of all other focal spots maintains. One example is shown in Figure 3.9. For circular pupil, gratings at the corner of the screen can be partially blocked, resulting in weaker focal spots from the original 9-spot array.

The second issue of using multiple gratings to generate multi foci is caused by aberration. Each focal spot of the multiple gratings comes from a different part of the SLM screen with different aberrations, whereas each spot of a phase hologram comes from the entire SLM with the same aberration effect. A phase hologram on the entire SLM screen can be used for more complex beam steering and beam splitting than the grating technique. A phase hologram for a desired far field image can be

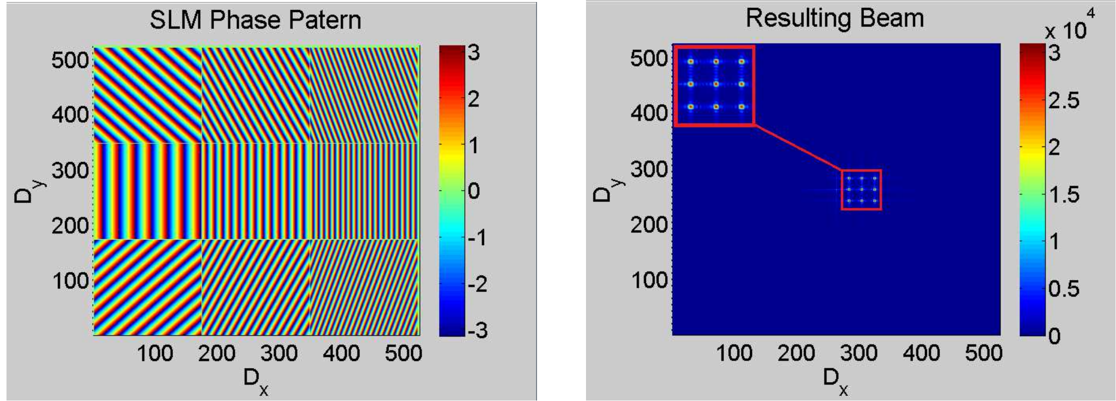

(a) SLM phase pattern for beam-splitting

(b) resulting beam after beam-splitting

Figure 3.8: Beam splitting using multiple phase gratings: (a) the SLM phase pattern, calculated from the desired diffraction direction (D_{xi}, D_{yi}) for beam i in a 3×3 grating-array; (b) the resulting intensity distribution, using the designed phase pattern in (a). The x and y-axes present the 525×525 pixels that make up the face of the SLM (the phase screen).

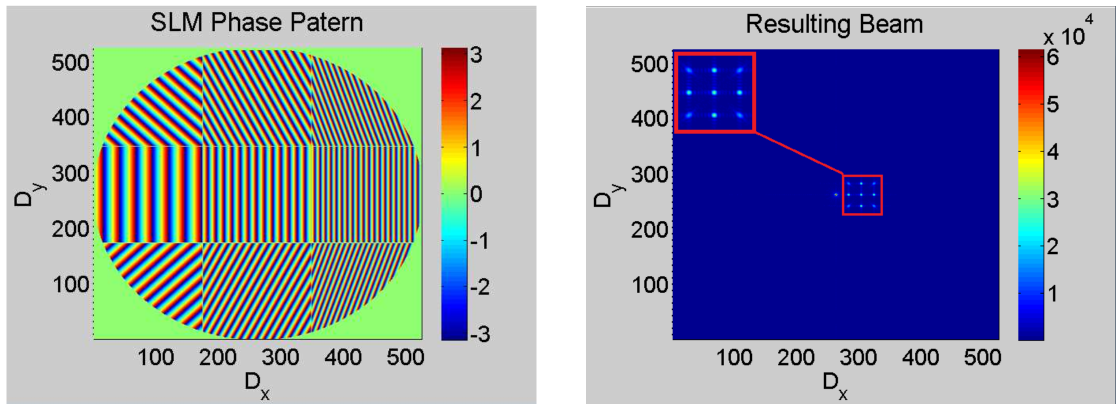

(a) SLM phase pattern with gratings partially blocked

(b) resulting beam with gratings partially blocked

Figure 3.9: Beam splitting with gratings partially blocked in a 3×3 grating-array: (a) the SLM phase pattern for a 3×3 beam array with circular screen size; (b) the resulting intensity distribution, using the designed phase pattern in (a).

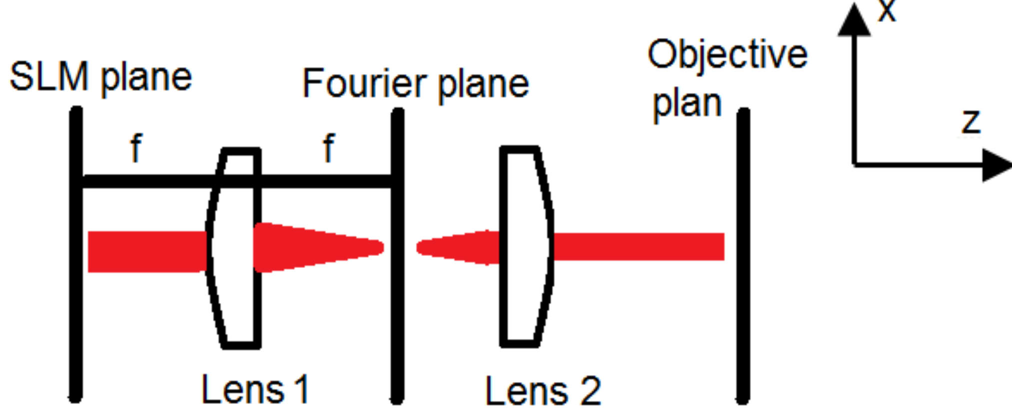

Figure 3.10: Schematic diagram of the multi foci generation using an SLM.

calculated on the basis of a weighted Gerchberg-Saxton algorithm [47]. The desired far field image can either be a single focal spot at a certain position, or an array of multiple spots at predetermined positions. The schematic diagram of the hologram generation is shown in Figure 3.10. Here Lens 1 acts as a Fourier transformer, the field in its back focal plane is the Fourier transform of the field in the SLM plane.

In order to create a specific light field $E(x, y) = |E(x, y)|exp[i\phi(x, y)]$ on the objective plane, the complex field, $F(u, \nu)$, desired in the Fourier plane should be:

$$F(u, \nu) = |F(u, \nu)|exp[i\phi(u, \nu)] = \frac{1}{\lambda_0 f} \int_x \int_y E(x, y) exp[-i\frac{2\pi}{\lambda_0 f}(xu + y\nu)]dxdy \quad (3.7)$$

where f is the focal length of Lens 1.

According to diffraction theory, the complex electric field v_m of each focus m is the sum over the fields from all the N pixels on the SLM plane:

$$v_m = \frac{exp[i2\pi(2f/\lambda_0)}{i} \frac{d^2}{\lambda_0 f} \sum_{j=1,N} |E| exp[i(\phi_j - \Delta_j^m] \quad (3.8)$$

where j refers to the jth pixels coordinates on the SLM plane, N is the total number

of pixels, d^2 is the pixel's area, and Δ_j^m are the individual propagator functions:

$$\Delta_j^m = \frac{2\pi}{\lambda_0 f}(x_j u + y_j \nu) \tag{3.9}$$

If the SLM face is uniformly illuminated and normalized, V_m can be used as a more compact notation of v_m:

$$V_m = \sum_{j=1,N} \frac{1}{N} exp[i(\phi_j - \Delta_j^m] \tag{3.10}$$

The goal of the Gerchberg-Saxton algorithm is to optimise ϕ_js to maximize the modulus of V_m for all focal spots, for a given set of Δ_j^m. The calculation process begins with a random phase function ϕ. V_ms are obtained according to Equation (3.10). As discussed in details in [47], the updated ϕ can be calculated as follows:

$$\phi = \arg \sum_m exp[i\Delta_j^m] \frac{V_m}{|V_m|} w_m \tag{3.11}$$

The resulting ϕ is assigned to the SLM screen for the next iteration. The iterations continue until the error between the intensity distribution of the reconstructed far-field image and the desired focal spots is within a predetermined tolerance.

Note that w_m is a weighting factor for obtaining a high spot uniformity, which equals to 1 at the beginning. For every following iteration, w_m is defined as follows:

$$w_m^k = w_m^{k-1} \frac{\langle V_m^{k-1} \rangle}{|V_m^{k-1}|} \tag{3.12}$$

Here, $\langle \dot{} \rangle_m$ represents the average field magnitude.

An example of a phase hologram applied on an SLM is shown in Figure 3.11. If a hologram of Figure 3.11(a) is applied to the display of the SLM, a 3×3 multi-foci array can be obtained for parallel fabrication as shown in Figure 3.11(b). The

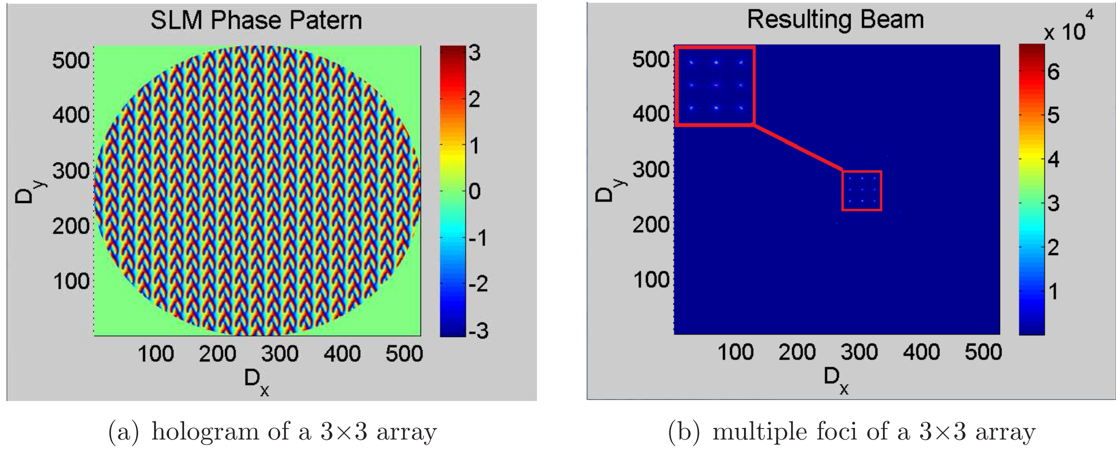

(a) hologram of a 3×3 array (b) multiple foci of a 3×3 array

Figure 3.11: A 3×3 multi-foci array generated by using a phase hologram for beam splitting and steering on the SLM.

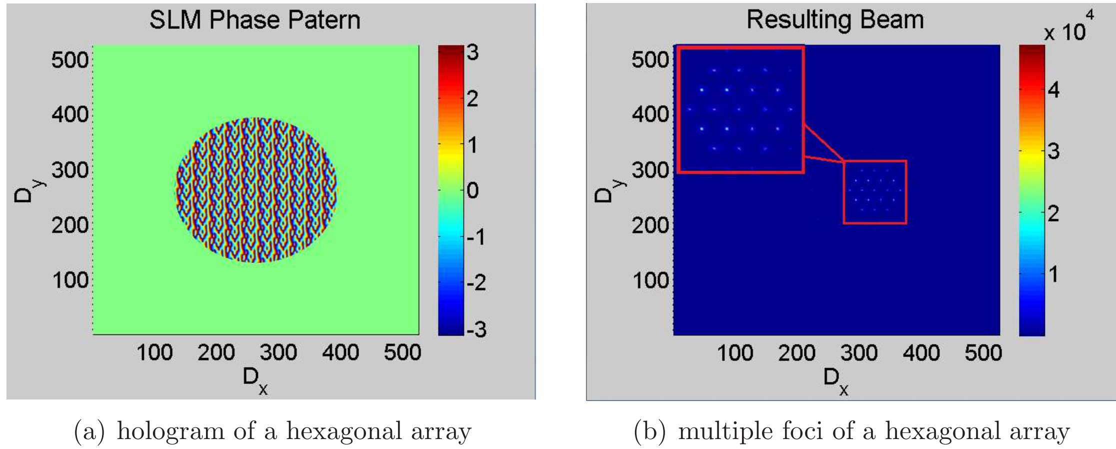

(a) hologram of a hexagonal array (b) multiple foci of a hexagonal array

Figure 3.12: A hexagonal multi-foci array generated by using a phase hologram for beam splitting and steering on a subdivision of the SLM screen.

simulation results indicate that the multi-foci array generated using the hologram is more uniformly distributed than the one using the grating array (Figure 3.8(b)).

Another example of a more complicated multi-foci array using a subdivision of the SLM screen is also displayed in Figure 3.12. As it is shown, even if the illumination of the SLM is limited, the resulting focal spots can still maintain its designed structure with uniform distribution.

3.2.3 Adaptive Aberration Correction

Conveniently, any wavefront aberration can be expressed as a phase function in the pupil plane of the objective lens as an infinite Zernike polynomial series. For example, an arbitrary phase aberration function $\phi(r, \theta)$ would be expressed as

$$\phi(r, \theta) = \sum A_{nm} Z_n^m(r, \theta) \tag{3.13}$$

where m and n are nonnegative integers with $n \geq m$, θ is the azimuthal angle, r is the normalized radial distance $|r| \leq 1$, and A_{nm} are the Zernike coefficients.

For the allowable combinations of n and m, the Zernike polynomials are a sequence of polynomials that are orthogonal on the unit disk, which can be defined by

$$Z_n^m(r, \theta) = \begin{cases} \{\sqrt{2} R_n^{-m}(r) \sin(-m\theta) & \text{if } m < 0 \\ R_n^0(r) & \text{if } m = 0 \\ \sqrt{2} R_n^m(r) \cos(m\theta) & \text{if } m > 0 \end{cases} \tag{3.14}$$

The radial polynomials $R_n^m(r)$ are defined as follows:

$$R_n^m(r) = \sqrt{n+1} \sum_{s=0}^{(n-m)/2} \frac{(-1)^s (n-s)!}{s!((n+m)/2 - s)!((n-m)/2 - s)!} r^{n-2s} \tag{3.15}$$

The orthogonality in the radial part is as follows:

$$\int_0^1 r\sqrt{2n+2} R_n^m(r) \sqrt{2n'+2} R_{n'}^m(r) dr = \delta_{n,n'} \tag{3.16}$$

To simplify these matrices by a single index, a conventional mapping of the two indices n and m to a single index i has been introduced by Noll. Therefore, the phase

aberration function $\phi(r, \theta)$ can be rewritten as:

$$\phi(r, \theta) = \sum A_{nm} Z_n^m(r, \theta) = \sum A_i Z_i(r, \theta) \tag{3.17}$$

The association between $Z_n^m(r, \theta)$ and $Z_i(r, \theta)$ and the first 22 Zernike modes of the aberration term are shown in Table 3.1. For $i = 5$, when $n = 2$ and $m = 2$, it is the astigmatism aberration referred as Mode 5 in the following discussion. Modes 1, 2 and 3 correspond to the piston, tip and tilt, which only represent shift in the position rather than curvature in the wavefront. Therefore, the first 3 modes are usually not counted as normal aberrations and only $n \geq 4$ are considered for aberration correction in the system.

If an aberration compensation, $\phi^c(r, \theta)$, is applied, the resulting corrected phase-aberration function $\phi'(r, \theta)$ is given by:

$$\phi'(r, \theta) = \phi(r, \theta) - \phi^c(r, \theta) \tag{3.18}$$

which should be minimised for optimal aberration correction.

In practice, $\phi^c(r, \theta)$ can either be one single overall phase value or sum of individual aberration modes as follows:

$$\phi^c(r, \theta) = \sum A_i^c Z_i(r, \theta) \tag{3.19}$$

Here A_i^c are the Zernike coefficients applied for aberration compensation.

i	n	m	$Z_i(r,\theta)$	Aberration term
1	0	0	1	Piston
2	1	1	$2r\cos\theta$	Tip (Tilt x, about y axis)
3	1	-1	$2r\sin\theta$	Tilt y, about x axis
4	2	0	$\sqrt{3}(2r^2-1)$	Defocus
5	2	-2	$2\sqrt{3}r^2\cos(2\theta)$	Astigmatism y (45°)
6	2	2	$2\sqrt{3}r^2\sin(2\theta)$	Astigmatism x (0°)
7	3	-1	$2\sqrt{2}(3r^2-2r)\cos\theta$	Coma y
8	3	1	$2\sqrt{2}(3r^2-2r)\sin\theta$	Coma x
9	3	-3	$2\sqrt{2}r^3\cos(3\theta)$	Trefoil y
10	3	3	$2\sqrt{2}r^3\sin(3\theta)$	Trefoil x
11	4	0	$\sqrt{5}(6r^4-6r^2+1)$	Primary Spherical
12	4	2	$\sqrt{10}(4r^4-3r^2)\cos(2\theta)$	Secondary Astigmatism x
13	4	-2	$\sqrt{10}(4r^4-3r^2)\sin(2\theta)$	Secondary Astigmatism y
14	4	4	$\sqrt{10}r^4\cos(4\theta)$	Tetrafoil x
15	4	-4	$\sqrt{10}r^4\sin(4\theta)$	Tetrafoil y
16	5	1	$2\sqrt{3}(10r^5-12r^3+3r)\cos\theta$	Secondary Coma x
17	5	-1	$2\sqrt{3}(10r^5-12r^3+3r)\sin\theta$	Secondary Coma y
18	5	3	$2\sqrt{3}(5r^5-4r^3)\cos(3\theta)$	Secondary Trefoil x
19	5	-3	$2\sqrt{3}(5r^5-4r^3)\sin(3\theta)$	Secondary Trefoil y
20	5	5	$2\sqrt{3}\cos(5\theta)$	Pentafoil x
21	5	-5	$2\sqrt{3}\sin(5\theta)$	Pentafoil y
22	6	0	$\sqrt{7}(20r^6-30r^4+12r^2-1)$	Secondary Spherical

Table 3.1: The first 22 Zernike polynomials.

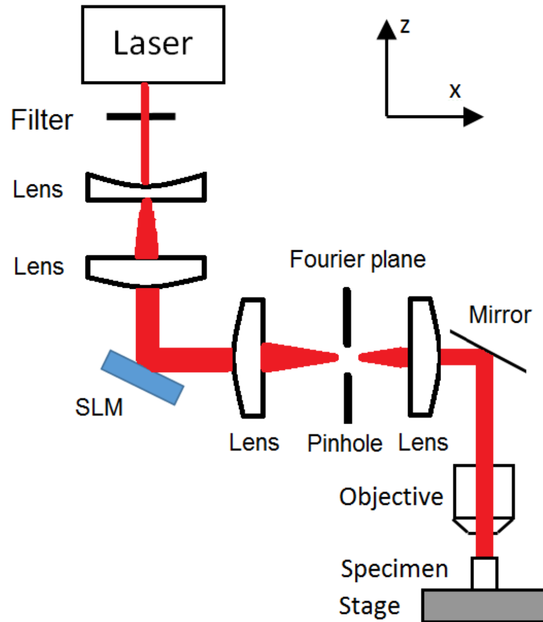

Figure 3.13: Schematic diagram of a DLW system with an SLM.

3.3 Direct Laser Writing Setup and Procedures

3.3.1 Experimental System Setup with the SLM

DLW systems with adaptive optical correction have demonstrated great potential for achieving high-quality 3D waveguides. Figure 3.13 shows the schematic diagram of a DLW system with an SLM. The output of the laser beam is expanded and directed onto an SLM, which is used to modulate the phase of the wavefront of the light. The SLM and the pupil plane of the objective are imaged onto one another by a 4f system. A pinhole is placed in the Fourier plane of the SLM. As discussed in Section 3.2.1, the pinhole eliminates interference effects and ensures only the first diffracted light is used for fabrication.

The actual experimental setup for the DLW fabrication system with SLM is shown in Figure 3.14. The femtosecond laser (Solstice-100F, 100 fs pulse width, 1 kHz repetition rate, 780 nm - 820 nm wavelength) has two outputs: the Mai Tai (S1) output, which provides low-energy power for system alignment; and the regeneratively

amplified (Regen) (S2) output, which is used for high-energy fabrication processes. A half-wave plate and a polariser are inserted after the laser to control the output power. The neutral density filter (ND filter) is used to reduce the power of the laser output. The beam is then expanded (using L1 and L2) and directed to an SLM, which modulates the wavefront of the light. The beam splitter (BSC), L3, L4 and a charge-coupled device (CCD) camera CCD 2 are only used for alignment (not fabrication) for checking the reflected light. The output of the SLM is imaged (using L5 and L6) to the pupil plane of the microscope objective (20X, Zeisis Plan Neofluar with 0.5 NA). A pinhole is placed in the Fourier plane of the SLM. In this configuration, the SLM can be used for adaptive aberration correction and beam-shaping [48, 49], thereby greatly improving the quality of the fabrication focus. The sample is placed and translated on a computer-controlled three-axis translation stage (Aerotech ABL10100 and ANT95-3-V). An LED is mounted beneath the stage and is used to image the sample onto a camera (CCD 1). A colour filter is used in front of CCD 1 to reduce the noise of the imaging. The laser pulses are usually focused 100 μm to 1000 μm below the surface of a transparent sample at different speeds along the x-axis (perpendicular to the laser propagation axis).

Before applying aberration correction, the amount of aberrations in the system should first be evaluated. Two different techniques are applied to measure the aberrations: the Shack–Hartmann wavefront sensing and the plasma emission aberration sensing.

3.3.2 Experimental Procedures

In this section, experimental procedures of DLW are discussed in general. Specific details of different fabrication experiment are provided in the relevant sections. Before the experiment, laser safety training and risk assessment are provided because a high-power laser (Class 4) is used. All potential risks, local rules and protection measures

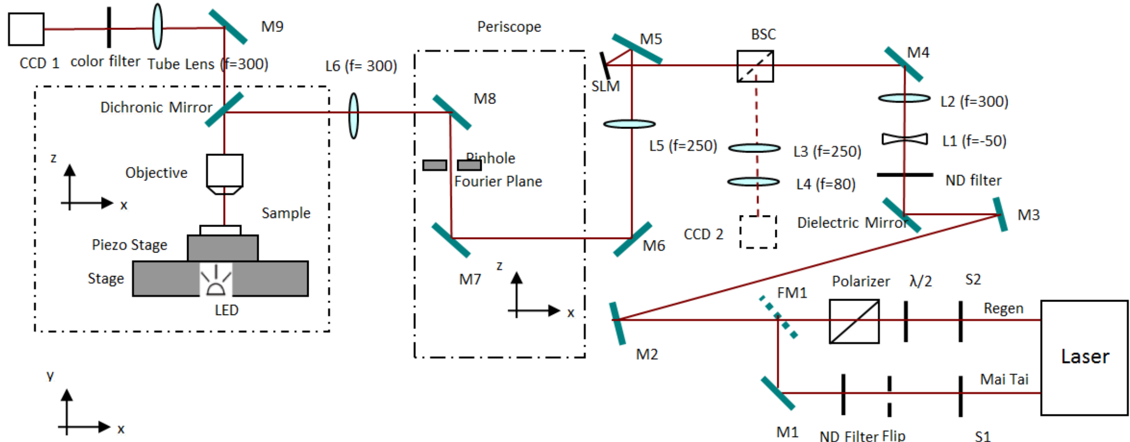

Figure 3.14: Experimental setup of a DLW system with adaptive aberration correction. List of Components: 1. laser 100 fs, 1 kHz, 790 nm; 2. S1, S2 shutter; 3. M1, M2, M3, M4, M5, M6, M7, M8, M9 reflect mirror; 4. $\lambda/2$ rotatable half-wave plate; 5. Polariser Glan-Taylor polariser; 6. FM1, FM2 flip mirror; 7. Dielectric mirror; 8. ND filter neutral density filter; 9. L1, L2, L3, L4, L5, L6 lens: achromatic doublets; 10. BSC beam splitter chamber; 11. SLM; 12. Pinhole on the Fourier plane; 13. LED; 14. Dichronic Mirror; 15. Objective 0.5NA, 20X; 16. Sample; 17. AeroTech Stage; 18. Piezo Stage; 19. Tube lens; 20. Colour filter; 21. CCD Camera.

should be carefully studied and fully understood. The experimental setup in the lab is arranged properly to avoid any potential hazards (Figure 3.15). The original setup was developed by other research members of the team, but I am able to align and calibrate the existing setup, and fabricate waveguides using the DLW system with adaptive optics.

The experimental procedure comprises three main parts: equipment alignment, SLM hologram generation and ultrafast-laser-writing waveguide fabrication. A Labview program is used for the alignment and fabrication, including the control of the laser, the SLM hologram, the settings of the camera, and the stages.

The first step of the experiment is the alignment of the DLW system. During this step, it is essential not only to achieve good experimental results but also to ensure that the whole system remains stable and comparable between different experiments. The beam emitted from the femtosecond laser is aligned through all of the optical components: filters, polarizers, lenses, the SLM, the objective, mirrors, the sample

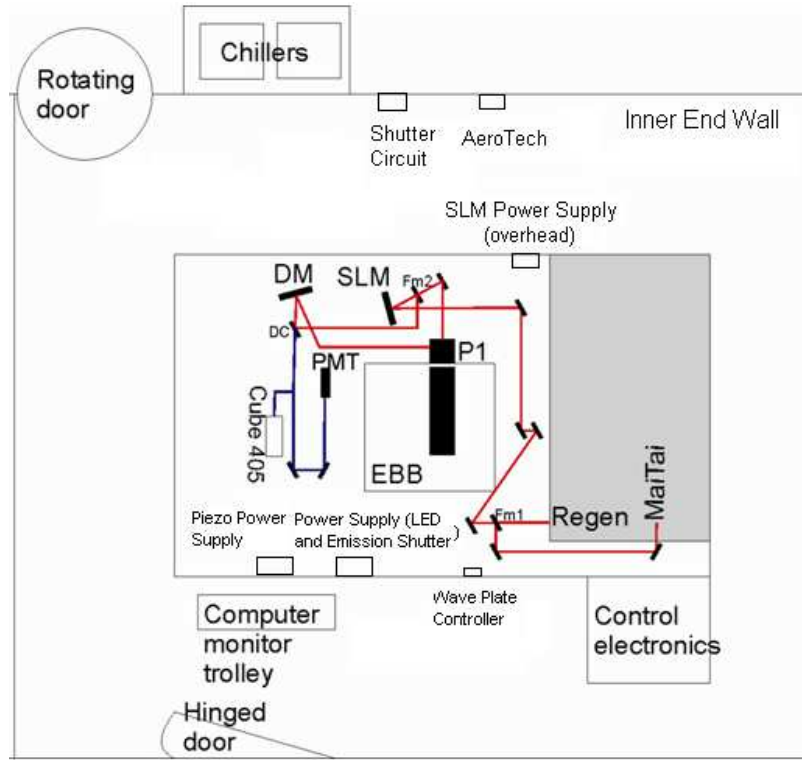

Figure 3.15: Lab layout of a DLW system.

and the CCD camera (Figure 3.14). Note that the Mai-Tai is used for system alignment with low energy (FM1 flip). Beam paths are checked with a paper target by aligning each component using the infrared viewer. Repeat checking is done to "walk" the beam through the centre of all components.

The SLM is first aligned until the beam hits approximately its centre. The following steps are then required to match the pupil planes of the SLM and the objective lens.

1. Detach the CCD camera and place it on position CCD 2 in the diagram.

2. Place a mirror on the sample stage (i.e., under the objective).

3. Move the objective until the mirror is approximately in the focal plane.

4. On the LabView software under Control SLM apply Mode 5, magnitude 1rad and flatness correction off. This should display a cross shape on the SLM

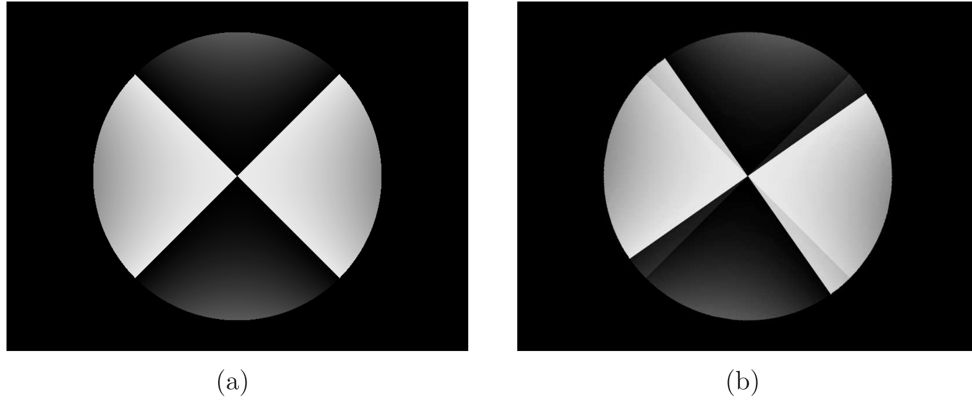

Figure 3.16: The SLM cross phase pattern for alignment: (a) The original SLM cross phase pattern; (b) The SLM diffraction pattern.

(Figure 3.16(a)). On the CCD display, there are two images of the diffraction pattern (Figure 3.16(b)).

5. Move the objective laterally until both images of the diffraction pattern coincide.

6. Replace the CCD camera to its original position CCD 1.

7. Save the SLM holo parameters to the default path.

The position of the pinhole should also be adjusted on the Fourier plane of the SLM. As it mentioned before, the pinhole in the DLW system is used to block the zeroth order of the output, which eliminates the interference with unmodulated light passing through the SLM. Depending on the structure of the waveguides, different phase patterns (holograms) are applied on the SLM. The GerchbergSaxton algorithm is used to calculate the hologram for beam shaping.

Before fabrication, the sample (a block of glass , KDP, $LiNbO_3$, or any other transparent materials) is carefully cleaned and attached to a microscope slide on top of the piezo stage. Bubble wrap and an air conditioner can be used to cover the laser system to prevent airflow and stabilize the temperature. The Labview control program is opened on the computer; this program has four control panels, which control the laser, the SLM, the CCD camera and the AeroTech stage, respectively.

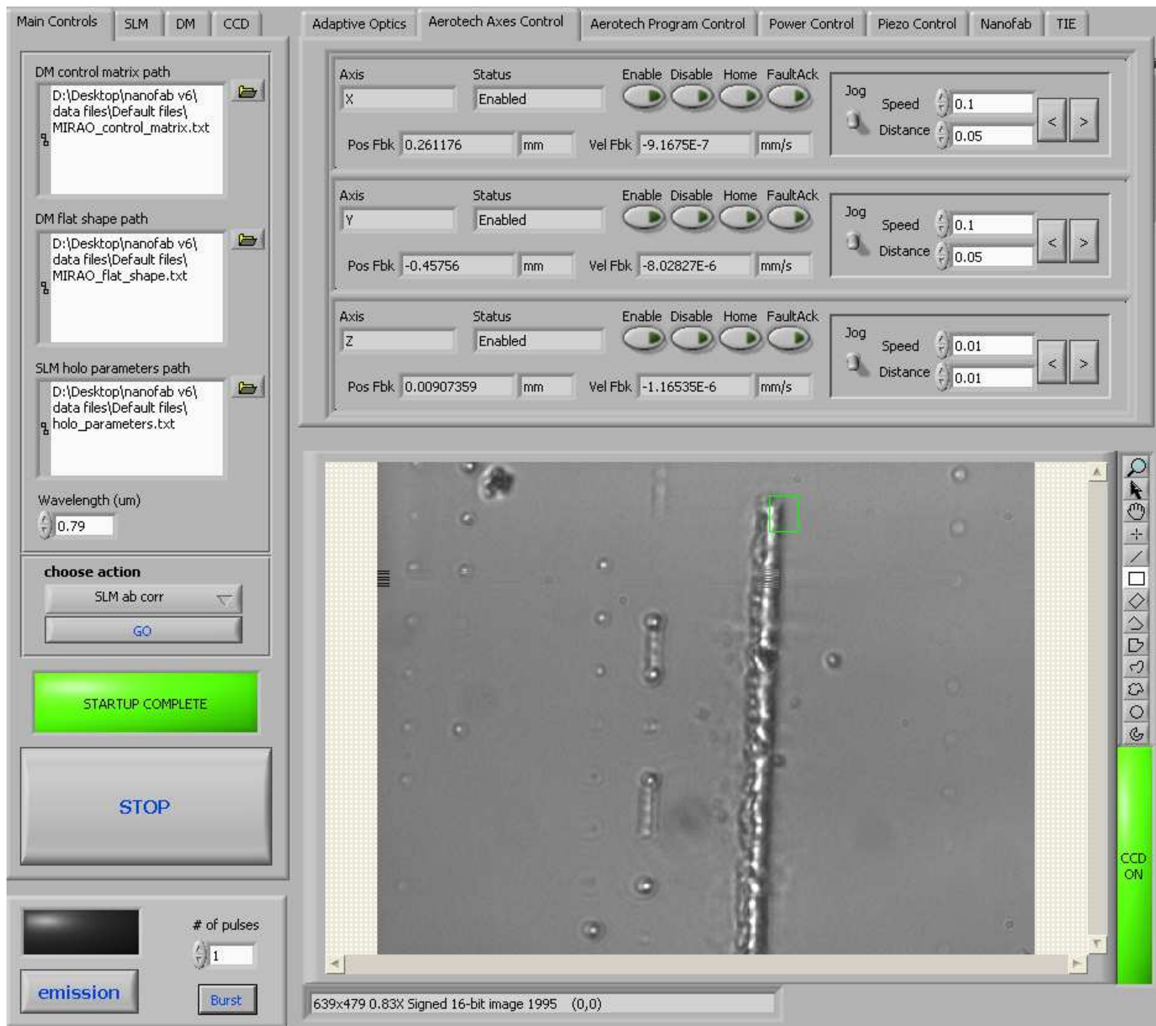

Figure 3.17: Main control user interface of the Labview program for DLW. The left side is the main control panel, the upper-right corner shows the Aerotech control and the lower-right corner shows the CCD image.

When the program is open, its main control panel is shown in Figure 3.17. There are four tabs on the top left: Main Controls, SLM, DM and CCD. DM is not used at all for the purposes of this experiment. There are also tabs on the top right. The upper-right corner of the interface shows the Aerotech control (default), the laser power control, or the SLM pattern display. The lower-right corner shows the CCD image of the sample. On the upper-right, by choosing between tabs, different user interfaces are shown during the fabrication (Figure 3.18).

The waveguide-writing procedure is as follows:

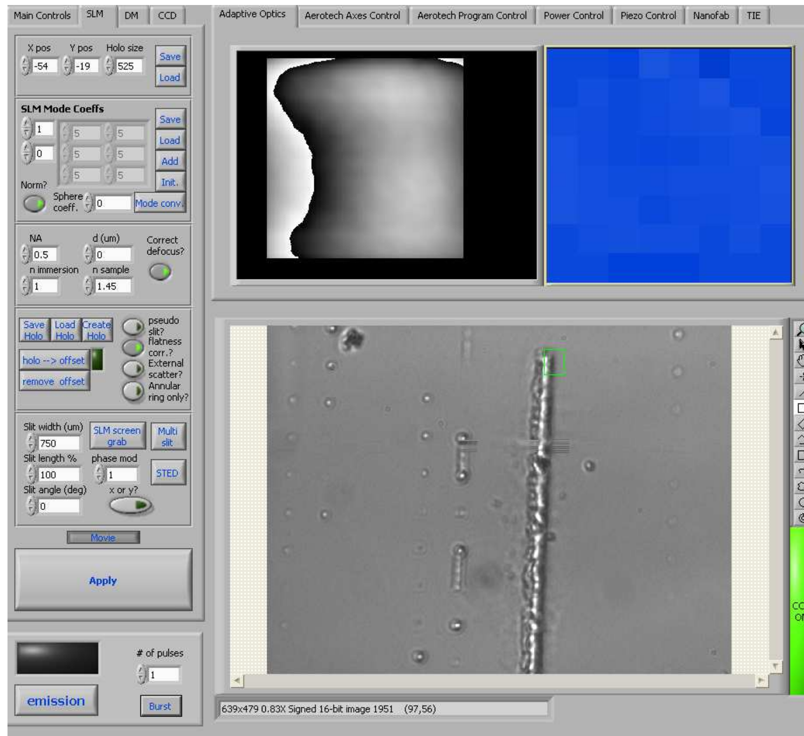

(a) Left: SLM control; Upper-Right: SLM display

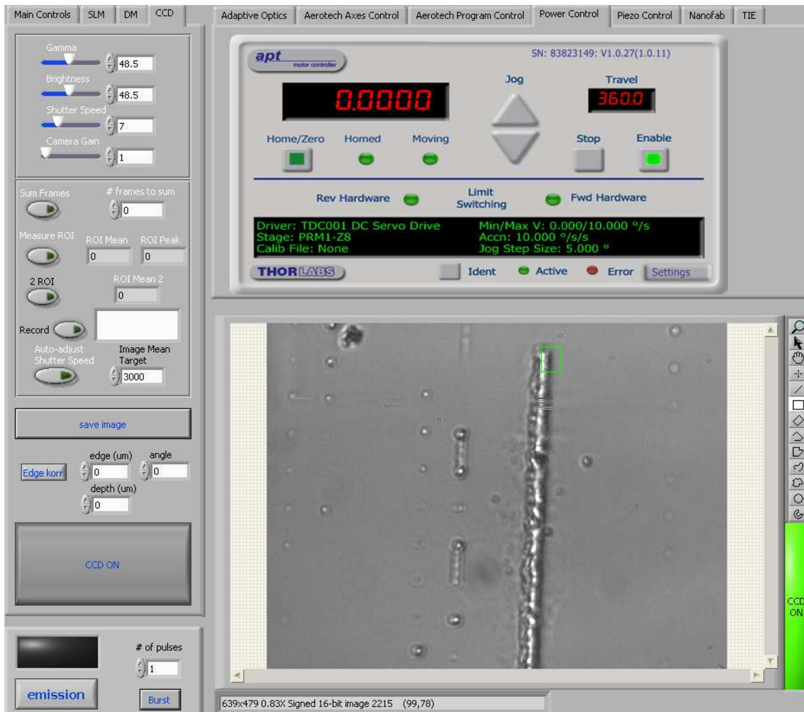

(b) Left: CCD control; Upper-Right: Power control

Figure 3.18: Different user interfaces of the Labview control program for the DLW system.

1. Turn on the laser.

2. Align the sample. The CCD camera is used to monitor the sample. Both transmission imaging and back reflection of the laser can be used in the system. Align the sample properly to ensure that the sample movement is aligned with the transmission of the stage. Adjust the position of the objective and/or the AeroTech stage to focus on the top surface of the sample. When using the transmission image, if the sample is perpendicular to the laser beam, the sample should remain in focus while it is translated.

3. Aberration correction. Adjust the SLM mode values (normally those of Modes 5, 6, 7, 8, 11, 22 and 37 and the defocus adjustment) using the plasma emission sensing method for aberration correction.

4. Apply the aberration-corrected SLM pattern.

5. Set the appropriate depth at which the waveguide is located in the sample.

6. Execute and modify the AeroTech control code for movement during fabrication.

7. Turn on the Regen output and start fabrication.

Fabrication parameters such as the laser power, scan speed and number of paths (whether single or multiple scans) should also be carefully considered and adjusted during the fabrication. For different materials with different waveguide structures at different depths below the surface, the fabrication parameters can be quite different. For example, the power of the laser is one of the most important parameters and should be carefully chosen by rotating the angle of the half-wave plate at the laser output. If the power is too small, very weak waveguides would be fabricated and hardly any light would be guided (Figure 3.19(a)). However, if the power is too high, the processed material is cracked and damaged, which also results in no light-guiding

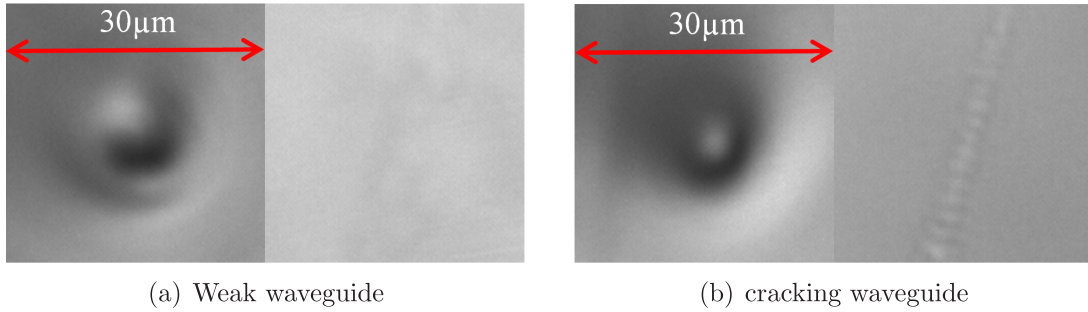

(a) Weak waveguide (b) cracking waveguide

Figure 3.19: Cross-sectional and top-down views of nonworking waveguides written at a depth of 100 μm under the microscope.

(Figure 3.19(b)). Therefore, appropriate pulse energy (power, exposure time, etc.) should be chosen for DLW fabrication.

3.4 Aberration Correction Sensing Methods Using an SLM

3.4.1 Shack–Hartmann Wavefront Sensing

Shack–Hartmann wavefront sensing [50] is a useful method for measuring and correcting aberrations of all types across the whole pupil, and is widely used in adaptive optics systems. A classical Shack–Hartmann sensor (Figure 3.20) comprises an array of lenses (called lenslets) of the same focal length. The wavefront goes through each lens and is focused into a photon sensor array (typically a CCD array or CMOS array). The local tilt of the wavefront across each lens is proportional to the tilt of the corresponding position of the wavefront and can be calculated from the position of the focal spot on the sensor. Any phase aberration can be approximated by a set of discrete tilts. By sampling an array of lenslets, all of these tilts can be measured and the whole wavefront approximated.

A similar idea is applied to the SLM by segmenting its entire aperture into an array of smaller apertures, as shown in Figure 3.21(a). Each aperture comprises a blazed

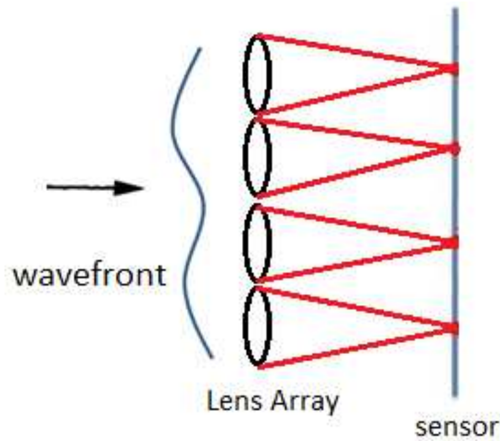

Figure 3.20: Schematic diagram of the Shack–Hartmann sensor.

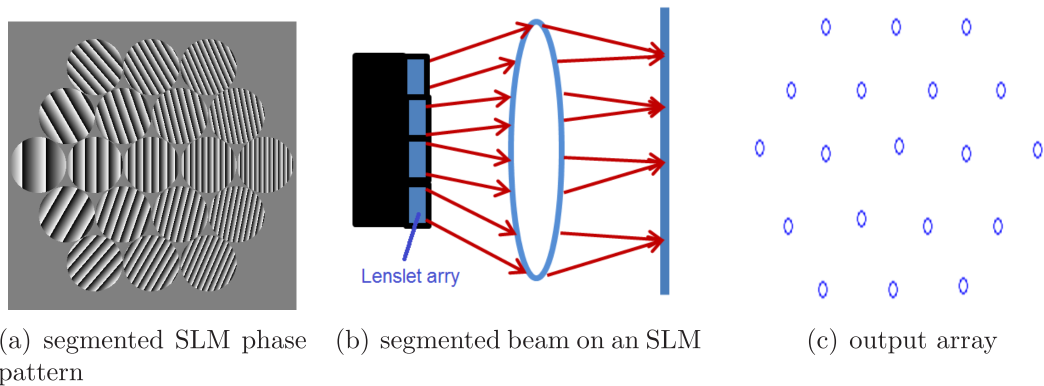

(a) segmented SLM phase pattern (b) segmented beam on an SLM (c) output array

Figure 3.21: SLM with the Shack–Hartmann array.

grating focused into the focal plane by the objective lens, as shown in Figure 3.21(b) and Figure 3.21(c). Without any aberration, the array of spots has no distortion; however, if there is aberration, because each spot comes from a different part of the SLM (therefore the back aperture of the objective), it results in displacement from its original position. The displacement of each spot can be analysed by fitting a linear combination of the Zernike polynomials in order to recover a phase map of the aberration. The phase map can then be subtracted from the original phase pattern on the SLM to correct for aberrations.

To eliminate the effect of camera and imaging magnification, a whole aperture phase pattern is also applied on the SLM, as shown in Figure 3.22(a). The hologram

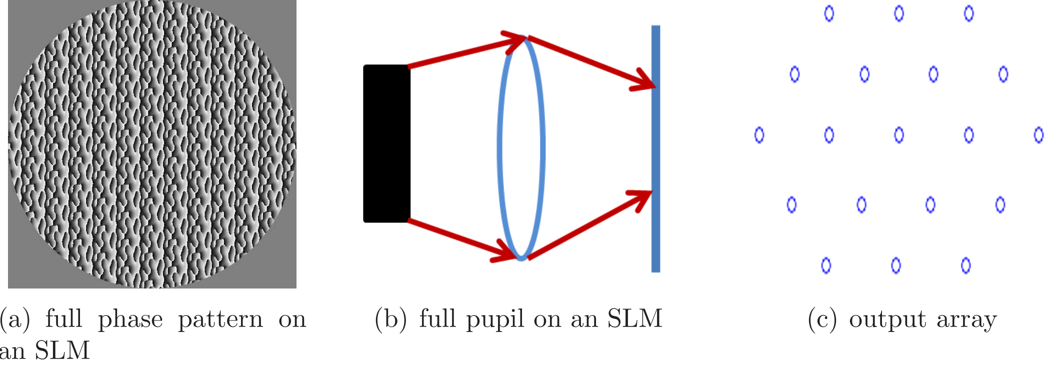

(a) full phase pattern on an SLM

(b) full pupil on an SLM

(c) output array

Figure 3.22: SLM with the whole aperture.

is calculated using the algorithm in [47]. Now each spot in the array comes from the full pupil of the SLM and has the same aberration effect. Aberration has an effect on the shape of the spot but is not affected by the position of the spots. The output array of spots in Figure 3.22(c) can be used as a reference. The displacement of each spot in Figure 3.21(c) compared with Figure 3.22(c) represents the aberration of its corresponding region.

Now let us introduce additional aberration of mode 5 astigmatism ($A_5 Z_5(r, \theta)$, with $A_5 = 1$ and $Z_5(r, \theta) = 2\sqrt{3}r^2 \cos(2\theta)$; refer to Table 3.1). By applying the phase hologram of Figure 3.22(a), the spot array in Figure 3.23(a) is first obtained as a reference. The shape of the spot is distorted because of the aberration, but the geometry of the array should be maintained. Then the segmented phase hologram of Figure 3.21(c) is applied to the SLM, and the resulting spot array is shown in Figure 3.23(b). By comparing the positions of the spots in Figure 3.23(a) and Figure 3.23(b), the resulting displacement is shown in Figure 3.23(c).

Note that the intensity of the diffracted spot decreases with the diffracted distance. As shown in Figure 3.23(b), the rightmost spot is the brightest because it has the smallest diffracted distance. This is mainly caused by phase wrapping of the applied phase pattern [51]. Therefore, instead of the original SLM phase pattern (Figure 3.21(a)), phase randomization is added, as shown in Figure 3.24(a). As a

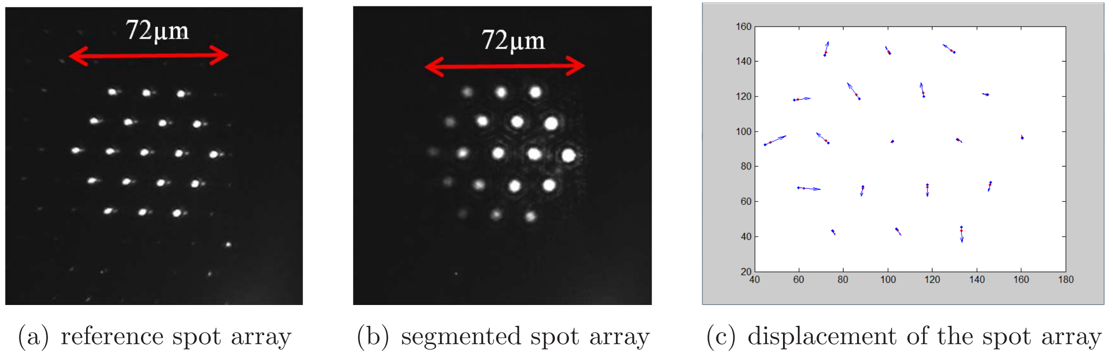

(a) reference spot array (b) segmented spot array (c) displacement of the spot array

Figure 3.23: Shack–Hartmann array with additional astigmatism aberration.

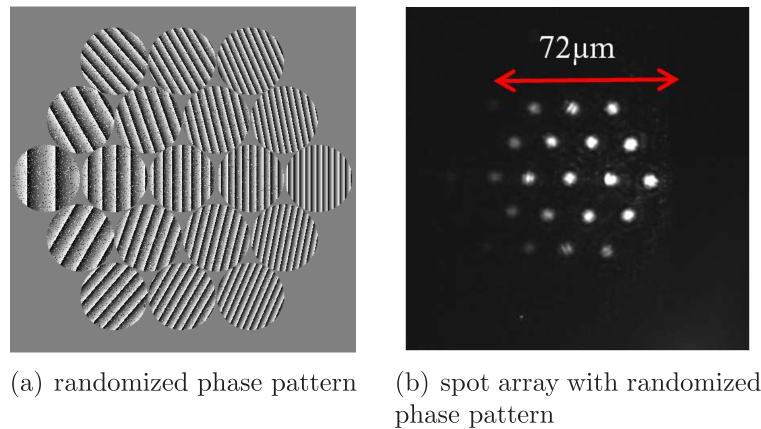

(a) randomized phase pattern (b) spot array with randomized phase pattern

Figure 3.24: Effect of phase wrapping and randomized phase pattern.

result, the array of the spot has a more even intensity distribution (Figure 3.24(b)) compared with that of Figure 3.23(b).

Because of the reduced NA for each small aperture, spots of the Shack–Hartmann array have relatively lower image quality than references (Figure 3.23(a)). Different types of small apertures are therefore tried to find the best structure: circular, rectangular or hexagonal, as shown in Figure 3.25. The hexagonal shape shows slightly better quality, because of its relatively larger NA.

By fitting a linear combination of the first 11 Zernike polynomials to the displacement of the spot array, the aberration can be recovered, as shown in Figure 3.26. Because there are many other aberrations in the system besides the additional astigmatism aberration that is introduced deliberately, the result is not a perfect astigma-

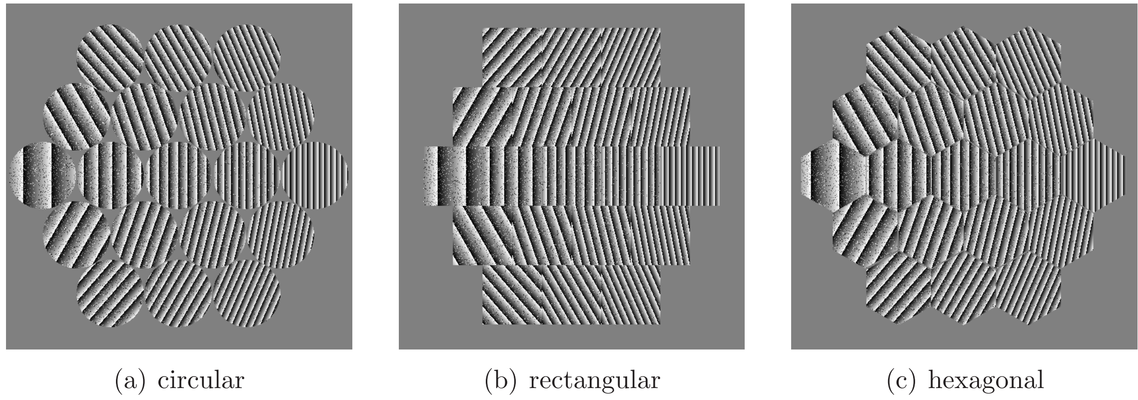

(a) circular (b) rectangular (c) hexagonal

Figure 3.25: Different shapes of small apertures applied on an SLM screen.

Figure 3.26: Aberration correction result. Zernike coefficients from A_5 to $A_1$1 are 1.3, 0.11, -0.06, 0.16, 0.11, 0.02, and 0.21.

tism phase correction.

The difference is also caused by the error in the displacement. During image-processing, it is noticed that the position of the spots cannot be identified very accurately. This is mainly due to the highly reduced NA, leading to low-quality diffracted spots whose exact positions are hard to identify. The lack of accuracy in displacement results in error in the aberration measurement, which makes aberration correction less efficient. Further investigation must be undertaken to increase the NA to achieve higher accuracy.

3.4.2 Plasma Emission Aberration Sensing

To further improve the accuracy of aberration measurement, the plasma emission aberration sensing is also applied in the DLW system. It is presented in [52] that plasma emission intensity is a valid metric for the focal spot quality. During fabrication with high-powered energy, the plasma can be generated by multi-photon absorption and avalanche effects. A well aberration-corrected focal spot corresponds to maximum plasma emission, which is imaged onto the CCD camera. As discussed before in Section 3.2.3, the corrected phase aberration function is given by Equation (3.18).

All other Zernike modes being the same, if the coefficient A_5 is gradually changed from -2.0 to +2.0 by steps of 0.1 to the phase pattern on the SLM, and if the plasma emission of the fabrication focal spot is maximized when $A_5 = -0.5$, then $\phi'(r, \theta)$ is minimized at the same time. This indicates that there is an astigmatism aberration of 0.5 in Mode 5 of the existing $\phi(r, \theta)$. Therefore, the coefficients for all of the Zernike modes that maximize the plasma emission (and minimize $\phi'(r, \theta)$) are the aberration corrections $-\sum A_i Z_i(r, \theta)$ required for the existing $\phi(r, \theta)$.

Figure 3.27 shows results of the plasma emission sensing for different Zernike modes at a fabrication depth of 650μm. All other modes being equal, the coefficient of each Zernike mode (defocus, astigmatism, coma, and spherical) is tested by scanning the optimal mode coefficient (applied by changing the phase pattern on the SLM) when the plasma emission is maximized. The superposition of aberration correction in different modes forms $-\sum A_i Z_i(r, \theta)$ and the test is repeated until the optimal unaberrated focal spot (minimum $\phi'(r, \theta)$) is achieved.

Figure 3.27 shows that the plasma emission intensity varies with the change of coefficient for each mode and is maximized when the aberration is compensated by applying $-A_i$. At a waveguide depth of 650μm, the focal spot has an aberration of +400μm for the defocus; +0.25 for Mode 5; -0.5 for Mode 6 and Mode 8; +0.5 for

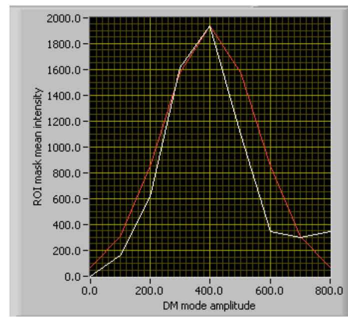

(a) plasma vs. defocus

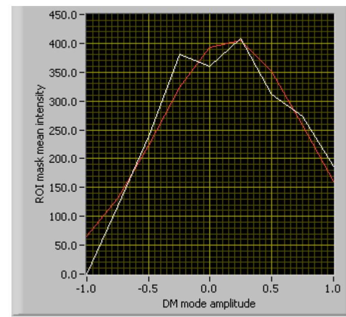

(b) plasma vs. mode 5

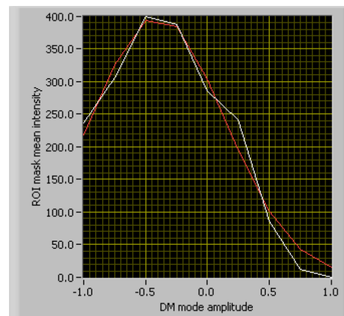

(c) plasma vs. mode 6

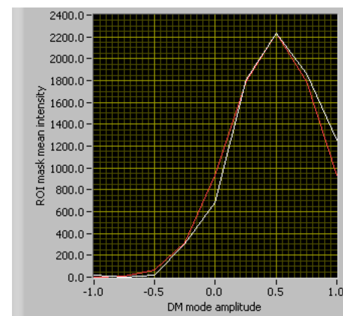

(d) plasma vs. mode 7

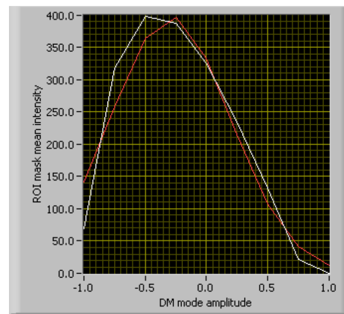

(e) plasma vs. mode 8

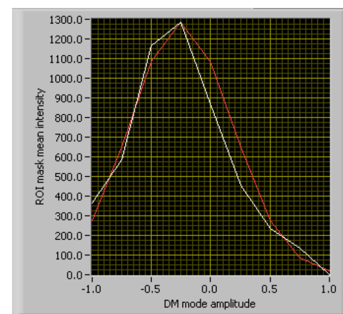

(f) plasma vs. mode 11

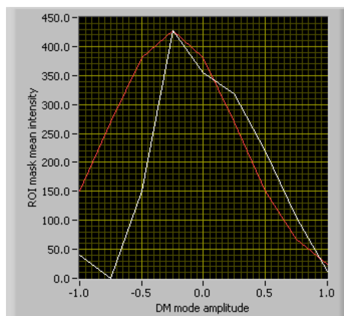

(g) plasma vs. mode 22

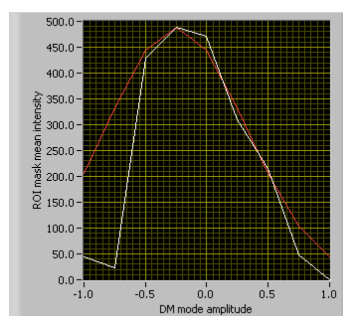

(h) plasma vs. mode 33

Figure 3.27: Plasma emission intensity changes with different Zernike modes at a fabrication depth of 650μm.

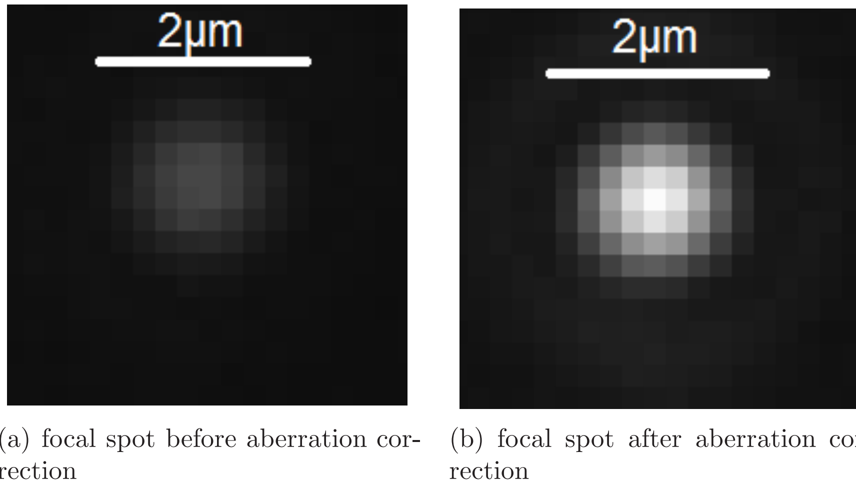

(a) focal spot before aberration correction (b) focal spot after aberration correction

Figure 3.28: Plasma emission sensing for different Zernike modes at a fabrication depth of 650μm.

Mode 7; -0.25 for Mode 11, Mode 22 and Mode 37. The focal spot before and after aberration correction is shown in Figure 3.28. The results indicate that the plasma emission aberration sensing corrects the aberration from the original focal spot, which is significantly defocused and weaker. Plasma emission sensing has higher accuracy and more reliable than Shack–Hartmann wavefront sensing. However, it requires adjustments for each Zernike mode to be made manually and separately.

3.5 Conclusion

In conclusion, the use of SLM in a DLW system facilitates the fabrication of more complex and higher-quality 3D waveguides and offers greater control over the shaping and quality of the focal spot. The use of SLM is especially helpful for aberration correction in the DLW system.

Two different techniques for adaptively correcting aberrations have been demonstrated. The Shack–Hartmann wavefront sensing has the advantage of correcting aberrations in a single step but with less accuracy. Conversely, plasma emission sensing method needs to correct the aberration of each Zernike mode separately, but

offers an advantage of accurate correction and can greatly improve the quality of the focal spot. By controlling different fabrication parameters in the DLW system, a few different waveguides with different structures in different materials have been demonstrated. The DLW system with adaptive optics using the SLM offers a great potential to fabricate high quality optical waveguides with the ultrafast laser writing technology.

Chapter 4

Characterisation of Optical Waveguides

The characterisation methodologies of optical waveguides are discussed in this chapter. A description of the cross-section measurement is first presented. The guide mode is then measured for the evaluation of refractive-index profile, which is essential for the characterisation of the DLW waveguide. An improved propagation-mode near-field method (PMNFM) and an equivalent-step-index (ESI) profile method are proposed for the derivation of the refractive-index profile of the written waveguides. Although there are still many limitations to this technique and challenges facing its implementation, the refractive-index profile of a commercial single-mode fiber and a laser-written waveguide have been successfully evaluated and obtained. In addition, a simple estimation of the refractive index using quantitative phase microscopy has also been briefly discussed. Finally, the insertion and propagation loss of the written waveguide is measured and calculated. The result of the refractive-index evaluation has been discussed and published in [53] and [54].

4.1 Introduction

The characterisation of optical waveguides is crucial for all different types of fabrication processes, not only for the ultrafast direct laser writing (DLW). The refractive-index profile of the written waveguide plays an important role in determining its physical and transmission properties, and is one of the most critical features. The other waveguide parameters, such as the cross-section, guide-mode profile, insertion loss and propagation loss, are also of great interest. The evaluation of fabricated waveguides, compared with the designed features, provides useful information to the DLW system. This feedback can be used to improve the quality of the future design and fabrication processes.

For most of the optical components fabricated by the DLW technique, the measurement of refractive-index change (Δn) is either not clearly mentioned [6, 7, 10, 29] or estimated by measuring the numerical aperture (NA) of the waveguide output [5, 26, 55]. The NA measurement is simple but not accurate, with approximately 30% error [26]. The PMNFM [37] is not used by the previous waveguides probably because of its high-sensitivity to noise. An improved PMNFM with properly data-processing such as Savitzky-Golay filters and curve fittings can be applied to achieve a better accuracy in predicting the characteristics of the waveguides. The experimental results are able to match the simulation algorithms. Unlike other methods, the quantitative phase microscopy can be used to estimate the refractive-index modification during laser writing, which greatly facilitates the fabrication process.

4.2 Cross-section Measurement

Once the waveguide has been fabricated with the ultrafast DLW technique, it is viewed under an optical microscope (either a transmission electron or differential interference contrast microscope). To observe the cross-section clearly, the sample should be side-

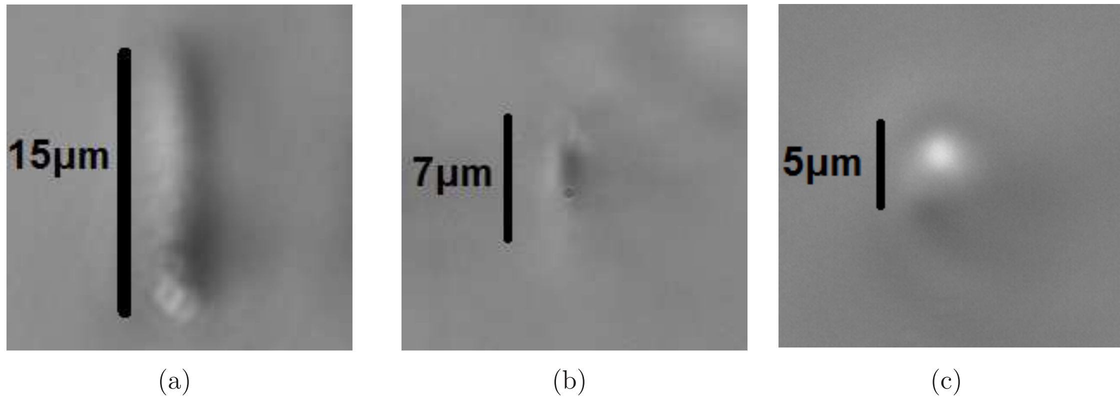

(a) (b) (c)

Figure 4.1: Different cross-sections by modifying the phase patterns on an SLM.

polished and cleaned, if the condition allows. As discussed in Chapter 3, the spatial light modulator (SLM) can be used to modify the cross-section profile of the written waveguides. For different grating patterns with different widths, the resulting cross-sections are different, as shown in Figure 4.1. The aspect ratio can be made to vary over a large range by changing the NA and grating width of the SLM phase pattern. Based on the requirement, different cross-sections can be easily achieved by modifying the SLM pattern using software. The control and measurement of the cross-section of the written waveguides are essential for the characterisation and fabrication of the DLW process.

4.3 Propagation-Mode Near-Field Method (PM-NFM)

Many different methods and techniques on the basis of different principles have been proposed for determining index profiles: these include the reflection method [34], the refracted near-field method [35], and the interferometry method [33]. Unfortunately, most of them have disadvantages such as very sensitive dependence upon the condition of the end face (as in the reflection and refracted near-field methods) or extensive requirements for sample preparation (as in the interferometry method). One of the

most well-known techniques for the evaluation of the refractive-index profile is the propagation-mode near-field method (PMNFM) [37,39,40], which is effective for small and weakly-guiding waveguides.

4.3.1 Theoretical Study

Compared with other techniques, the PMNFM has the advantage of simplicity and independence on the condition of end face. The refractive-index profile can be obtained simply from the measurement of the near-field pattern of a propagation mode, which is the field distribution ϕ from the output end face of the waveguide.

For a weakly-guiding circular waveguide, if the refractive index depends only on the distance from the centre axis, and the permeability of the medium is homogenous and equal to that of vacuum, the optical field intensity of a propagation mode can be described in a scalar wave equation as follows [37]:

$$\nabla^2\phi_r + \{k_0^2 n_r^2 - \beta^2 - \frac{m^2}{r^2}\}\phi_r = 0 \tag{4.1}$$

$$\nabla^2\phi_r = \frac{1}{r}\frac{d}{dr}(r\frac{d\phi_r}{dr}) = \frac{1}{r}\frac{d\phi_r}{dr} + \frac{d^2\phi_r}{dr^2} \tag{4.2}$$

where ϕ_r is the field distribution, r is the distance from centre axis, k_0 is the wavenumber in vacuum, n_r is the refractive-index distribution, β is the propagation constant of a mode, and m is the azimuthal quantum number.

If only the fundamental mode is excited (i.e. $m = 0$), then

$$n_r^2 = -\frac{\nabla^2\phi_r}{k_0^2\phi_r} + n_{eff}^2 \tag{4.3}$$

where $n_{eff} = \frac{\beta}{k_0}$, is the effective refractive index of the waveguide.

If $n_r = n_0 + \Delta n_r$, where n_0 is the substrate refractive index and Δn_r is the change

of the refractive index along the axis, if the change in refractive index is small, then

$$n_r^2 = n_0^2 + 2n_0\Delta n_r + \Delta n_r^2 \approx n_0^2 + 2n_0\Delta n_r \tag{4.4}$$

Therefore Equation (4.3) becomes

$$n_0^2 + 2n_0\Delta n_r = -\frac{\nabla^2\phi_r}{k_0^2\phi_r} + n_{\mathit{eff}}^2 \tag{4.5}$$

By solving for Δn_r and writing $n_r = n_0 + \Delta n_r$,

$$n_r = -\frac{\nabla^2\phi_r}{2n_0k_0^2\phi_r} + \frac{n_{\mathit{eff}}^2}{2n_0} + \frac{n_0}{2} \tag{4.6}$$

where n_{eff} and n_0 are both constant; therefore $\frac{n_{\mathit{eff}}^2}{2n_0} + \frac{n_0}{2}$ can be replaced by a constant C:

$$n_r = -\frac{1}{2n_0k_0^2\phi_r}(\frac{1}{r}\frac{d\phi_r}{dr} + \frac{d^2\phi_r}{dr^2}) + C \tag{4.7}$$

When $r = r_0$ (the core radius at the boundary), in the substrate, the value of C can be determined by

$$C = n_0 + \frac{1}{2n_0k_0^2\phi_{r_0}}(\frac{1}{r_0}\frac{d\phi_{r_0}}{dr} + \frac{d^2\phi_{r_0}}{dr^2}) \tag{4.8}$$

As a result, from Equation (4.7), n_r is only a function of ϕ_r. This means that once the propagation-mode pattern ϕ_r is measured, the refractive-index profile n_r can be uniquely determined.

4.3.2 Simulation Results

The PMNFM is first evaluated by computer simulation. The simulation procedures are shown in Figure 4.2. First, a refractive-index profile *Profile1* ($n_{assumed}$ with certain shape) is assumed. A Pascal program is then used to calculate the theoretical field distribution ϕ_r at the end facet with the assumed profile. The Pascal program is devel-

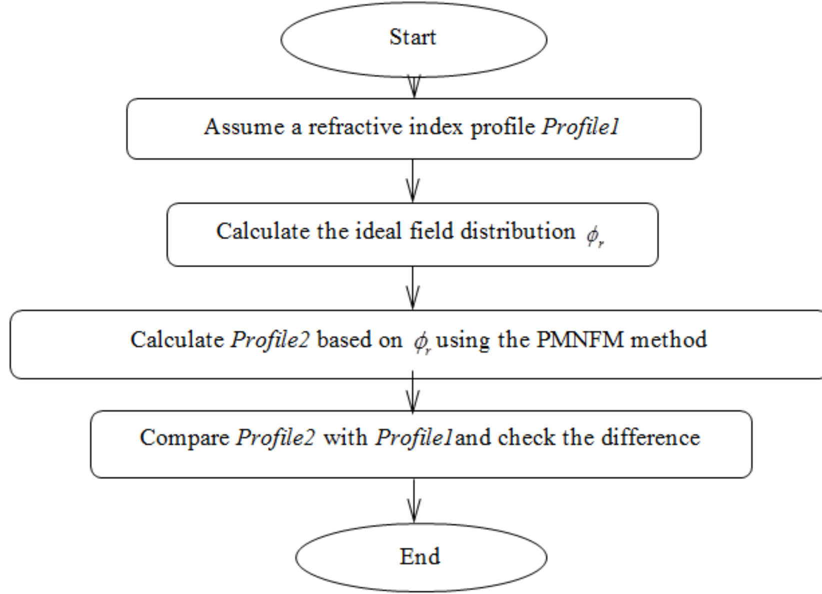

Figure 4.2: Flowchart of the propagation-mode near-field method (PMNFM) simulation.

oped by Harry MacKenzie in [56], and works by applying the finite difference approach to the wave equation to calculate the propagation constant and the field profile with known refractive-index information. Using the theoretical field distribution profile ϕ_r , the refractive-index profile *Profile2*(n_r) is calculated by Equation (4.7). Ideally, without any error, *Profile2* would be exactly the same as *Profile1* $(n_{assumed} = n_r)$. Therefore, by comparing the difference between n_r and $n_{assumed}$, the performance and accuracy of the PMNFM can be evaluated.

Figure 4.3 shows the simulation results for a step-index fiber and a parabolic graded-index fiber. Figure 4.3(a) and Figure 4.3(c) are the theoretical intensity distributions of an assumed step-index and graded-index fiber. It is assumed that the wavelength is 600 nm, the substrate has a refractive index of 1.440, the core has a refractive index of 1.445, and the radius of the fiber is 10 μm. The fiber core is divided into 100 layers for finite difference calculation in the Pascal program.

Figure 4.3(b) and Figure 4.3(d) show the calculated refractive-index profile (red curve), and how it compares with the assumed profile (blue curve). Note here the

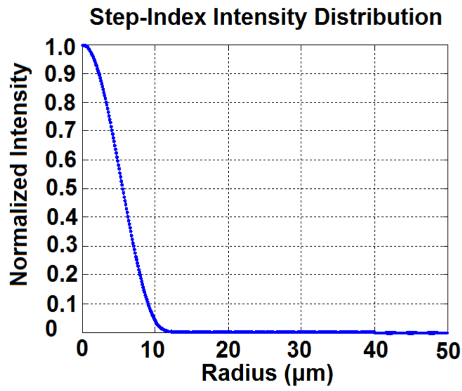

(a) intensity distribution profile of step-index fiber

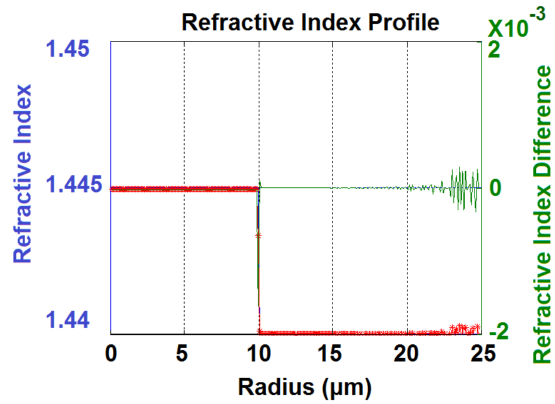

(b) refractive-index profile of step-index fiber

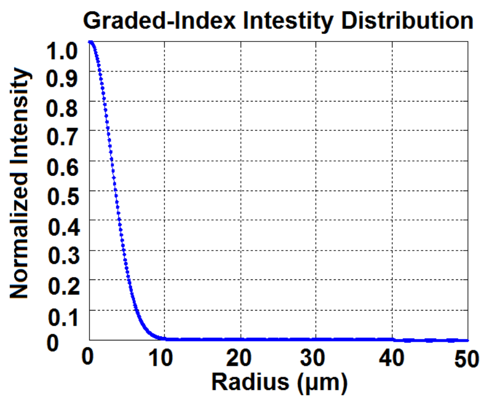

(c) intensity distribution profile of graded - index fiber

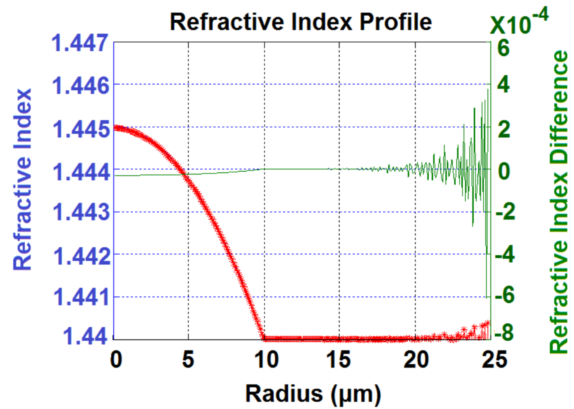

(d) refractive-index profile of graded -index fiber

Figure 4.3: Refractive-index simulation results for the step-index and graded-index fiber. The blue curves in (b) and (d) are the assumed refractive indices $n_{assumed}$; the red curves show the calculated refractive indices n_r; and the green curves show $n_{assumed} - n_r$.

blue curve is not very obvious as it matches very closely with the red curve, which covers it. The green curve shows the difference between the assumed profile and the calculated one. These results demonstrate that the refractive-index profile can be reconstructed using the PMNFM with good accuracy in both cases ($< 5\%$ difference for both the step-index and the parabolic grated-index fiber). Note that there is one extremely noisy point at the edge of step-index fiber in Figure 4.3(b), which is due to the discontinuity of the assumed step-index profile.

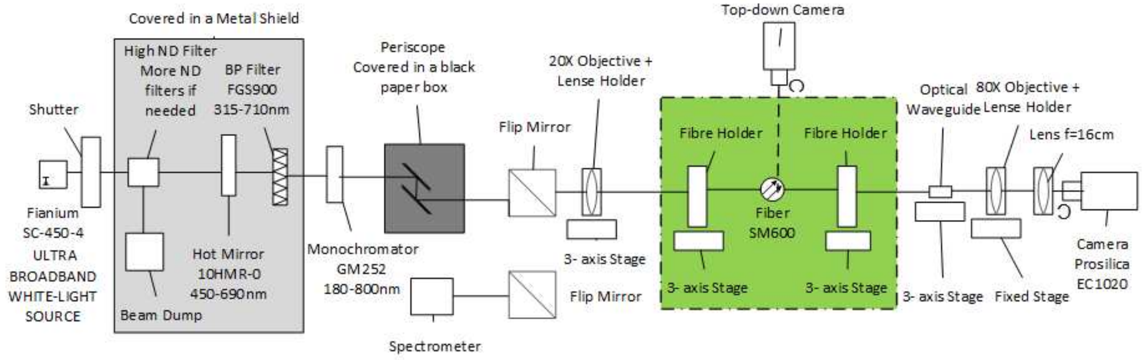

Figure 4.4: Experimental setup for the measurement of output intensity profiles.

4.4 PMNFM Experimental Measurements

4.4.1 Experimental Setup

Based on the proposed PMNFM, if the near-field intensity distribution of the optical waveguide is measured by a charge-coupled device (CCD) camera (as described in Section 2.4.2 in Chapter 2), the related refractive-index profile can be calculated. The experimental setup used to measure the output intensity distribution of an optical waveguide is shown in Figure 4.4. The pulses from an ultra-broadband laser (460-2,200 nm, 4 W, peak spectral power density of 12 mW/nm at 1,064 nm, 40 MHz, and 6 ps) pass a neutral density (ND) filter, a colour filter, a hot mirror and a monochromator to be attenuated and have the right wavelength selected. A power meter and spectrometer are used to monitor the output pulses, which are fed to a 20x objective lens before being coupled into a short piece of single-mode fiber. The single-mode fiber (SM600) is used to provide a uniform source and facilitate the coupling of light into a waveguide afterwards. The output end face is then magnified and imaged by the camera.

Different wavelengths can be selected using the monochromator (600 nm for most of the measurements). The objective lenses, a piece of single-mode fiber and a waveguide sample are all held on 3-axis stages, which help to maximize the flexibility of the

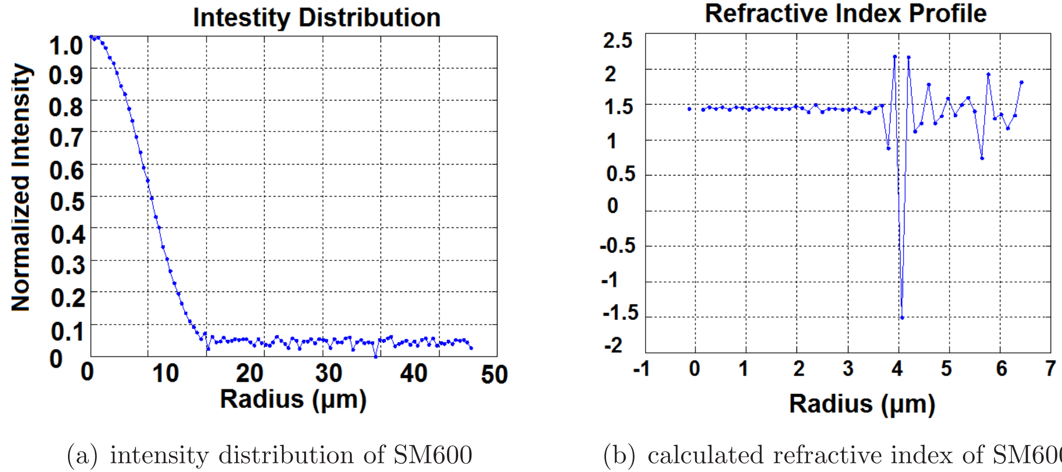

(a) intensity distribution of SM600 (b) calculated refractive index of SM600

Figure 4.5: Refractive-index calculation of an SM600 single-mode fiber using the original PMNFM.

coupling alignment. Another top-down camera is used to help the alignment of the output ends of the fiber and the waveguide.

Before coupling the light into the optical waveguide, the intensity distribution is first obtained directly from the output of SM600, whose refractive-index profile is then calculated. As the refractive-index profile of SM600 is known on the datasheet, the accuracy of the proposed method can be properly evaluated through comparison with the calculated result.

4.4.2 Reduction of Noise

Although a perfect match can be obtained with the theoretical results in simulation, in practice, measurement values are normally far from expectation. Take the Thorlabs SM600 single-mode fiber, for example. The calculated results from the intensity measurement out of this fiber are depicted in Figure 4.5(b), which contains only noise. This result mainly arises from a noisy intensity distribution (4.5(a)) measured from the experiment, compared with the smooth theoretical data in the previous simulation (Figure 4.3(a) and Figure 4.3(c)).

From a theoretical point of view, Equation (4.7) contains a second derivative of the

field profile, which indicates that the calculated refractive-index profile is very sensitive to the noise. A small amount of noise in the field profile introduces dramatic change in the calculated refractive-index profile and even washes out the profile completely. In this case, different algorithms and methods are investigated to reduce noise and further improve the accuracy.

Note that although the direct calculated result is very noisy in Figure 4.5(b), there is still some useful information. For example, an abrupt change appears in the calculated result around 3.8 μm to 4 μm, which probably indicates a fast change in the refractive index around this area. This shows an approximate estimation of the boundary.

For one single CCD image, as shown in Figure 4.6(a), the intensity distribution is recorded across the red line in Figure 4.6(b). Noise in Figure 4.6(c) can be reduced to Figure 4.6(d) if 100 images are averaged instead of one. A Savitzky–Golay filter [57, 58], one of the most popular numerical smoothing filters, is then applied to the resulting average data. The basic idea is to use dynamical polynomials to fit data points within a moving window, which is an effective way to filter high frequencies while maintaining sharp edges at the boundary. Because of the high spatial noise in waveguides, curve fittings are also used to reduce the additional noise. A modified Gaussian mode fit is applied to the data points around the central area and a modified Bessel function to the remaining data points. Here the modified Gaussian function is $y = a_0 * e^{-b_0 * x^2} * (1 + a_2 * x^2 + a_4 * x^4)$, whereas the modified Bessel function is $y = a * K_0(b * x)$. K_0 is the modified Bessel function of the 2nd kind, $K_\alpha(x)$, for $\alpha = 0$.

4.4.3 Experimental Results

Figure 4.7 shows the curve-fitting results of one SM600 measurement, for both the Hermite-Gaussian fit (central) and the modified Bessel function fit (boundary). After

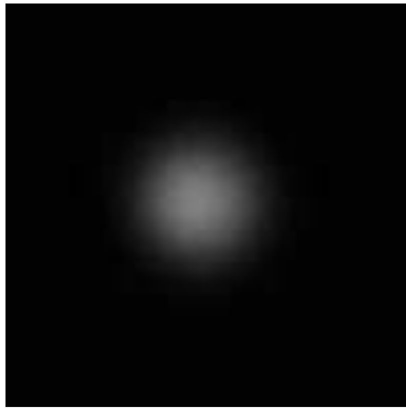

(a) one intensity CCD image

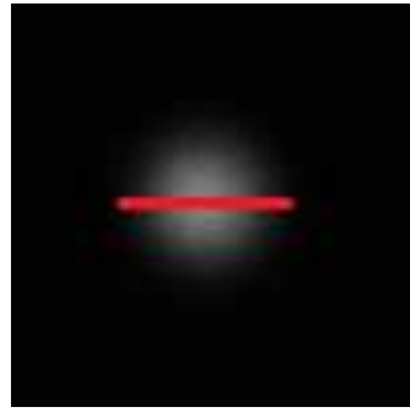

(b) intensity cross the red line

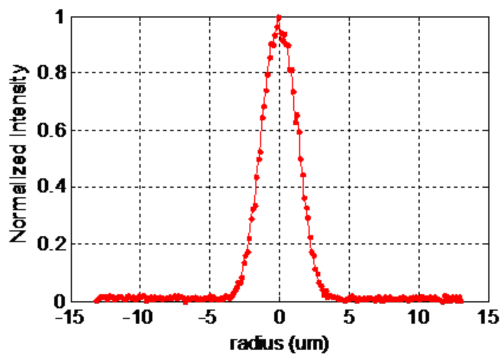

(c) recorded intensity distribution of one CCD image

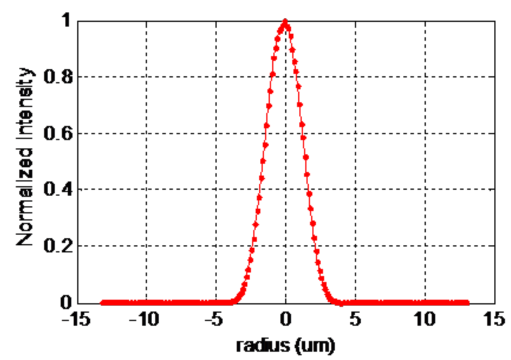

(d) recorded average intensity distribution of 100 CCD images

Figure 4.6: Single and multiple CCD images and their near-field intensity profiles.

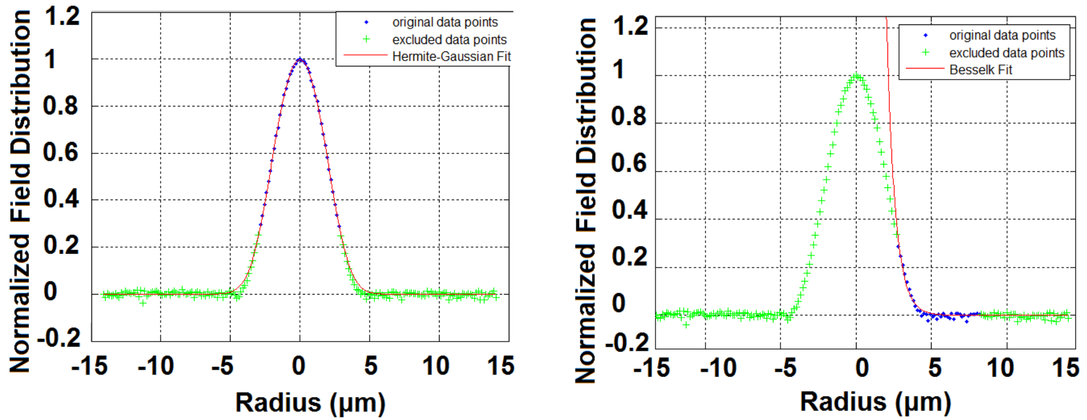

(a) Hermite-Gaussian mode fit to the central data

(b) modified Bessel function fit to the boundary data

Figure 4.7: Curve-fitting of the intensity distribution of an SM600 single-mode fiber.

applying the filter and curve fitting methods, the re-calculated refractive-index profile n_r of SM600 is now shown by the red curve in Figure 4.8(a). Compared with the real estimated refractive-index profile from the manufacturer (blue curve), the difference is small with a mean squared error (MSE) of 5.8×10^{-5}. The calculated field distribution ϕ_r has a MSE of 8×10^{-4} , when compared with the experimental data. The estimated numerical aperture (NA) is 0.14, which matches the 0.10-0.14 value on the datasheet for SM600. The estimated mode field diameter (MFD) is 5.1, close to the value of 5.0 on the datasheet.

After evaluating the improved PMNFM with the SM600 single-mode fiber, the light is coupled into a waveguide fabricated using DLW. By applying the same algorithm to the measured intensity distribution of a waveguide sample, the calculated results are shown in Figure 4.9. The actual field distribution ϕ_r has an MSE of 2.0×10^{-3} compared with the experimental data. The estimated numerical aperture (NA) is 0.11 with maximum refractive-index difference of 4×10^{-3}. The estimated MFD is 3.7, which is close to the experimental data of 3.5.

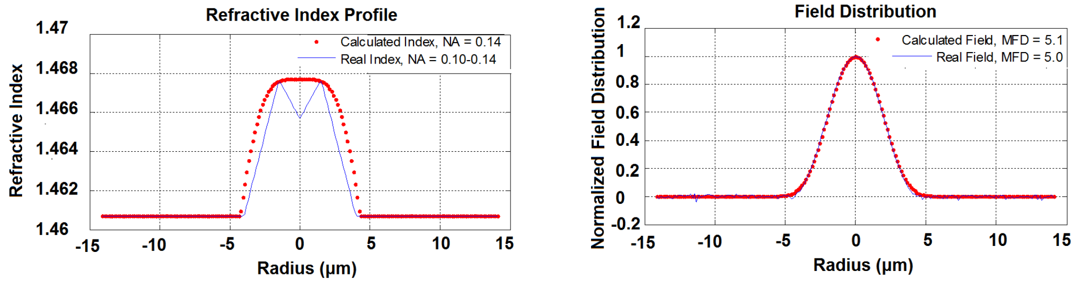

(a) Calculated and Real Refractive Index of SM600

(b) Calculated and Real Field Distribution of SM600

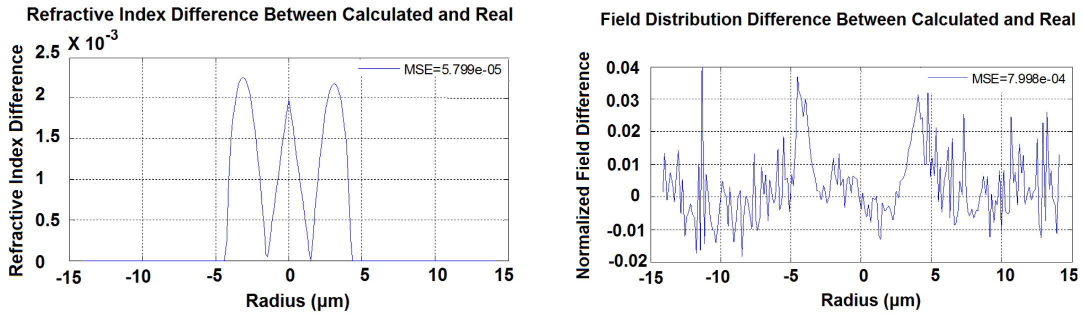

(c) Refractive-Index Difference

(d) Field Distribution Difference

Figure 4.8: Refractive-index calculation of an SM600 single-mode fiber using the improved PMNFM.

4.5 Equivalent-Step-Index (ESI) Profile

In practice, the exact details of the refractive-index profile are difficult to obtain. Fortunately, the propagation characteristics are not sensitive to these details. The idea of an equivalent step index (ESI) [59] is on the basis of the fact that most circularly symmetric single-mode waveguides have similar propagation characteristics to those of a single-mode step-index fiber. This means that the field mode, the propagation constant, and other propagation properties such as the bend loss of a single-mode waveguide can be accurately predicted by its equivalent step-index fiber. Because the characteristics of step-index fiber are simple and well-known, it is convenient to convert different waveguides to their ESI.

From the wave theory of a step-index fiber [60], the field distribution of the fun-

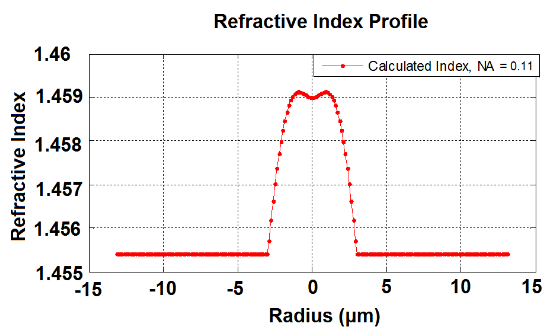

(a) Calculated refractive index of a waveguide sample

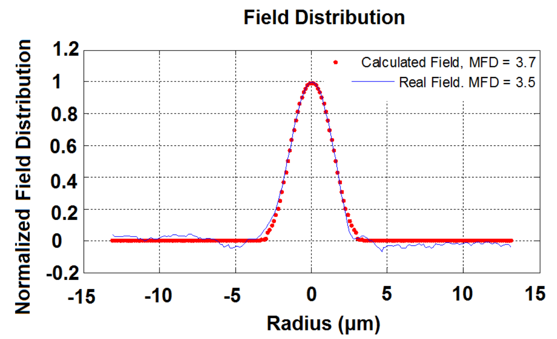

(b) Calculated and real field distribution of a waveguide sample

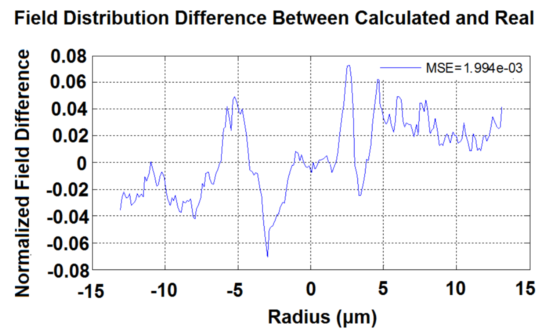

(c) Field distribution difference

Figure 4.9: Refractive-index calculation of a laser-written waveguide using the improved PMNFM.

damental mode in this fiber can be represented as:

$$E(r) = \begin{cases} \frac{J_0(ur)}{J_0(ua)} & \text{if } r < a \\ \\ \frac{K_0(\omega r)}{K_0(\omega a)} & \text{if } r > a \end{cases} \tag{4.9}$$

where

$$\omega = \sqrt{\beta^2 - n_0^2 k_0^2}$$
$$u = \sqrt{n_1^2 k_0^2 - \beta^2}$$
$$\nu = \sqrt{u^2 + \omega^2} = k_0 a \sqrt{n_1^2 - n_0^2}$$

u can be approximated on the basis of [61]:

$$u = u_\infty \frac{\nu}{\nu + 1}\left(1 - \frac{1}{6}\frac{u_\infty^2}{(\nu + 1)^3} - \frac{1}{20}\frac{u_\infty^4}{(\nu + 1)^5}\right) \tag{4.10}$$

Here $E(r)$ is the field distribution, r is the distance from center axis, k_0 is the wavenumber in vacuum, n_0 is the refractive index of the cladding, n_1 is the refractive index of the core, β is the propagation constant of a mode, and the core-cladding interface is at $r = a$. J_0 is the zeroth-order Bessel function, K_0 is the modified Bessel function of the second kind, and $u_\infty = 2.40483$ for the fundamental mode. To obtain the best ESI profile, a and $\Delta n = n_1 - n_0$ are iterated and used to calculate $E(r)$. The resulting $E(r)$ with a minimal MSE compared with the original field distribution is taken as the ESI profile.

The calculated results of applying the ESI method to the SM600 and the waveguide sample are shown in Figure 4.10 and Figure 4.11. The calculated NA (0.14) and MFD (5.0) of the SM600 are very close to values on the datasheet. An MSE of 5.5×10^{-5} is observed between the calculated and real refractive-index profile, while an MSE of 9.6×10^{-4} for the field distribution compared with the real data. For the same

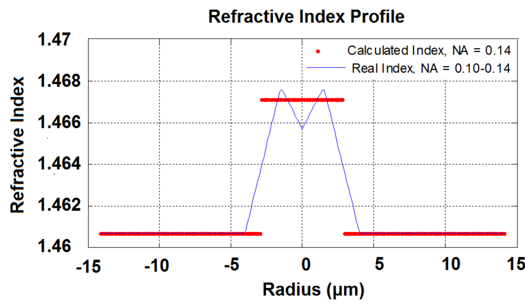

(a) Calculated and Real Refractive Index of SM600

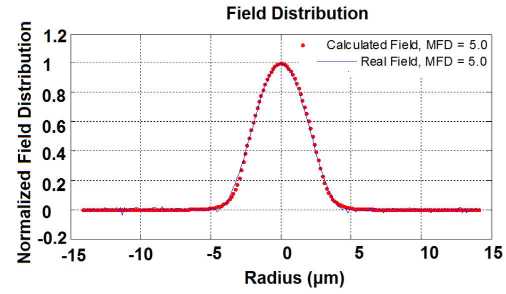

(b) Calculated and Real Field Distribution of SM600

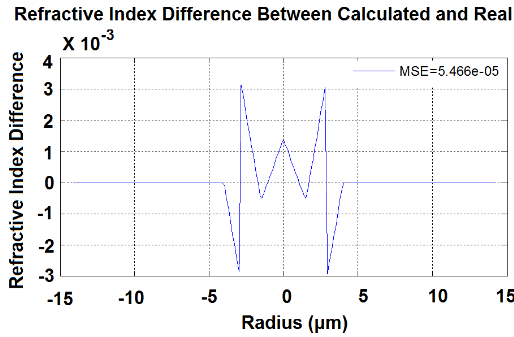

(c) Refractive-Index Difference

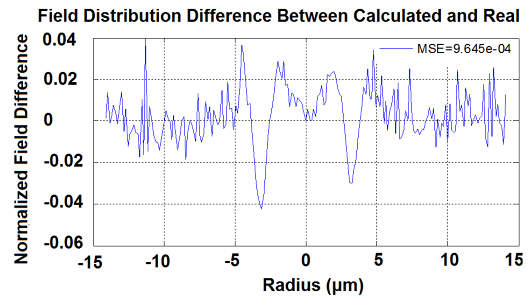

(d) Field Distribution Difference

Figure 4.10: Refractive-index calculation of an SM600 single-mode fiber using the ESI method.

DLW waveguide measured in Figure 4.9, the estimated NA is 0.09 with an MFD of 3.5. The maximum refractive-index difference between the core and the cladding is approximately 2.8×10^{-3}. The calculated field distribution has an MSE of 1.9×10^{-3} compared with the experimental data, showing how accurately the fitted ESI can be used to compute the waveguide model field.

4.6 Quantitative Phase Microscopy

Quantitative phase measurement can also be applied to monitor the refractive index during laser fabrication. There are many microscopy methods that quantify the phase shift which occurs when light passes through a more optically dense object. Normally, three images of the object are captured by transmission microscope, one in focus, one slightly positively defocused and one slightly negatively defocused. These images can

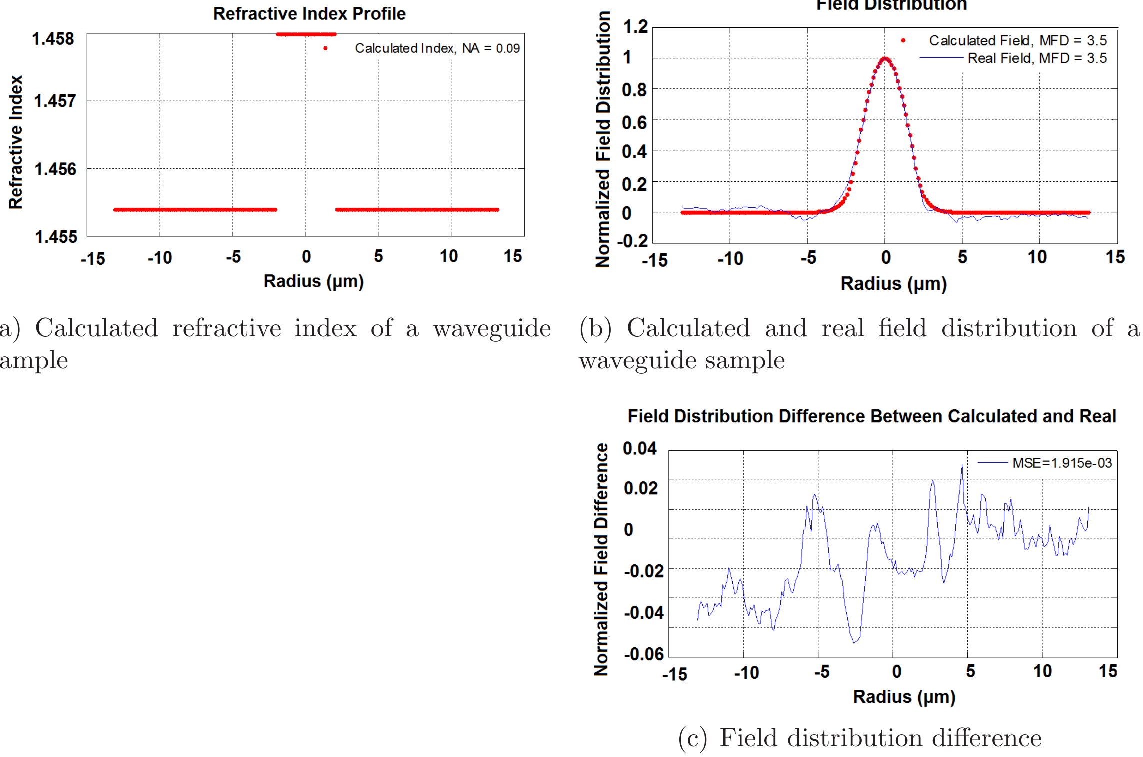

(a) Calculated refractive index of a waveguide sample

(b) Calculated and real field distribution of a waveguide sample

(c) Field distribution difference

Figure 4.11: Refractive-index calculation of a laser-written waveguide using the ESI method.

provide wavefront evolution (the distortion of the wavefront by the object) between image planes and can be post-processed to obtain a phase profile. This phase profile can then be converted into refractive-index profile.

The quantitative phase microscopy method I applied is on the basis of the transport of intensity equation (TIE) [62–64]. The basic idea is that the wavefront of light traveling through a transparent material is affected by its phase gradients. For a one-dimensional object (along the x-axis), the TIE can be derived from the paraxial wave equation, resulting in the following expression for the phase function $\phi(x)$ [65]:

$$\phi(x) = -\frac{2\pi n}{\lambda_0} \int (\frac{1}{I(x)} \int (\frac{dI(x)}{dz} dx)) dx \tag{4.11}$$

Here, n represents the refractive index of the sample, λ_0 is the light vacuum wavelength, and $I(x)$ denotes the intensity of the object along the x-axis. Furthermore,

$\frac{dI(x)}{dz}$ is the axial intensity gradient along the beam-propagation direction, which can be approximated by the difference of two slightly defocused images.

The optical path length (OPL) of the object can be calculated from the related phase $\phi(x)$:

$$OPL(x) = \phi(x) \cdot \frac{\lambda_0}{2\pi n} \tag{4.12}$$

Once OPL is known, the refractive-index change of the modified area, $\Delta n(x)$, can be calculated using the following equation:

$$\Delta n(x) = \frac{OPL(x)}{d} \tag{4.13}$$

where d is the thickness of the modified area in the material.

Equation (4.11) shows that the phase profile can be calculated from three images: one showing the intensity I(x) of the sample in focus, and two symmetrically defocused around the sample to estimate the axial intensity gradient $\frac{dI(x)}{dz}$. The experimental setup of the TIE measurement is displayed in Figure 4.12(a). This setup takes advantage of the existing DLW fabrication system (the left portion of Figure 3.14 in Chapter 3) and is easy to implement. The Köhler epi-illumination is set up using a 530 nm LED light, which is coupled through the same objective lens used for the fabrication by a dichroic mirror. The light is reflected through a 50/50 beam splitter and a tube lens, and imaged onto a CCD camera. The defocused images are recorded by translating the tube lens axially (with respect to the waveguide axis) by a small amount, Δz.

Figure 4.12(b) shows the OPL measurement of a waveguide fabricated in a glass block using the TIE method, together with the result using interferometry. For the interferometric measurement, the light source in Figure 4.12(a) is changed to a 640 nm diode laser and a Mach–Zender interferometer is installed between the tube lens and the CCD in order to introduce a shear to one arm [65]. The refractive-index

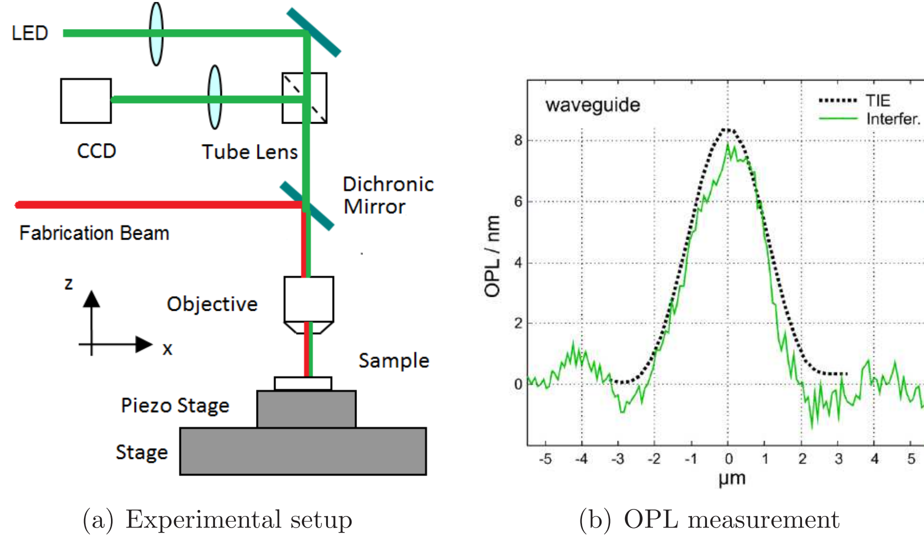

(a) Experimental setup (b) OPL measurement

Figure 4.12: (a) Experimental setup for measurement of accumulated OPL in the z-axis for embedded waveguides using quantitative phase microscopy (TIE). (b) Comparison of OPL measurements by interferometry and the TIE method for one DLW written waveguide in a fused silica glass.

profile $\Delta n(x)$ can be calculated from OPL using Equation (4.13). Figure 4.12(b) shows a good match between the TIE and interferometer results, indicating the TIE method is a valid metric for the refractive-index evaluation of waveguides.

Compared with the PMNFM, the TIE method has the advantage of taking the existing DLW fabrication setup and can estimate the refractive index of the written waveguides without moving. However, the TIE method is very sensitive to the illumination condition and normally contains 30% fluctuation in the result. Moreover, it is difficult to get an accurate value for the modified region, which is d in Equation (4.13). But it is a good indicator for simple refractive-index estimation during the DLW fabrication process.

4.7 Insertion and Propagation Loss

The insertion loss of an optical waveguide normally comprises three factors: the input and output coupling losses to and from the waveguide, and the propagation

loss along the waveguide. In order to obtain a better optical mode to couple into the fabricated waveguide, laser beam is first coupled into an optical fiber, whose output is then coupled into the waveguide. The optical fiber is directly butt-coupled to the waveguide end-facet to reduce device size and eliminate complicated alignment.

Limited by the equipment, destructive loss measurement such as cut-back method cannot be used in my case. The scattering light along propagation direction in the waveguide is recorded by a CCD camera, but the intensity resolution of the recorded image cannot provide sufficient accuracy for loss calculation. Therefore, a direct measurement method is applied. In order to estimate the insertion and propagation loss of the DLW written waveguide, the Thorlabs S121C photodiode is first tested for power measurement. Unfortunately, no power difference is observed between the input and output of the DLW written waveguide, both of which maintain an observed value of 0.1 μW (too small for the photodiode). Therefore, a CCD camera is used for power estimation in my case. The laser power is adjusted for the input and output measurement to avoid intensity saturation on the CCD camera, but the camera settings (brightness, shutter speed, gain, etc.) are maintained to keep the results comparable. After taking images of the near-field mode from the input and output of the waveguide, the intensity calculation algorithm is as follows:

1. Select the region of interest ROI in the image (red box in Figure 4.13, for example).
2. Calculate the average intensity values of the background (the area outside the red box).
3. Subtract the background value from the ROI.
4. Integrate the intensity value inside the ROI.
5. Normalize the integrated intensity of the input and output. Divide the inte-

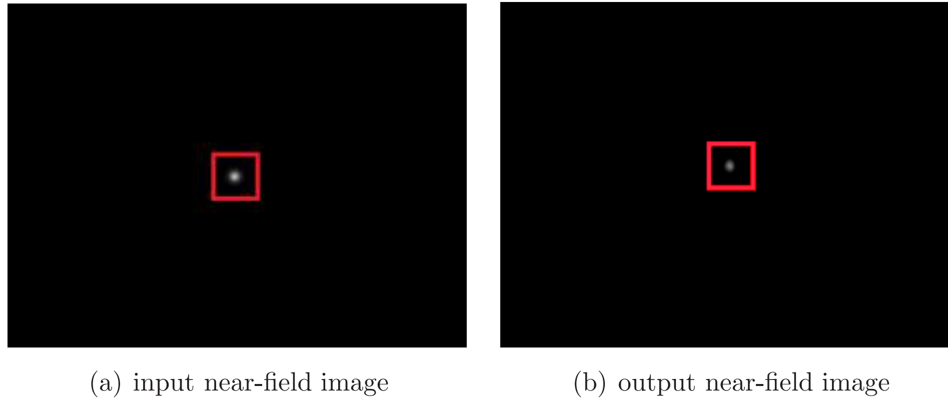

(a) input near-field image (b) output near-field image

Figure 4.13: CCD images of the waveguide input and output, and their selected ROI.

grated values by the corresponding laser power of the input and output measurements.

6. Divide the normalized integrated intensity values of the output intensity by that of input, thereby showing the coupling efficiency between the output and input.

For example, the near-field modes of the input and output are captured before and after the waveguide under test (Figure 4.13). The laser power is 1.5 μW and 3.1 μW. The original image has a dimension of 1,024 x 768 pixels. Now select a ROI of 50×50 pixels. By applying the above algorithm, the integrated intensity value of Figure 4.13(a) is 19,270 and Figure 4.13(b) is 11,334. Thus the normalized input intensity is 19,270/1.5= 12,847 and the normalized output intensity is 11,334/3.1=3,656, resulting in a coupling efficiency ratio of 3,656/12,847=28.5%.

Note that the measured insertion loss is significant; this is mainly attributed to butt-coupling into the waveguides with fiber. When coupling the light from the SM600 fiber-end into the waveguide, the average coupling efficiency is approximately 30% for a 10 mm single-mode waveguides (5.2 dB) using the described method and algorithm. There are a few major contributors to this loss:

1. Coupling misalignment: the stage (Figure 4.14 used for the free-space coupling is a 3-axes stage. It has only coarse adjustment, micrometer-accuracy in its control

of the coupling angle. The loss of the single-mode waveguide coupling is mainly due to this misalignment, as it is more sensitive to the angle than multimode. It is also noticed that the output mode is jittering, probably because of the unstable mechanical spring inside the stage. This all can result in high loss during coupling.

2. Mode mismatch loss: as it is described in Section 2.4.2 in Chapter 2, when light is coupled into waveguides, there are different dimensions between the input and output modes. The mode coupling loss is determined by the overlapping of the two modes.

3. Fresnel reflection loss: there is 4% reflection loss from the two reflection facets.

4. Loss on the waveguide edge: if the edge of the sample is not polished properly, the waveguide might not be perpendicular to the edge, or the waveguide end might not be close enough to the edge, etc.

5. The propagation loss of the DLW waveguide.

Theoretically, the coupling efficiency, η, between the fiber and waveguide can be calculated using the overlap integral as follows:

$$\eta = \frac{[\int\int E_f(x,y)E_w^*(x,y)dxdy]^2}{[\int\int E_f(x,y)E_f^*(x,y)dxdy]^2][\int\int E_w(x,y)E_w^*(x,y)dxdy]^2]} \quad (4.14)$$

where the integrals are taken over all space. $E_f(x,y)$ and $E_w(x,y)$ are the electric field of the fiber and waveguide, $E^*(x,y)$ represents complex conjugate.

A Matlab program is developed to calculate the coupling efficiency using Equation (4.14). For a fiber mode and a waveguide mode displayed in Figure 4.15, the calculated η is 92.4%.

Limited by the quality of the equipment in the lab, especially the stages, there is also large loss caused by coupling misalignment. Most of the 5.2 dB insertion loss

Figure 4.14: Experimental setup for the waveguide coupling.

cannot be attributed to propagation loss of the waveguide. For comparison, when a piece of 10 mm SM600 fiber is cut and placed for testing instead of the waveguide, an insertion loss of 4.6 dB is observed. As the propagation loss of 10 mm SM600 is negligible, 4.6 dB can be used as a reference of the system insertion loss (exclude the propagation loss). By comparing with the SM600 result, the actual propagation loss of the waveguide is estimated to be approximately 0.6 dB/cm.

4.8 Conclusion

The improved PMNFM proposed in this chapter allows a better accuracy in predicting the transmission characteristics of optical waveguides. Because of the high sensitivity to the noise in the experimental data, data post-processing should be applied using the Savitzky–Golay filter and curve-fitting technique. In addition, to simplify the prediction of propagation properties, the ESI profile is calculated to obtain a better understanding of the written waveguide, as the characteristics of step-index fiber are

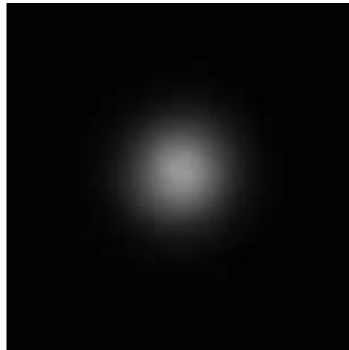

(a) fiber mode

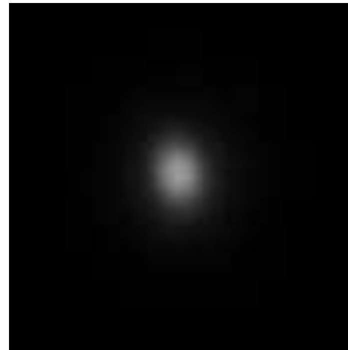

(b) waveguide mode

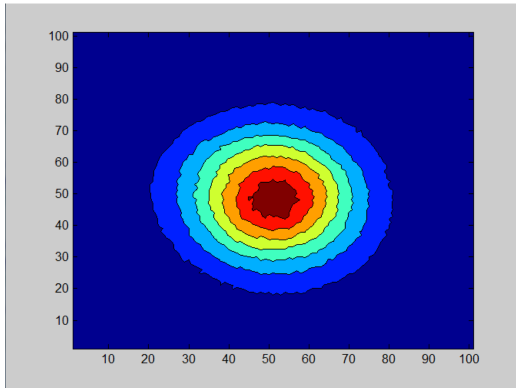

(c) fiber mode profile

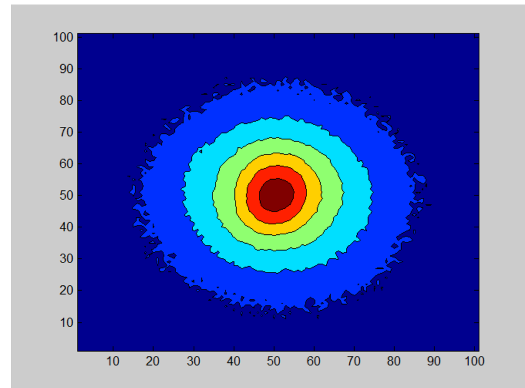

(d) waveguide mode profile

Figure 4.15: Calculation of mode-coupling efficiency. (a) fiber mode; (b) waveguide mode; (c) extracted fiber mode profile in Matlab; (d) extracted waveguide mode profile in Matlab.

well-known. The calculated results from the experimental data on the SM600 single-mode fiber and a DLW waveguide, with both the improved PMNFM and the ESI method, are close to expectation with small errors. This indicates good accuracy of the proposed methods.

For simply estimation, quantitative phase measurement via the TIE method is also applied to understand the refractive-index profile during fabrication by taking advantage of the existing DLW system. Measurement of the insertion and propagation loss is important for waveguide characterisation as well. Limited by the lab equipment, an accurate loss measurement cannot be obtained. The propagation loss of the DLW written waveguide can only be estimated by comparison with the known commercial single-mode fiber. Our group are now updating and improving the experimental equipment in the lab by using much higher quality stages and photodiode for better measurement. In general, the PMNFM and TIE method discussed in this chapter have provided sufficient information about the refractive-index profile of the DLW waveguide for the system, whereas the quality of the waveguide can be measured by a good estimation of the propagation loss in comparison with the known commercial fiber.

Chapter 5

Fabrication of Optical Waveguides in Fused Silica

Optical waveguides inside pure silica glasses are demonstrated and discussed in this chapter. Following the investigation of adaptive aberration correction in the direct laser writing (DLW) system, waveguides fabricated at various depths (up to 1.2 mm) are investigated and analysed. Based on the characteristics analysis of the written waveguides, fabrication parameters are carefully adjusted to obtain higher-quality components. It is demonstrated that the quality of the focal spot in ultrafast DLW fabrication is improved dramatically by applying the aberration correction, especially when deep into the sample. The potential of the DLW technique with adaptive optics for three-dimensional (3D) photonic structures is shown by the demonstration of y-splitters in fused-silica. A y-splitter is modelled using commercial BPM-CAD software and its bend losses are estimated by another commercial program called FIMMWAVE. The dimensions of the splitter are carefully designed and the propagation characteristics of the y-splitter is simulated. Y-splitters with different writing structures are then fabricated and characterised. Finally, the design and fabrication of parallel and multi-spot writing are briefly discussed. The results and fabrication

details of the aberration-corrected waveguide at different depths has been discussed and published in [66].

5.1 Introduction

The investigation of the DLW technique was first explored in silica glasses [1, 4] because of their excellent properties and importance in optical applications. However, depth-dependent aberrations have been a big concern for the DLW technique in the past decades, which greatly limits the capability of 3D fabrication at greater depths.

A very low NA objective is normally used to solve this problem but the spatial resolution is sacrificed. In addition, as discussed in Chapter 3, lower NA leads to a highly asymmetric cross-section for transverse laser writing. Here, waveguides fabricated by the DLW with aberration correction using a SLM are demonstrated deep inside fused silica. Properties of the waveguides written with and without aberration correction are studied and compared. Homogenous single-mode waveguides in a transverse geometry with circular cross-sections are obtained with the proposed technique. Depth-dependent aberrations are significantly reduced or eliminated, enabling the writing of optimal waveguides deep below the surface. Experimental results reveal that high quality single-mode waveguides can be produced over a significant depth range (>1 mm), while maintaining the accuracy of the fabrication position. This facilitates the fabrication of more complex three-dimensional (3D) waveguides, and adds greater control over the shaping and quality of the focal spot during the DLW process.

5.2 Waveguide Fabrication at Various Depths

Aberration may be induced by many different factors, one of which is the refractive-index mismatch between the processed material and the objective immersion medium.

The refractive-index mismatch aberration is depth-dependent and comes from an optical path length (OPL) difference between beams enter the interface at different angles (θ_1 and θ_2 in Figure 5.1). As each angle has different phase delays, the phase aberration ϕ induced by the air-dielectric (with a refractive index of n) interface can be written as follows:

$$\phi = \frac{2\pi d_{nom}}{\lambda_0}(n \cos\theta_2 - \cos\theta_1) \tag{5.1}$$

where λ_0 is the laser vacuum wavelength, d_{nom} is the nominal depth focusing within the sample, and θ_1 and θ_2 are the angles of convergence.

If the NA of the objective is known, Equation 5.1 can be converted to:

$$\phi(r) = \frac{2\pi d_{nom}}{\lambda_0}\left(\sqrt{(n^2 - (NAr)^2} - \sqrt{1 - (NAr)^2}\right) \tag{5.2}$$

where r is the normalised pupil radius.

The phase aberration can be compensated by applying the conjugate of the refractive-index mismatch aberration function $\phi_R(r)$ to the SLM:

$$\phi_R(r) = -\frac{2\pi d_{nom}}{\lambda_0}\left(\sqrt{(n^2 - (NAr)^2} - \sqrt{1 - (NAr)^2}\right) \tag{5.3}$$

The phase aberration can be divided into two portions: the spherical aberration (SA) and the defocus. Following the notation used by Cumming et al. [67], if we define s as the defocus factor, it links d_{nom} and d_{act} via the relation $d_{nom} = sd_{act}$. The spherical defocus function can be written as follows:

$$D_n(r) = \frac{2\pi \Delta d}{\lambda_0}\sqrt{(n^2 - (NAr)^2} = \frac{2\pi d_{nom}(1-s)}{s\lambda_0}\sqrt{(n^2 - (NAr)^2} \tag{5.4}$$

Here $\Delta d = \frac{d_{nom}(1-s)}{s} = d_{act} - d_{nom}$ is the distance that the focus is shifted, as shown in Figure 5.1. The offset in the fabrication depth Δd leads to unpredictable waveguide positions, and may cause problems when light is coupled into the top and bottom

waveguides at the same time. This extended depth of field also results in a highly asymmetric cross-section with multimode operation at large depths.

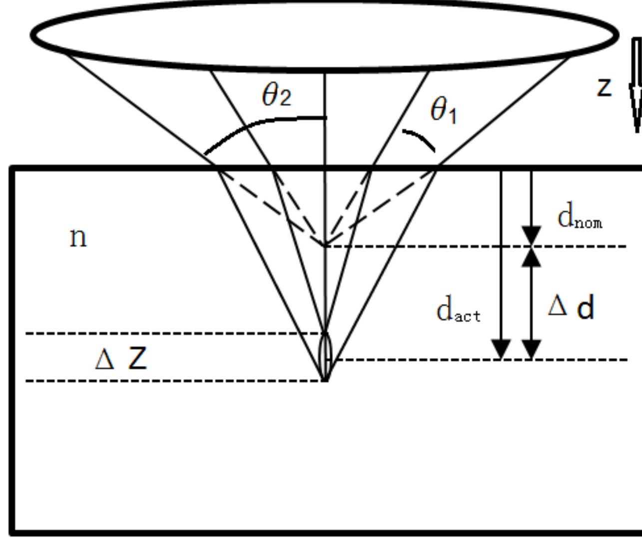

Figure 5.1: Schematic of the aberration generated during laser fabrication.

If the defocus function $D_n(r)$ is subtracted from the conjugated function $\phi_R(r)$, the defocus-free spherical aberration compensation, $\phi'_R(r)$, can be written as

$$\phi'_R(r) = \phi_R(r) - D_n(r) = \frac{2\pi d_{nom}}{s\lambda_0}\left(s\sqrt{1-(NAr)^2} - \sqrt{(n^2-(NAr)^2}\right) \tag{5.5}$$

The required stage position can be found by moving Δd, and the defocus-free SA can be corrected separately. The optimal value of s corresponds to the condition when the phase magnitude at the centre and edge of the pupil are equal, i.e. when $\phi'_R(1) = \phi'_R(0)$. To meet this condition, s should be equal to

$$s = \frac{n - \sqrt{n^2 - NA^2}}{1 - \sqrt{1 - NA^2}} \tag{5.6}$$

The relationship between $1/s(d_{act}/d_{nom})$ and NA is displayed in Figure 5.2. Obviously, the ratio of d_{act}/d_{nom} increases with NA. However, $1/s$ changes slowly at NAs lower than 0.6 and starts to increase dramatically at higher NAs. For fused silica

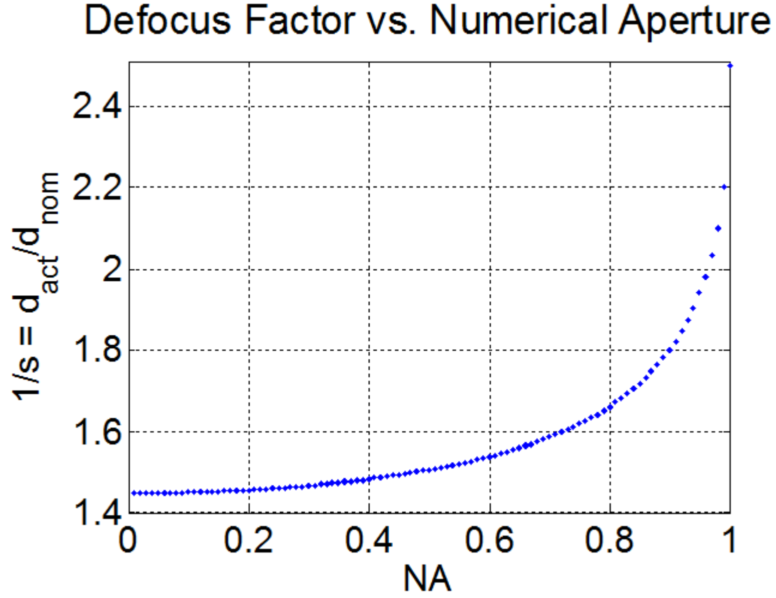

Figure 5.2: Relationship between the defocus factor (1/s) and the numerical aperture (NA) of the objective lens.

($n = 1.45$), $1/s = 1.51$ at $NA = 0.5$ and $1/s = 1.94$ at $NA = 0.95$.

During DLW fabrication, the phase pattern shown in Figure 5.3(a) is first applied on the spatial light modulator (SLM). It comprises three main components: the blazed grating, slit and background phase pattern. The blazed grating is used to diffract the maximum light to the first order, which reduces the interference with the other unmodulated light from the SLM. The slit is used to obtain a more symmetric waveguide cross-section, as discussed in Section 3.2 in Chapter 3. The background phase pattern is used to correct the initial flatness of the SLM and the system aberration. As discussed in Chapter 3, the plasma emission sensing technique is then applied to obtain the correction phase pattern for depth-dependent aberration at each depth. All components add up to a final phase pattern (at a depth of 650 μm for example), as shown in Figure 5.3(b).

Optical properties of the waveguides at different depths are related to their depth-dependent aberration. Compared with other DLW systems, our DLW system with adaptive optics has the advantage of accurate aberration correction at various depths,

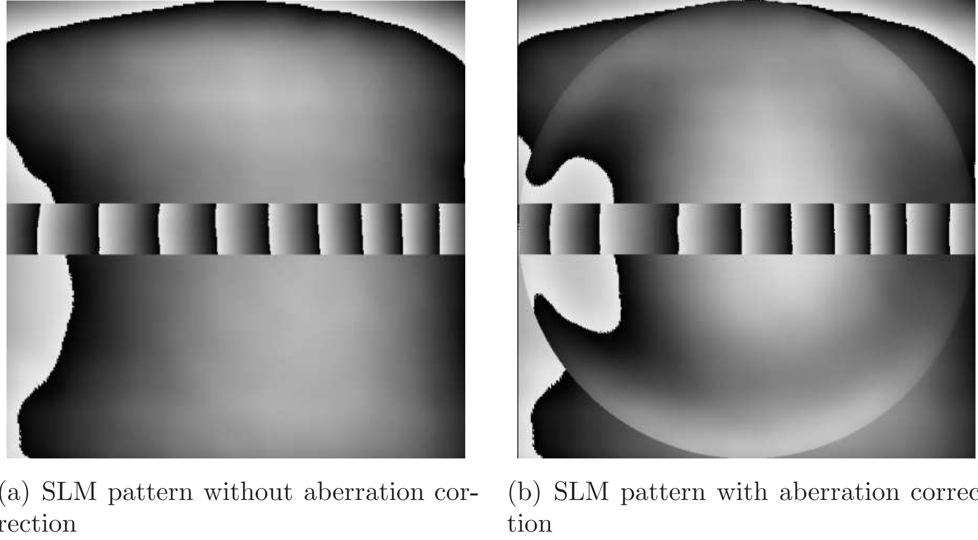

(a) SLM pattern without aberration correction

(b) SLM pattern with aberration correction

Figure 5.3: SLM phase pattern for waveguide fabrication: (a) phase pattern as blazed grating and slit without aberration correction; (b) phase pattern with aberration correction at 650 μm depth (defocus of +400 μm, +0.25 for mode 5, -0.5 for mode 6 and mode 8, +0.5 for mode 7, -0.25 for mode 11, mode 22 and mode 37).

thereby greatly improving the quality of the focal spots.

Fabrication parameters should also be carefully adjusted during DLW process. Different pulse energies (measured at the back aperture of the objective) and writing speeds are tested to obtain the optimal parameters for DLW fabrication. For example, combinations of parameters in Table 5.1 are tested for the DLW system at a depth of 0.2 mm. The fabricated waveguides are shown in Figure 5.4. Obviously, waveguide D has the optimal performance, resulting in sufficient refractive-index modification without cracking. At a pulse energy of 3.8 μJ, waveguide A and B can create some small refractive-index changes. At a pulse of of 4.1 μJ, waveguide C has non-uniform modification when the speed is too fast (50 μm/s). When the pulse energy is too high (> 4.3 μJ), severe damage occurs in the substrate during DLW fabrication resulting in cracking (waveguide E and F).

Figure 5.5 shows waveguides fabricated at various depths of 0.2, 0.5, 0.8, 1.0 and 1.2 mm into a fused silica sample, at a speed of 0.25 mm/s, with slit beam-shaping. During fabrication, the power of the laser should also be carefully chosen by

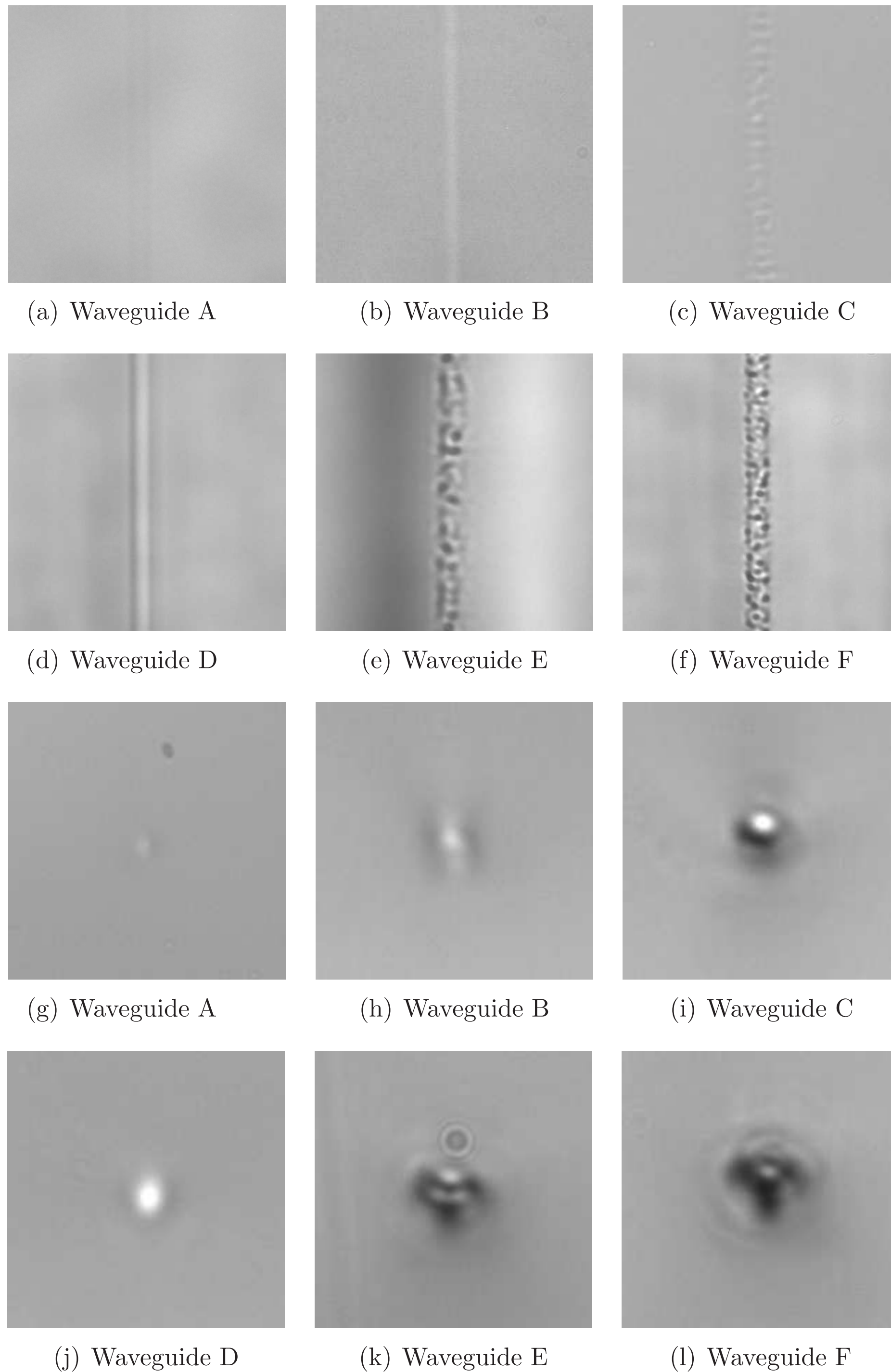

Figure 5.4: Waveguide fabricated at 0.2 mm with different pulse energy and writing speed as listed in Table 5.1. (a)-(d) top-down view of the fabricated waveguides under transmission microscope (with slight defocus); (e)-(h) cross-sectional view of the fabricated waveguides under transmission microscope (with slight defocus).

Waveguide	Pulse Energy (μJ)	Speed (μm/s)
A	3.8	50
B	3.8	25
C	4.1	50
D	4.1	25
E	4.3	50
F	4.3	25

Table 5.1: Fabricated waveguides with different pulse energies and writing speeds.

rotating the angle of the half-wave plate at the laser output. Without the aberration correction, particularly at higher depths, the focal spot can be highly aberrated, resulting in non-circular and non-homogenous waveguides with larger cross-section.

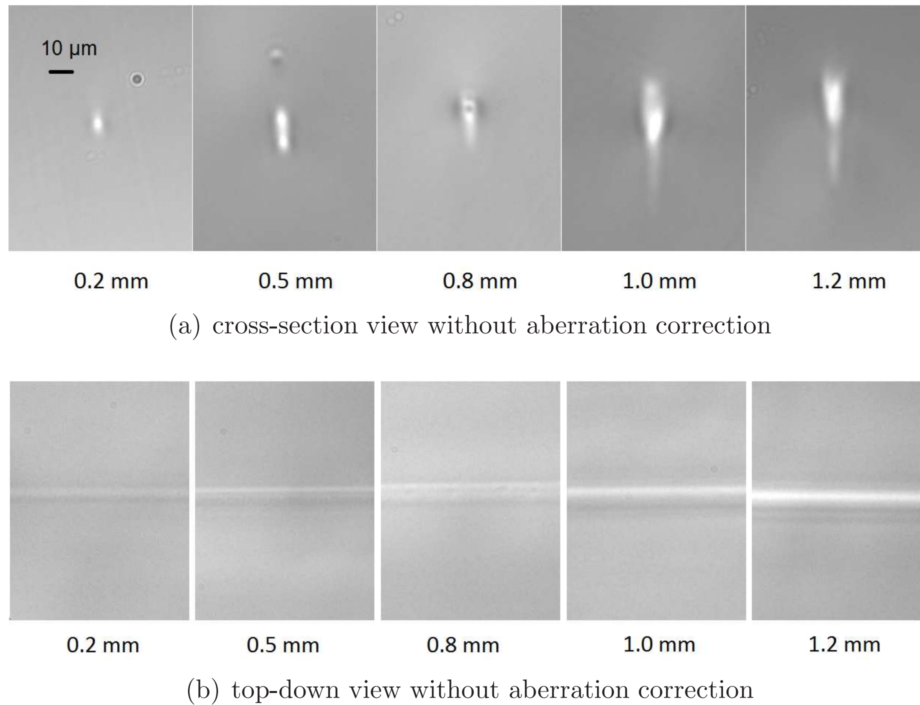

(a) cross-section view without aberration correction

(b) top-down view without aberration correction

Figure 5.5: Microscope images of waveguides fabricated at different depths without aberration correction.

Conversely, when an aberration correction is applied (Figure 5.6), circular and homogenous waveguides can be created in the focal region at different depths. The

cross-sections of the waveguides maintain a similar profile, even deep into the surface.

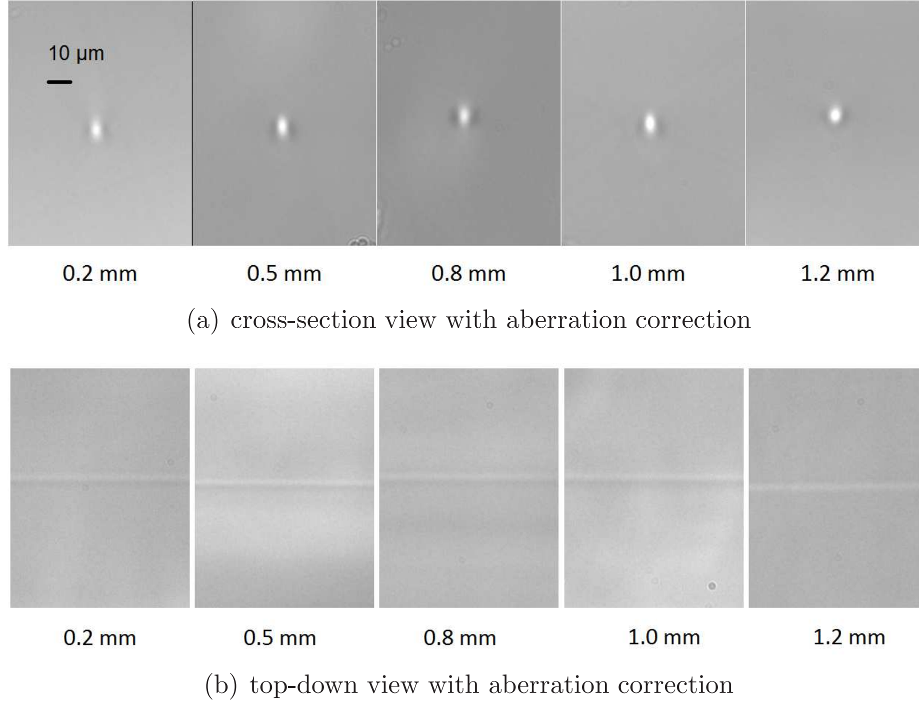

(a) cross-section view with aberration correction

(b) top-down view with aberration correction

Figure 5.6: Microscope images of waveguides fabricated at different depths with aberration correction.

Note that more pulse energy is required for refractive-index modification at larger depths. As shown in Table 5.2, the pulse energy increases dramatically from 4.9 μJ (at a depth of 0.2 mm) to 9.9 μJ (at a depth of 1.2 mm), if no aberration correction is applied. There is much less increase (3.9 μJ to 5.8 μJ) over the same depth range with aberration correction. The high pulse energy requirement is mainly caused by the depth-dependent abberation, which highly extends the dimensions of the writing focus.

The aberration correction can also help to precisely situate the waveguide position inside the sample. Figure 5.7(b) shows that, at the depth of 1.2 mm, the uncorrected waveguides are highly elongated and off from the original set position, whereas the corrected ones are circular and precisely located (Figure 5.7(a)).

Waveguides written without aberration correction change to multimode waveg-

Depth Below Surface (mm)	Required Pulse energy without aberration correction (μJ)	Required Pulse energy with aberration correction (μJ)
0.2	4.9	3.9
0.5	5.2	4.1
0.8	7.0	4.5
1.0	8.5	5.0
1.2	9.9	5.8

Table 5.2: Pulse energy requirement at different depths with and without aberration correction.

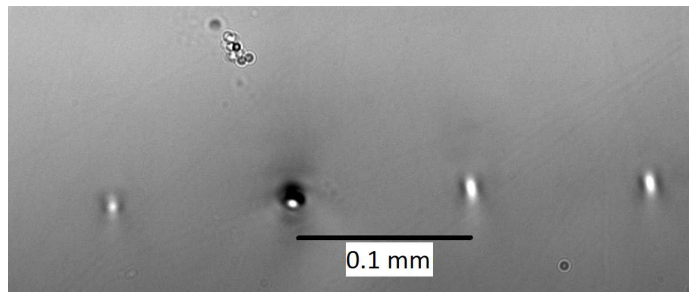

(a) cross-section of waveguides at the depth of 0.1 mm

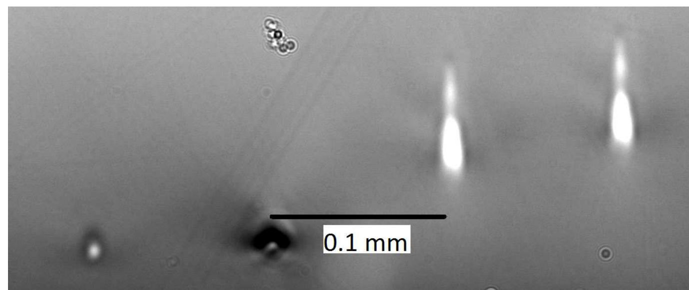

(b) cross-section of waveguides at the depth of 1.2 mm

Figure 5.7: The position offsets of the waveguides fabricated at the depth of 0.1 mm and 1.2 mm, under the transmission microscope (with slight defocus). The right two waveguides in both images are aberration corrected, while the left ones are not.

uides at greater depths. Conversely, waveguides fabricated with aberration correction continue to transmit single mode (Figure 5.8(a)) with well-confined circular cross-sections. Waveguides fabricated at different depths (0.2, 0.5, 0.8, 1.0 and 1.2 mm) with corrected aberrations are shown in Figure 5.8(b). It can be seen that the waveguide fabricated at a depth of 1.2 mm has similar quality as the ones at lower depth of 0.2 mm, while maintaining single mode. This indicates that focal spots are well aberration-corrected during the DLW fabrication.

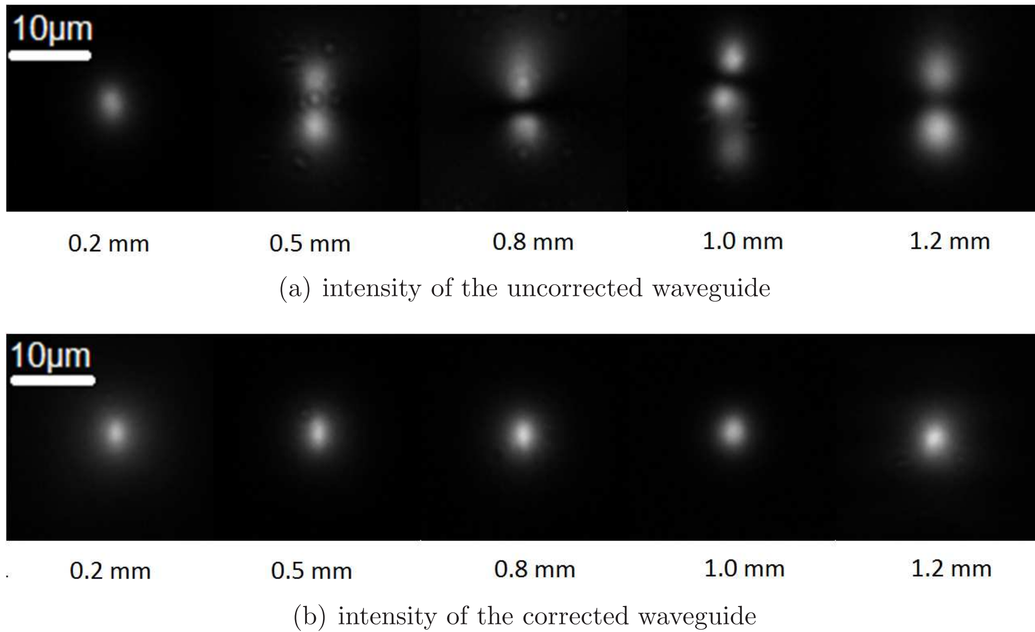

(a) intensity of the uncorrected waveguide

(b) intensity of the corrected waveguide

Figure 5.8: The near-field intensity distributions at the end of fabricated waveguides for a wavelength of 630 nm.

For an aberration-corrected waveguide fabricated at a depth of 0.8 mm, a total loss of 5 dB at 630 nm over 10 mm is measured. As discussed in Chapter 4, significant losses are mainly attributed to butt-coupling into the waveguides with fiber. Take the insertion loss of the commercial fiber SM600 as a reference, the actual estimated propagation loss of the written waveguide is approximately 0.5 dB/cm. By using the quantitative phase microscopy during fabrication, as proposed in [65], the maximum refractive-index increase at the center of this waveguide is approximately 4.5×10^{-3}. Light at a wavelength of 630 nm is coupled into the waveguide and the intensity

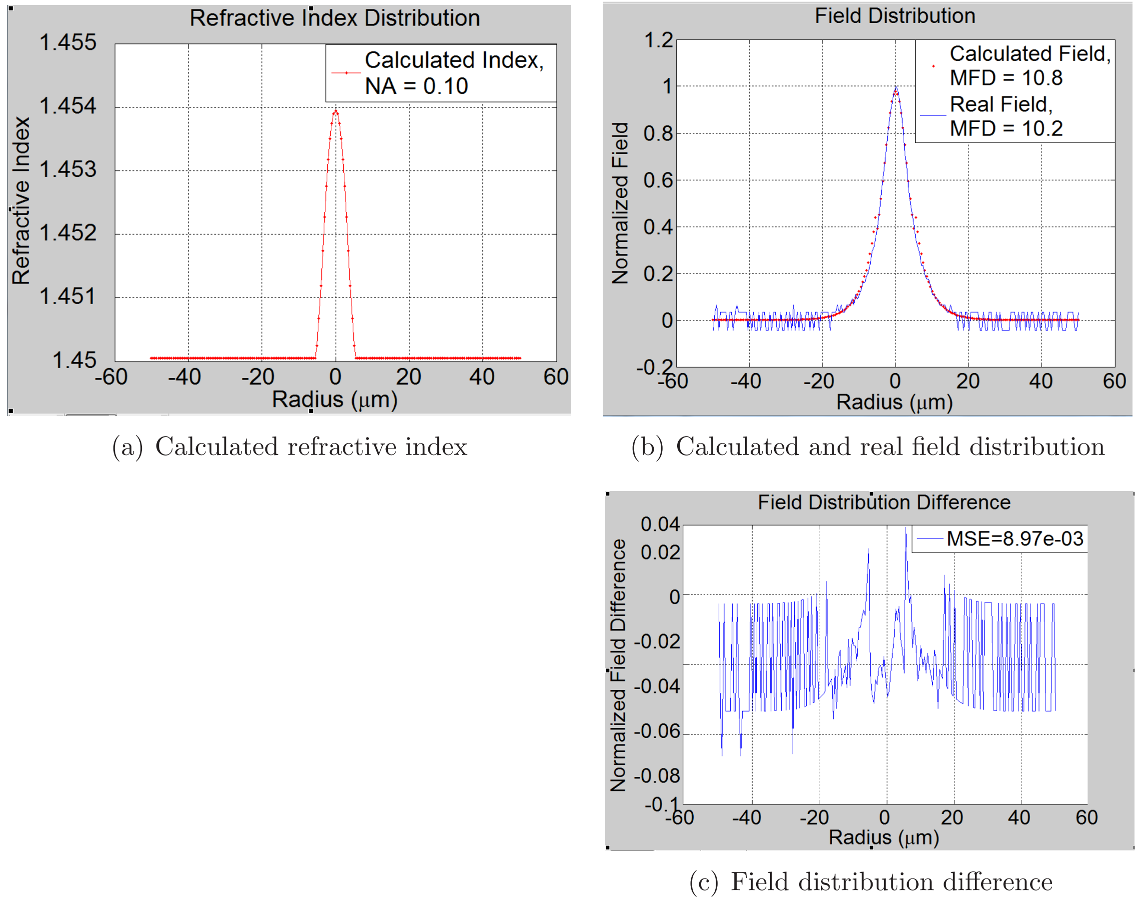

(a) Calculated refractive index

(b) Calculated and real field distribution

(c) Field distribution difference

Figure 5.9: Refractive-index calculation of an aberration-corrected waveguide at a depth of 0.8 mm using the PMNFM.

distribution at the end facet of the waveguide is imaged onto a charge-coupled device (CCD) camera. Analysis of this image using the improved propagation-mode near-field method (PMNFM) is shown in Figure 5.9. The calculated refractive-index profile is displayed in Figure 5.9(a), with a refractive-index difference of approximately 3.8×10^{-3} at its peak.

5.3 Design and Fabrication of Y-splitters

To demonstrate the capacity of DLW for optical devices, y-splitters with different dimensions and parameters are modelled and fabricated. With adaptive optics, the fabricated y-splitters have more symmetric and circular profiles compared with pre-

vious demonstrations.

5.3.1 Bend Losses

Before the design of y-splitters, it is essential to understand the relationship between the bend losses and bend radii. Traditionally, the most commonly used bend loss model is developed by Marcuse in [68]. In general, the radiation loss caused by the curved waveguide can be obtained by calculating the amount of output power ΔP per unit length of the waveguide and from the loss formula:

$$2\alpha = \frac{\Delta P}{P} \tag{5.7}$$

where P is power carried in the straight guide and α is the amplitude-loss coefficient of the guided wave. Here, 2α is used to represent the power-loss coefficient.

From [68], 2α can be presented as follows for a weakly guiding fundamental mode:

$$2\alpha = \frac{\sqrt{\pi}\kappa^2 exp[-\frac{2}{3}(\gamma^3/\beta_g^2)R]}{2\gamma^{3/2}V^2\sqrt{R}(\ln\gamma a)^2} \tag{5.8}$$

Here, β_g is the propagation constant in the straight guide and can be calculated from the eigenvalue equation of the guided modes. R is the radius of curvature of the bent waveguide, core-cladding interface is at $r = a$, and

$$\gamma = \sqrt{\beta_g^2 - n_0^2 k_0^2}$$
$$\kappa = \sqrt{n_1^2 k_0^2 - \beta_g^2}$$
$$V = \sqrt{\kappa^2 + \gamma^2} = k_0 a \sqrt{n_1^2 - n_0^2}$$

where n_0 is the refractive index of the cladding, n_1 is the refractive index of the core, and k_0 is the wavenumber in vacuum.

For a single-mode weakly-guiding waveguide, with known wavelength λ_0, Δn and a, the relationship between the bend radius and the loss can be estimated using

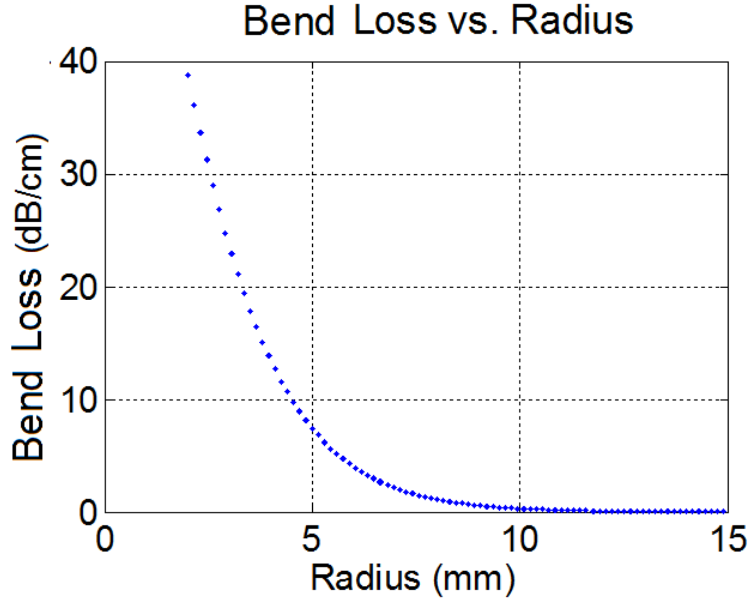

Figure 5.10: The relationship between the bend radius (mm) and the loss (dB/cm) using the Mercue's modelling. λ_0=600 nm, $\Delta n = 2 \times 10^{-3}$ and a=3 μm.

Equation (5.8). Figure 5.10 shows an example when λ_0=600 nm, $\Delta n = 2 \times 10^{-3}$ and a=3 μm. The waveguide loss is expressed in dB per centimeter (dB/cm) and is plotted against bend radius in mm. The "safe" bend radius (when the loss is negligible) is $R \gg 10mm$.

Equation (5.8) can only be used for estimation of weekly guiding, step-index single-mode waveguides. For complicated structures with other refractive-index profiles, other tools are needed. In my case, FIMMWAVE version 6, a commercial software that uses the bend waveguide module and a finite difference method (FDM) complex solving engine, is applied for calculation of accurate bend losses. If the same parameters (λ_0, Δn and a) are used as in Figure 5.10, similar simulation result is obtained by FIMMWAVE (Figure 5.11).

For circularly symmetric waveguides with a cladding refractive index of 1.45 and a quadratic variation of the index assumed across the fiber core, the simulation results are shown in Figure 5.12 and Figure 5.13. In Figure 5.12(a), when the numerical aperture (NA) is 0.1 ($\Delta n = 0.0034$), at a wavelength of 800 nm and a core radius

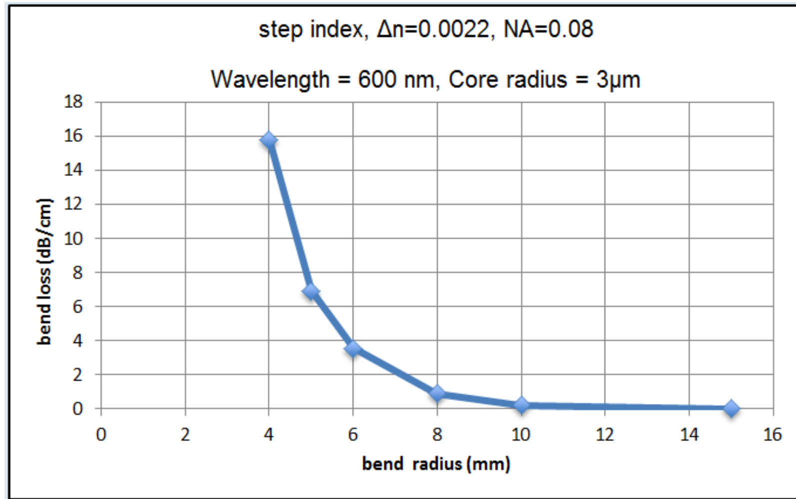

Figure 5.11: The relationship between the bend radius (mm) and the loss (dB/cm) using FIMMWAVE. λ_0=600 nm, $\Delta n = 2 \times 10^{-3}$ and a=3 μm.

of 4 μm, the "safe" bend radius (when the loss is negligible) is approximately 50 mm. With everything else held constant, if NA is reduced to 0.08 from 0.1 (value in Figure 5.12(a)), the "safe" bend radius will increase to approximately 250 mm (Figure 5.12(b)).

For a different wavelength of 600 nm and a core radius of 3 μm, when NA is 0.1, the "safe" bend radius is approximately 30–40 mm (Figure 5.13(a)). Reducing the NA to 0.08 increases the "safe" bend radius for a quadratic fiber back to approximately 150 mm, or even several thousand mm when $NA = 0.06$.

It can be seen from the simulation results that bend losses are more sensitive to NA than the wavelength. Based on the refractive-index measured using the PMNFM in Figure 5.9, the NA is 0.1 at a wavelength of 630 nm, with a core radius of 3.5 μm, the bend loss is negligible when $R \gg 100$ mm. Bend loss calculations are notoriously difficult and more work is probably needed to check their reliability. However, the simulation results can be used as references for the fabrication of bend waveguides, especially for the design of y-splitters.

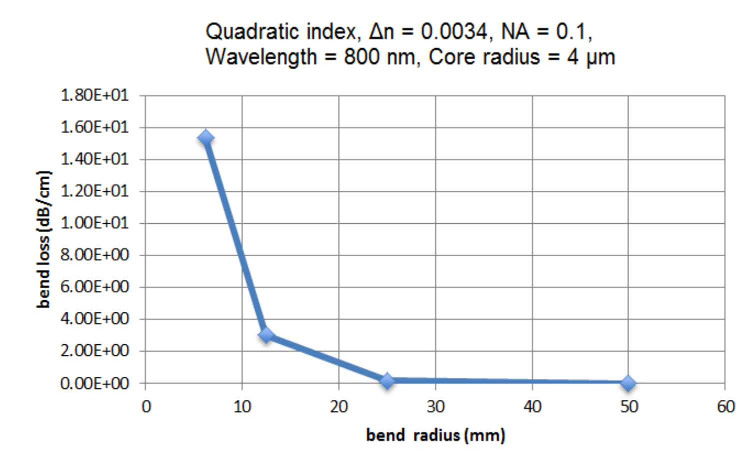

(a)

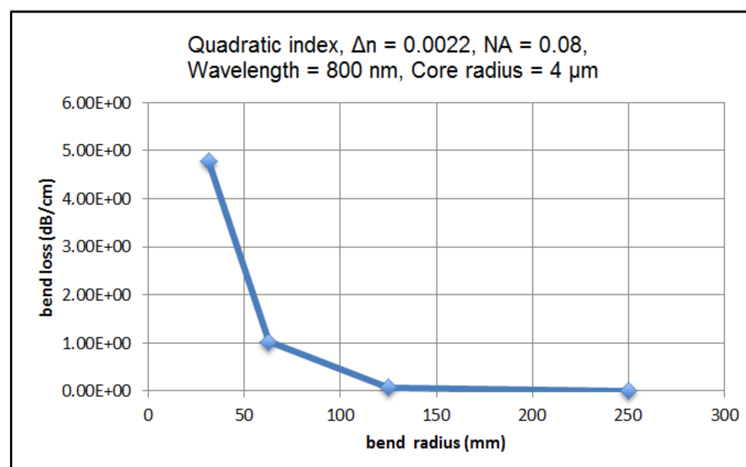

(b)

Figure 5.12: Simulation results between the bend loss and the radius of the waveguide at a wavelength of 800 nm.

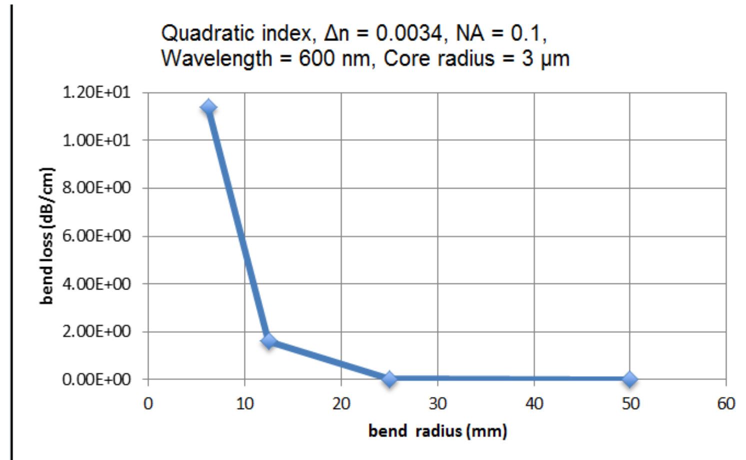

(a)

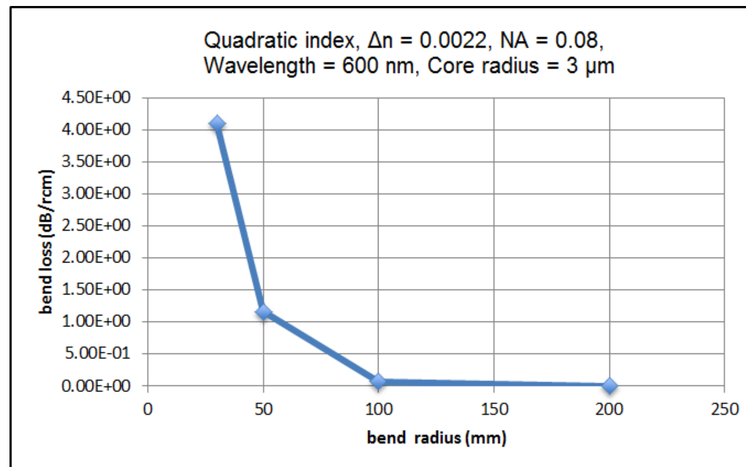

(b)

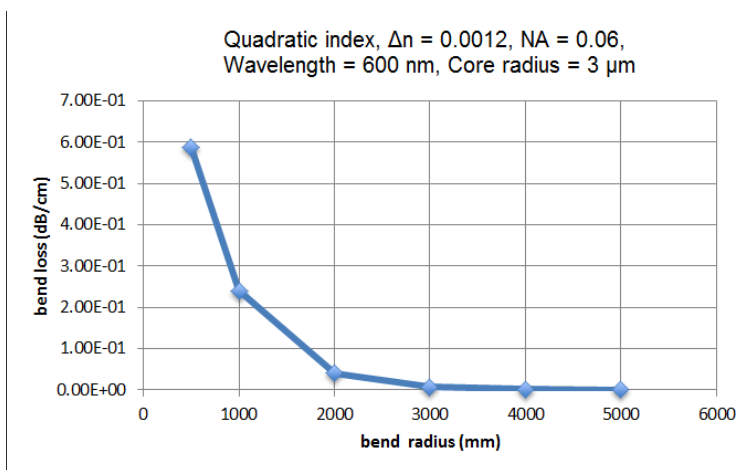

(c)

Figure 5.13: Simulation results between the bend loss and the radius of the waveguide at a wavelength of 600 nm.

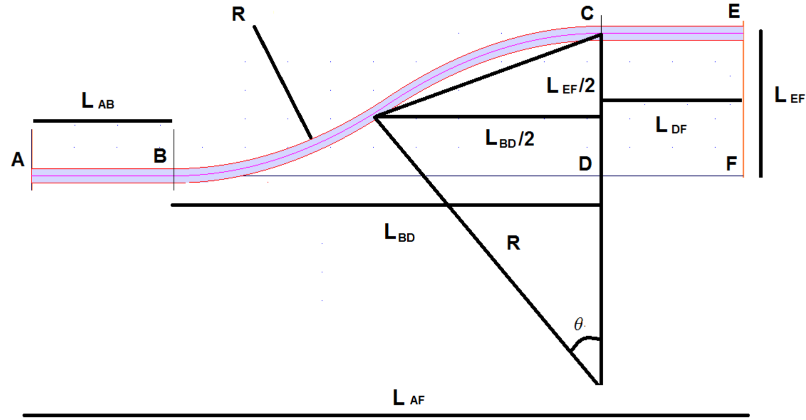

Figure 5.14: Bend radius calculation of a bend waveguide.

5.3.2 Modelling of Y-splitters

A y-splitter has two arms, both including straight and curved regions. As shown in Figure 5.14, the curved S-bend region comprises two identical arcs with a radius of R.

If the total length of the curved region is L_{BD} and the offset of the arm is L_{EF}, the bend radius can be calculated as follows:

$$R = \frac{(L_{BD}/2)^2 + (L_{EF}/2)^2}{L_{EF}} \tag{5.9}$$

The curved region has a total curved length L_{BC} of:

$$L_{BC} = 2R \cdot \arcsin \frac{L_{BD}/2}{R} \tag{5.10}$$

With the refractive-index information of the written waveguide using the algorithm discussed in Chapter 4, y-splitters can be modelled using BPM-CAD, a software package used for waveguide modelling of a variety of integrated and fiber optics. The beam propagation method (BPM) is used in the software to simulate the propagation of light through any waveguide. Different lengths and separations are tested and simulated. One example is shown in Figure 5.15. The total length of the splitter

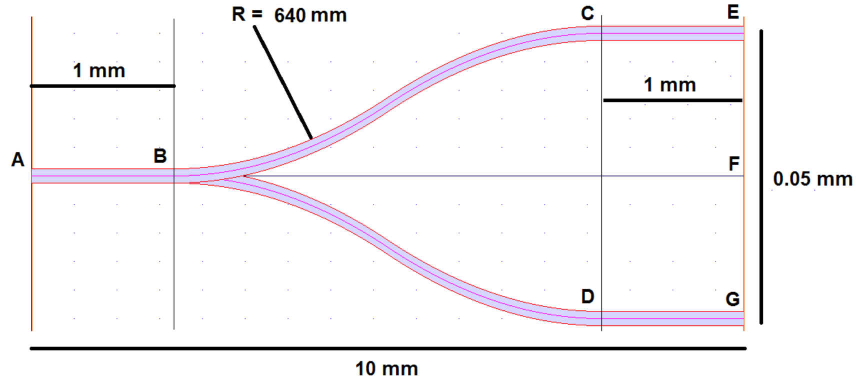

Figure 5.15: Design of a y-splitter in a fused silica glass sample.

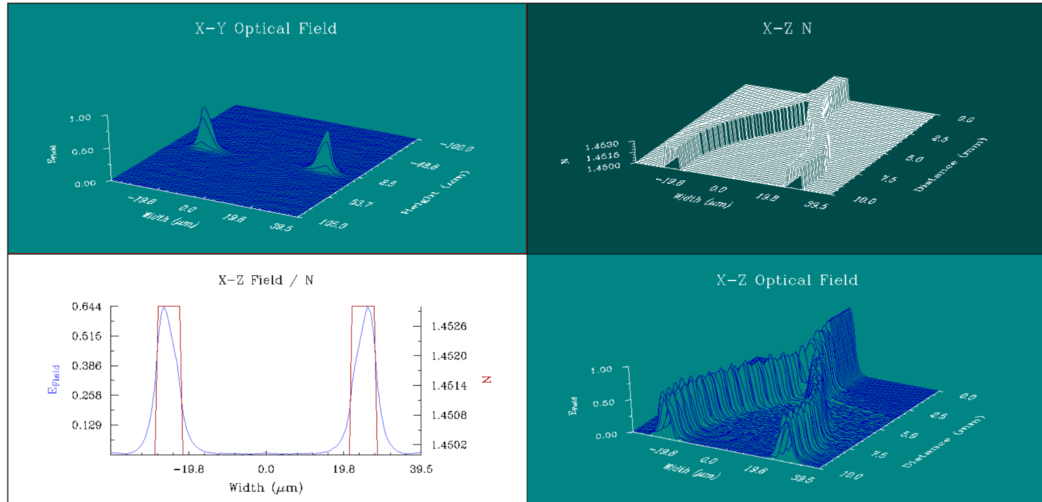

Figure 5.16: BPM-CAD simulation results of a y-splitter.

is 10 mm with a 0.05 mm separation. The refractive index of the substrate is 1.45 with a step-index difference of 3×10^{-3} for the waveguide. The width and height of the waveguide are 6 μ m each. The simulation results are shown in Figure 5.16. The wavelength is set to 600 nm, the excitation field is Gaussian and non-polarisation is assumed.

5.3.3 Fabrication of Y-splitters

A simple y-splitter is fabricated on the basis of above modelling at a pulse energy of 4.1 μJ and a speed of 25 μm/s. Y-splitters with different dimensions are fabricated

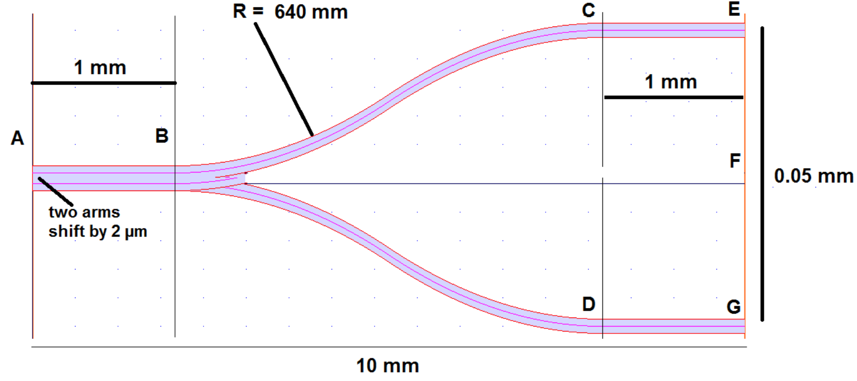

Figure 5.17: Shift of two arms in a y-splitter in a fused silica glass sample.

and tested. Figure 5.15 is one example of the written y-splitters with a total length of 10 mm (L_{AF}) and a separation distance of 0.05 mm (L_{EG}). The straight portion before (L_{AB}) and after (L_{CE} and L_{DG}) splitting are both 1 mm. The splitting junction is composed by two arc S-bends, whose radius can be calculated by Equation 5.9. The calculated bend radius is approximately 640 mm, much larger than the "safe" bend radius obtained from simulations in previous section. Therefore, the bend losses of the designed y-splitter are negligible.

During the fabrication, if the upper arm and lower arm of the y-splitter are fabricated, the straight portion before splitting (L_{AB}) is double-scanned. To avoid severe damage or crack of this region, the upper arm and lower arm can be written with inter-scan shifts. In our case, an inter-scan shift of 2 μm is applied, as shown in Figure 5.17. This provides more uniformity over the front region (L_{AB}) and higher refractive-index modifications.

A y-splitter fabricated at a pulse energy of 3.9 μJ and a speed of 25 μm/s is shown in Figure 5.18. The output optical modes of two y-splitters, with (y-splitter1) and without (y-splitter2) inter-scan shift, are shown in Figure 5.19 and Figure 5.20. For y-splitter1, the estimated splitting ratio is 45/55 and the total insertion loss of 8.7 dB, including splitting loss (3 dB) and fiber butt-coupling loss. As discussed in Chapter 4, significant losses are mainly attributed to butt-coupling into the waveguides with

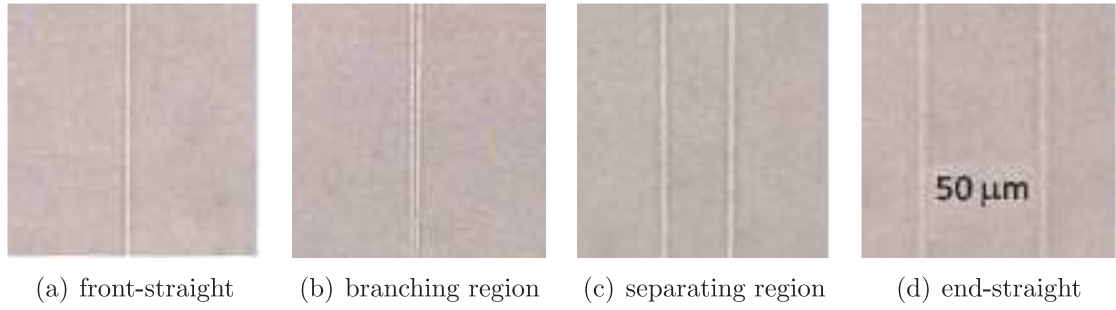

(a) front-straight (b) branching region (c) separating region (d) end-straight

Figure 5.18: A y-splitter with DLW under the microscope in a fused silica glass sample. (a) front-straight region (AB); (b) branching region (B); (c) separating region (BC); (d) end-straight region (CE, DG).

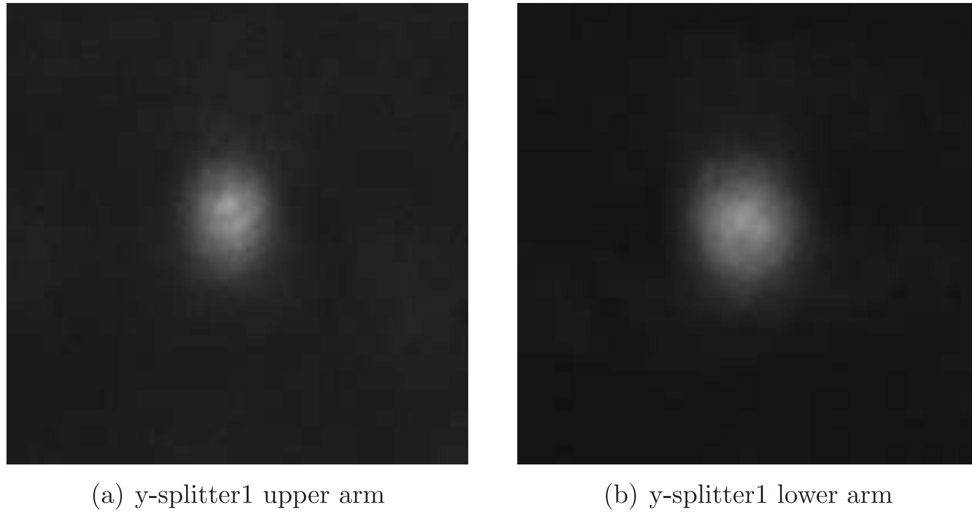

(a) y-splitter1 upper arm (b) y-splitter1 lower arm

Figure 5.19: Optical near-field mode of y-splitter 1 with inter-scan shift.

fiber. By taking the insertion loss of the commercial fiber SM600 as a reference, the estimated propagation loss is approximately 1.1 dB/cm. For y-splitter2, the estimated splitting ratio is approximately 50/50 and the total insertion loss is 9.4 dB. The estimated propagation loss of y-splitter2 is approximately 1.8 dB/cm. Y-splitter1 performs better than y-splitter2 because of the inter-scan shift that increases the refractive-index modification by double-scan. Investigation is still required to further optimise the performance of y-splitters with different structures and different writing paramters.

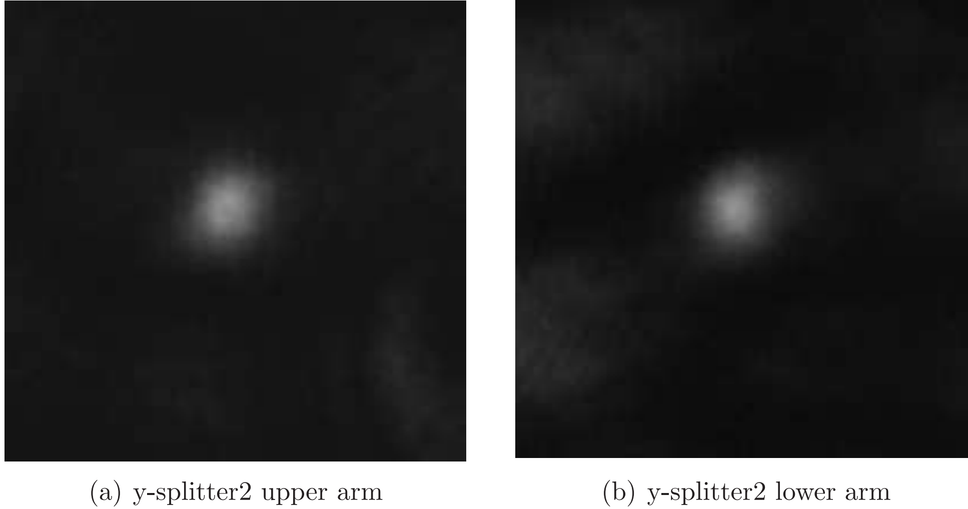

(a) y-splitter2 upper arm (b) y-splitter2 lower arm

Figure 5.20: Optical near-field mode of y-splitter 2 without inter-scan shift.

5.4 Parallel Fabrication

Investigation of the fabrication of other different waveguides is also undertaken. One example is that of multi-spot parallel waveguide fabrication. As discussed in Chapter 3, by applying different phase pattern to an SLM, different multi-foci array can be generated for parallel writing. A few test guides are written with different structures. Figure 5.21(a) shows a 3×3 array fabricated by writing three waveguides simultaneously at the same depth, then repeated three times at three different depths. Figure 5.21(a) shows the near-field mode while coupling light through the written waveguides. Note that the differences in the near-field mode are not only due to differences between the waveguides, but also to different coupling angles. Similar fabrication is also performed with a hexagonal array. However, the characterisation of the written waveguides is not well-measured, and further work is still required to optimise the properties of the written guides.

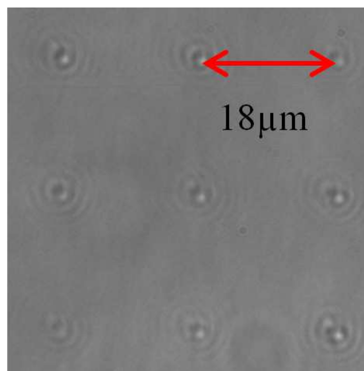

(a) 3×3 array structure

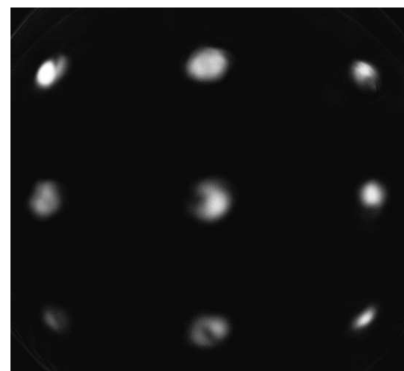

(b) 3×3 array mode

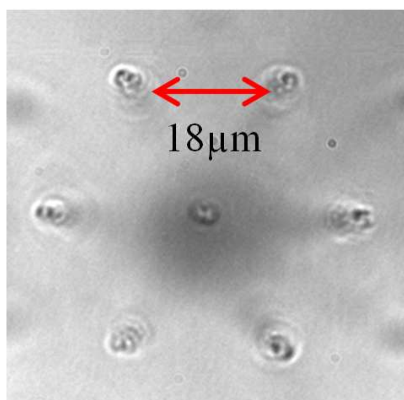

(c) hexagonal array structure

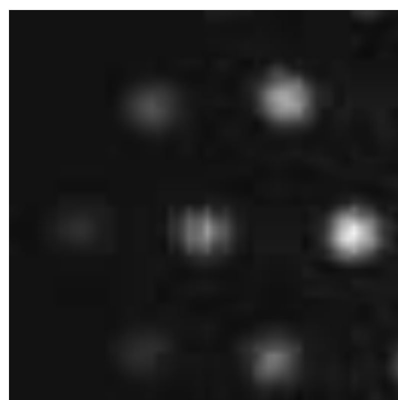

(d) hexagonal mode

Figure 5.21: Parallel writing of two multi-spot waveguides.

5.5 Conclusion

In conclusion, depth-dependent aberration has been corrected for DLW deep below the surface, and waveguides fabricated at various depths in fused silica have been demonstrated. The application of a plasma emission sensing method to the DLW system for adaptive aberration-correction has greatly improved the quality of the focal spot, especially at greater depths. This technique facilitates the fabrication of high-quality waveguides far below the surface, which is significant and useful for the DLW fabrication of 3D optical waveguides. Models and fabrication of a simple y-splitter are presented on the basis of the characteristic parameters of the DLW system. Using the DLW technique to fabricate high-quality waveguides in a single monolithic substrate, advanced 3D optical interconnects and other applications (optical communication, quantum circuits, optical data storage, etc.) can be realized. Other complicated 3D optical waveguides (such as parallel writing) are under study. The novel adaptive DLW system shows the potential for the future design of more complex 3D optical components.

Chapter 6

Ultrafast Laser Fabrication in KDP Crystal

In this chapter, the fabrication of optical waveguides in potassium dihydrogen phosphate (KDP) crystal by ultrafast direct laser writing (DLW) is demonstrated. This is the first time, to my knowledge, that two types of waveguides (type I and type II as discussed in Chapter 2.2) are obtained in KDP crystal. Compared with previous work, smooth regions of modified refractive-index change can be observed in KDP because of the implementation of aberration correction. Although unstable at high temperature, type I waveguides can be stable at room temperature for over 4 months. Type II waveguides are obtained and maintained stable after annealing at 150 ℃ for 2 hours. The result of the KDP fabrication has been published in [69] and the DLW application in KDP crystal for second harmonic generation is summarised in [70].

The chapter begins with an introduction of DLW in KDP crystal. The experimental setup is described and related results are discussed. Analyses and characteristics of the written waveguides are then presented, including refractive-index modifications, transmission losses, polarisation-dependent guiding properties and thermal-annealing effects. Finally, similar results are demonstrated in $LiNbO_3$ crystal.

6.1 Introduction

Ever since the first demonstration of ultrafast DLW of waveguides in glass in 1996 [1], extensive efforts have been made to explore the potential for writing waveguides in many different transparent optical materials [2, 3, 25, 71–74]. The KDP crystal is a widely used nonlinear optical material with a high damage threshold, which is employed in a variety of frequency-conversion applications. Considerable attention has been paid to the fabrication of waveguides in some nonlinear crystals, such as active-ion-doped YAG [75, 76], KT_iOPO_4 [77, 78] and $LiNbO_3$ [28, 79–82]. However, a successful demonstration has never been possible in KDP [31]. One issue affecting KDP in particular is that the threshold for modification of the refractive index is close to the damage threshold, i.e., the laser written waveguide can be easily damaged during its fabrication. Therefore, it is very difficult to control the fabrication parameters carefully enough to be able to produce smoothly modified regions with acceptable refractive-index change inside the KDP crystal.

By implementing the aberration correction with adaptive optics, two types of refractive-index modification can be induced in KDP crystal using our DLW system. For moderate laser powers, type I homogeneous waveguides are created; moreover, at higher pulse energies, type II waveguides are formed in the stressed area surrounding regions of laser-induced damage (please see Section 6.3 for the details of these waveguides). Double-line and four-line structures are applied to the type II guides to increase mode-confinement. Polarisation-sensitivity and the transmission properties of written waveguides are critical properties and are carefully studied. The results indicate that high-quality waveguides can be fabricated in KDP, offering the potential for further applications to nonlinear integrated-optics. Similar results are also presented in $LiNbO_3$ crystal, which has a relatively high refractive index and more severe aberration at greater depths. By applying adaptive aberration correction, the quality of the waveguides in $LiNbO_3$ is greatly improved.

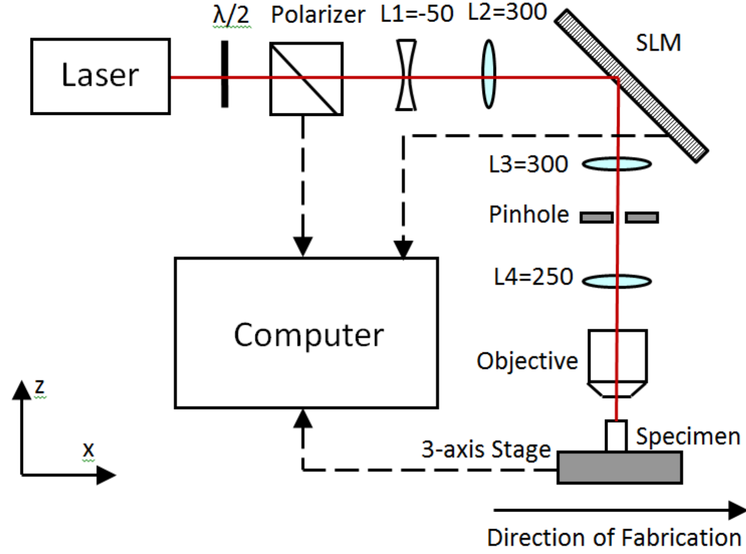

Figure 6.1: Schematic diagram of the ultrafast laser fabrication system. Lens focal lengths are shown in mm. Some intermediate optics have been omitted for clarity.

6.2 Experimental Setup

The fabrication system for KDP crystal is the same as the one used for fused silica, as shown in Chapter 3. Here a schematic diagram of the DLW-fabrication system is shown in Figure 6.1. Again, the femtosecond laser operates at a repetition rate of 1 kHz with 100 fs pulses centered at a wavelength of 790 nm. The beam is adaptively controlled by a spatial light modulator (SLM) for beam shaping and aberration correction [46, 48, 49], as discussed in Chapter 3.

The laser pulses are focused 170 to 250 μm below the surface of a 10-mm-thick KDP sample (10×5×10 mm), which is cut with the optical axis at 67.5° to the x-axis, providing the desired phase-matching conditions for type II spontaneous parametric down-conversion along the x-axis [83]. All waveguides are fabricated at a speed of 10 μm/s along the x-axis (perpendicular to the laser optical axis) at a length of 3 mm. For directly writing type I waveguides, slit beam-shaping is applied on the SLM to achieve a symmetric focal disc for fabrication [46]. The cross-section for structural modifications in type II waveguides is strongly asymmetric because of the

relatively low NA of the objective lens. For characterisation, a laser beam at a chosen wavelength is fiber-coupled into the KDP waveguides and the end facet is imaged with a charge-coupled device (CCD) camera, as described in Chapter 4. Although most of the waveguides are characterised at a wavelength of 535 nm, the guiding properties are also investigated at 415 nm and 630 nm with similar results.

6.3 Experimental Results and Discussion

The properties of the written waveguides are related to numerous fabrication parameters, including pulse energy, translation speed and focus-shaping. Two types of waveguide designs that are typically used for single-mode operation in crystalline materials can be fabricated by varying the pulse energy [3]. At lower pulse energy when no visible material damage occurs, a refractive-index increase is created in the modification region at the focus (Figure 6.2(a)). This type of direct laser writing modification, which is similar to conventional DLW waveguide-fabrication in amorphous materials, produces what is conventionally known as a type I waveguide. Type I waveguides have previously been demonstrated in a few crystalline materials, notably $LiNbO_3$ and have normally been observed to deteriorate with time and disappear after thermal-annealing [28]. Conversely, type II waveguides for which a higher pulse energy is employed during fabrication are permanent and thermally stable. Light-guiding is observed adjacent to the laser damage tracks in the crystal, with the associated induced stress field believed to create a local refractive-index increase. A double-line structure (Figure 6.2(b)) is usually used in type II waveguides to obtain more symmetric and better-confined guiding modes [28, 79–82]. Other four-line structures (Figure 6.3) are also of interest and have been used in some applications.

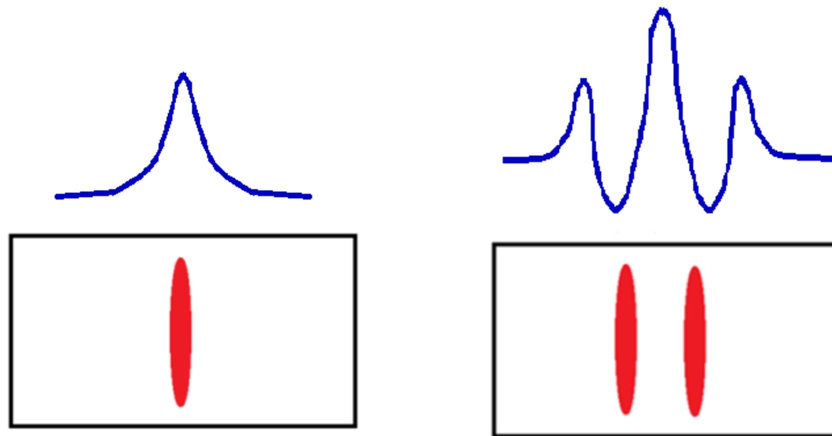

(a) refractive-index type I modification (b) refractive-index type II modification

Figure 6.2: Two types refractive-index modification using the direct laser writing technique in crystalline materials. The red spots are the laser-modified areas, and the blue curves are the estimated refractive-index profiles.

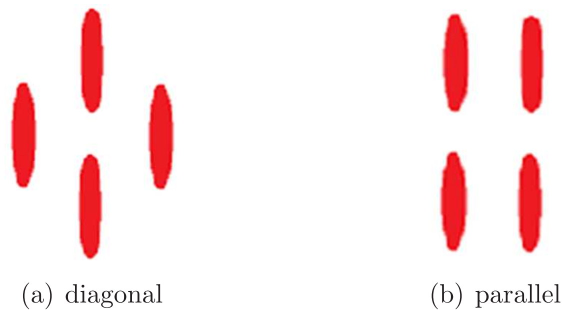

(a) diagonal (b) parallel

Figure 6.3: Four-line waveguide structures: diagonal and parallel.

6.3.1 Type I Waveguide

Figure 6.4 displays a single-line type I waveguide fabricated with a pulse energy of 5.1 μJ (measured at the back aperture of the objective), at a speed of 10 μm/s and with slit beam-shaping. When the refractive index is modified without slit beam-shaping, little guiding can be observed because of the highly asymmetric cross-section. With slit beam-shaping (as discussed in Chapter 3), Figure 6.4(b) shows a circular and homogenous waveguide created by a smooth refractive-index modification in the focal region. Note that careful control of the pulse energy is necessary, as the threshold for observed structural modification is very close to the damage threshold. If the pulse energy is too small (lower than 4.7 μJ), insufficient refractive-index modification is induced, whereas pulse energy that is too high (higher than 5.5 μJ) would damage the material. In both cases, a negligible transmitted optical mode is observed at the end facet and waveguide fabrication is unsuccessful.

The type I waveguide in KDP, in contrast to those reported in $LiNbO_3$, is observed to be stable at room temperature for a period of over 4 months without any change to either the coupled optical mode or the physical appearance of the waveguide when viewed by a transmission microscope. However, after thermal annealing at 150 ℃ for 2 hours, the index-contrast of the type I waveguides deteriorates and light guiding becomes impossible, as shown in Figure 6.4(d)-6.4(f).

The polarisation guiding properties of type I waveguides (before annealing) are investigated by rotating a linear polarizer in front of a CCD camera. Results reveal a highly polarisation-dependent guiding, with only the TM mode (E-field polarized along the y-axis) being observed (Figure 6.5). The reason behind this laser-induced anisotropy is not fully understood, but this possibly indicates that the refractive-index modification constitutes a high degree of birefringence. This further indicates that there may be some reduction of the non-linear properties of the crystal within these type I waveguides.

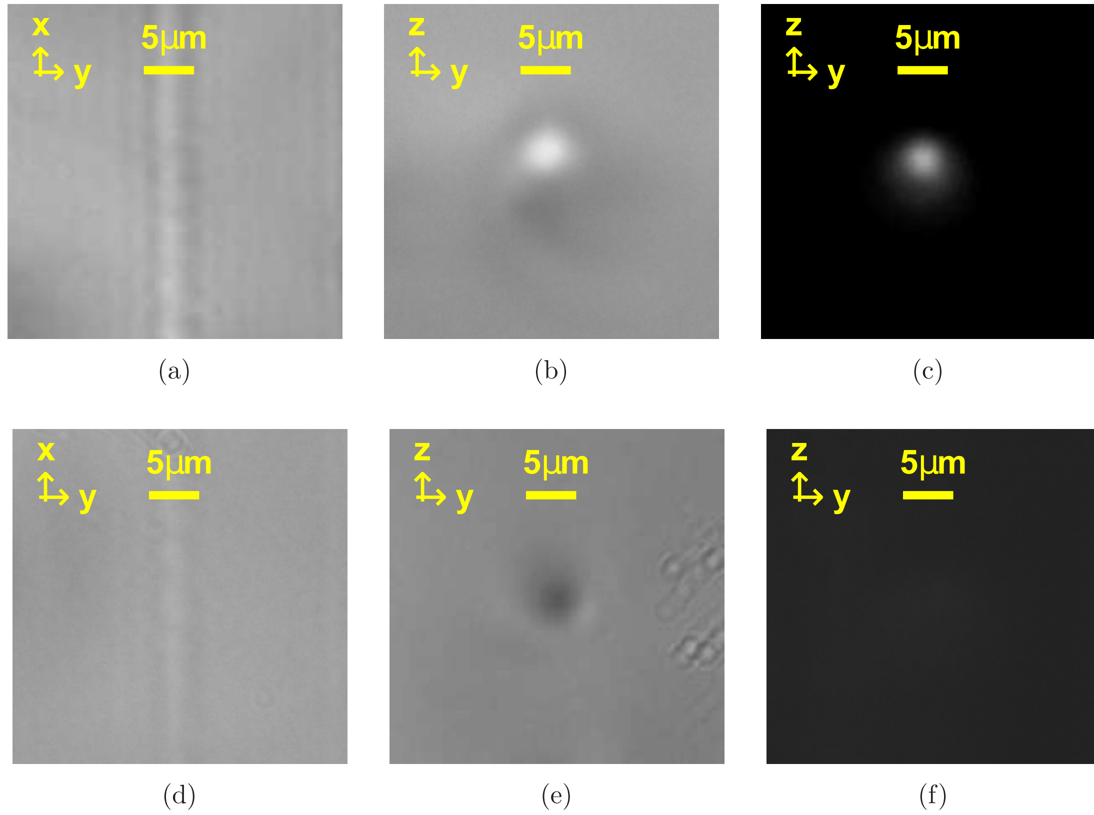

Figure 6.4: Type I single-line waveguide fabricated at a pulse energy of 5.1 μJ and a speed of 10 μm/s, with the slit beam-shaping before (a-c) and after (d-f) annealing. (a)(d) top-down view of the fabricated waveguides under transmission microscope (with slight defocus); (b)(e) cross-sectional view of the fabricated waveguides under transmission microscope (with slight defocus); (c)(f)the near-field intensity distribution for a wavelength of 535 nm at the end of the waveguide.

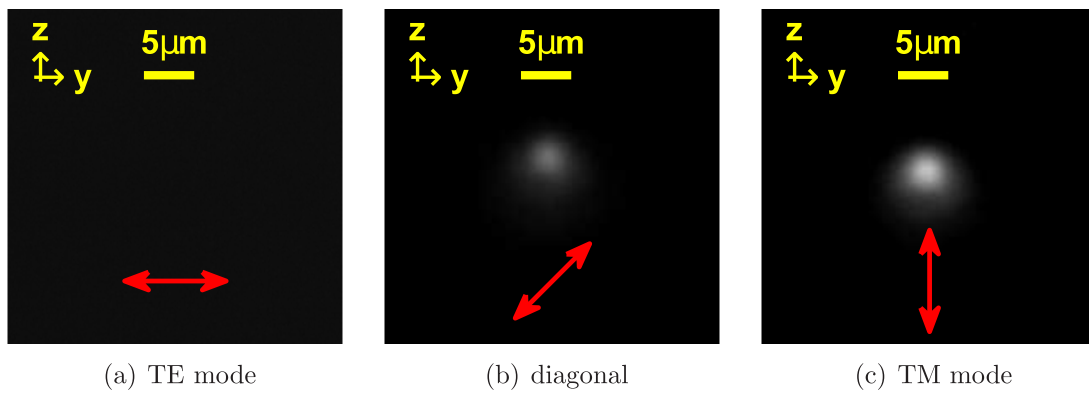

Figure 6.5: Optical mode of type I single-line waveguide at different polarisation. (a) horizontal polarisation (TE mode); (b) diagonal polarisation; (c) vertical polarisation (TM mode).

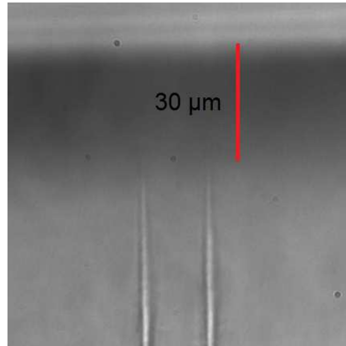

Figure 6.6: Edge view of the waveguides.

A total loss of 5.8 dB at 535 nm is measured for the type I structural modification guided light of the TM mode. As discussed in Chapter 4, significant losses are mainly attributed to butt-coupling into the waveguides with fiber. By comparing the insertion loss with that of the commercial fiber SM600, the actual estimated propagation loss is approximately 1.3 dB/cm. In addition, because of the lack of necessary equipment, I am not able to polish the KDP crystal following fabrication. As a consequence the waveguides terminate $\sim 30\mu$m from the end facet (Figure 6.6), resulting in large losses when fiber-coupling light into the guide. Therefore, the propagation loss of the waveguide should be much less than 1.3 dB/cm.

The refractive-index profile of TM light for type I waveguides is estimated on the basis of the propagation-mode near-field method (PMNFM) [37]. The calculated refractive-index profile is presented in Figure 6.7(a), with a refractive-index difference of 2.3×10^{-3} at its peak. The field distribution of the fundamental mode for the calculated refractive-index profile is shown in Figure 6.7(b), with a mean square error of 1.9×10^{-3} from the measured field profile. These results are in good agreement with measurements from quantitative phase microscopy (TIE) [65].

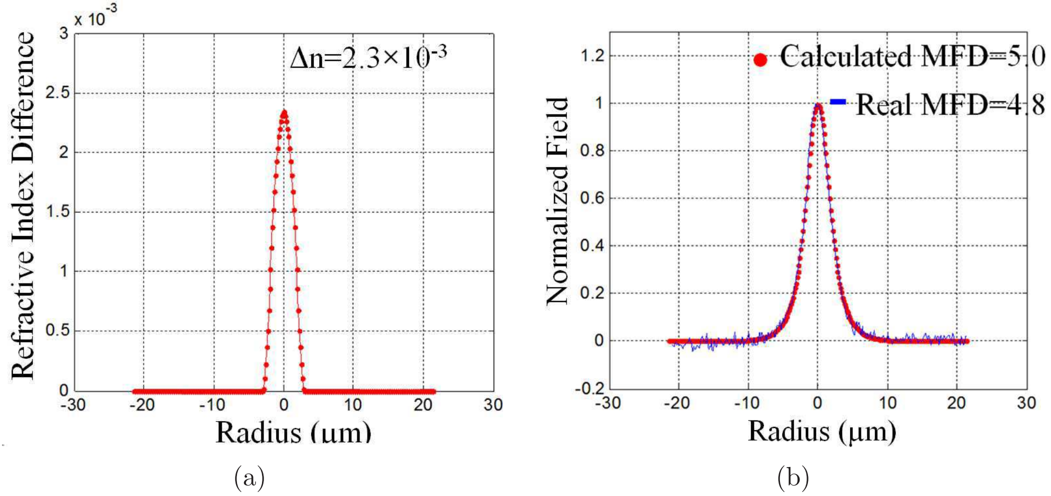

Figure 6.7: Refractive-index modification of type I single-line waveguide. (a) calculated refractive-index profile using propagation mode near-field method; (b) measured and calculated field distribution of the fundamental mode.

6.3.2 Type II Waveguide

For pulse energies above 0.17 μJ without any beam shaping (uniformly illuminated objective pupil), tracks are induced that are clearly visible as faults in the KDP crystal lattice. Such tracks are found to guide light adjacent to the region of laser damage in analogy with type II waveguides observed in other crystalline materials [3]. Normally, a double-line structure is applied for type II waveguides to improve mode-confinement. Proper separation distance (in the y-axis) between two adjacent lines is chosen to achieve optimal guiding, as shown in Figure 6.8. If the two lines are too close, a nonuniform refractive-index distribution occurs between the adjacent stress fields of the two damaged tracks. If the two lines are too far apart, the behaviour is similar to that of a single-line damaged track whose mode cannot be well-confined. For the system, 15μm is found to be the optimal separation distance.

Clearly, the transmitted mode of the type II waveguide (Figure 6.8(c)) is not as well-contained as that of the type I waveguide(Figure 6.4(c)). Three different type II waveguide structures are investigated in an attempt to improve the mode-confinement, as shown in Figure 6.9. Based on the result from Figure 6.8, the in-

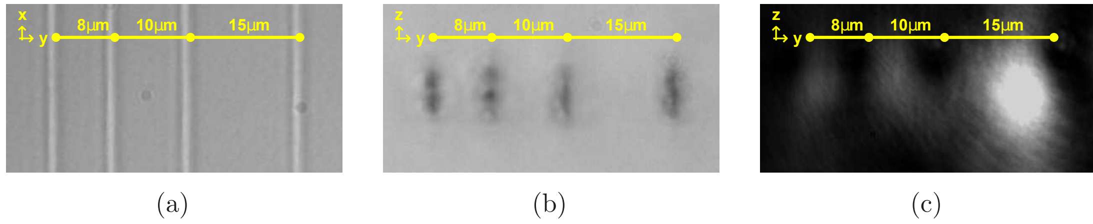

Figure 6.8: Type II double-line waveguides written at a pulse energy of 0.17 μJ and a speed of 10 μm/s, without slit pupil beam-shaping. (a) top-down view of the fabricated waveguides under microscope; (b) cross-sectional view of the fabricated waveguides under microscope; (c) the near-field intensity distribution for a wavelength of 535 nm at the end of the waveguide.

tuitive four-line structures that I first use to better confine the mode are shown in Figure 6.9(a) and Figure 6.9(b). Their resulting optical modes are shown in Figure 6.9(d) and Figure 6.9(e), which are better confined than that in Figure 6.8(c). A double-line structure with greater axial elongation in Figure 6.9(c) is also investigated. The axial elongation of the laser-induced features is increased by reducing the effective NA of the objective lens using the SLM [46].

Results shows that the three structures have similar guided modes. As it offers faster fabrication, a more circular mode and a simpler structure, the elongated double-line structure (Figure 6.9(c)) is therefore chosen for further investigation. Attention should be paid to selecting appropriate dimensions for the elongated focus. The optimal size applied in the experiment is approximately 2 μm$\times$15 μm, corresponding to an effective NA of 0.3. A less-elongated focus would result in inferior mode-confinement, whereas a more-elongated one would dramatically increase the pulse energy necessary for fabrication. In contrast to the type I waveguide, the properties of the type II waveguide are much less sensitive to the fabrication pulse energy.

The type II waveguides are stable at room temperature for over 4 months without any change in the coupled optical mode. After thermal-annealing at 150 ℃ for 2 hours, the type II waveguide continues to exist (unlike the type I waveguides), but with changes in the intensity distribution of the guided mode (as can be seen

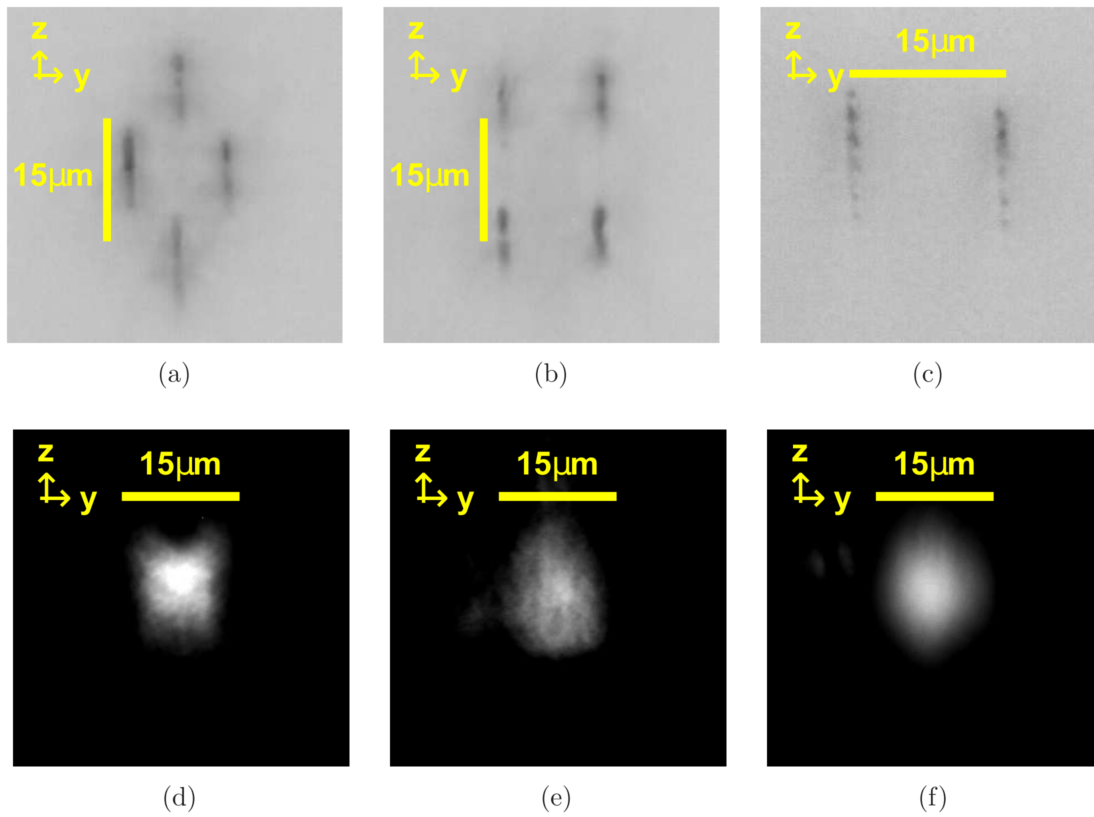

Figure 6.9: Type II waveguides with different structures. (a-c) cross-sectional view of different waveguide structures under microscope ; (d-f) the near-field intensity distribution for a wavelength of 535 nm at the end of respective waveguide structures (a-c).

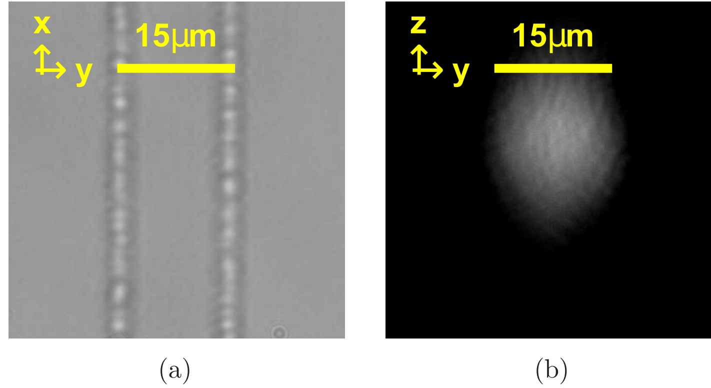

(a) (b)

Figure 6.10: Type II elongated double-line waveguide written at a pulse energy of 1.2 μJ and a speed of 10 μm/s after annealing. (a) top-down view of the fabricated waveguides under microscope; (b) the near-field intensity distribution at the end of the waveguide.

by a comparison between Figure 6.10(b) and Figure 6.9(f)). Under inspection with a transmission microscope, it is found that the laser-induced damaged track (Figure 6.10(a)) changes under annealing, revealing a much greater nonuniformity along its length. This is likely to affect the refractive-index profile of the guide, thus affect the guiding mode.

The polarisation-guiding properties of the type II waveguide (before and after annealing) are also investigated. The type II waveguides are much less polarisation-dependent relative to the type I guides discussed previously. It is shown in Figure 6.11 that before annealing, the type II waveguides act in both polarisation states, but with a propagation-loss that is still polarisation-dependent. After annealing, the waveguide becomes almost polarisation-independent, showing the potential for applications such as the generation of pure heralded single photons [84].

A total loss of 7.8 dB at 535 nm is measured for the elongated double-line type II waveguide for circular polarisation. Again, this is mainly due to the high coupling loss, and the estimated loss of the waveguide is approximately 3.3 dB/cm. An additional loss of 1.3 dB loss is observed for guiding after annealing. The refractive-index profiles of the type II waveguide after annealing are also estimated on the basis of the

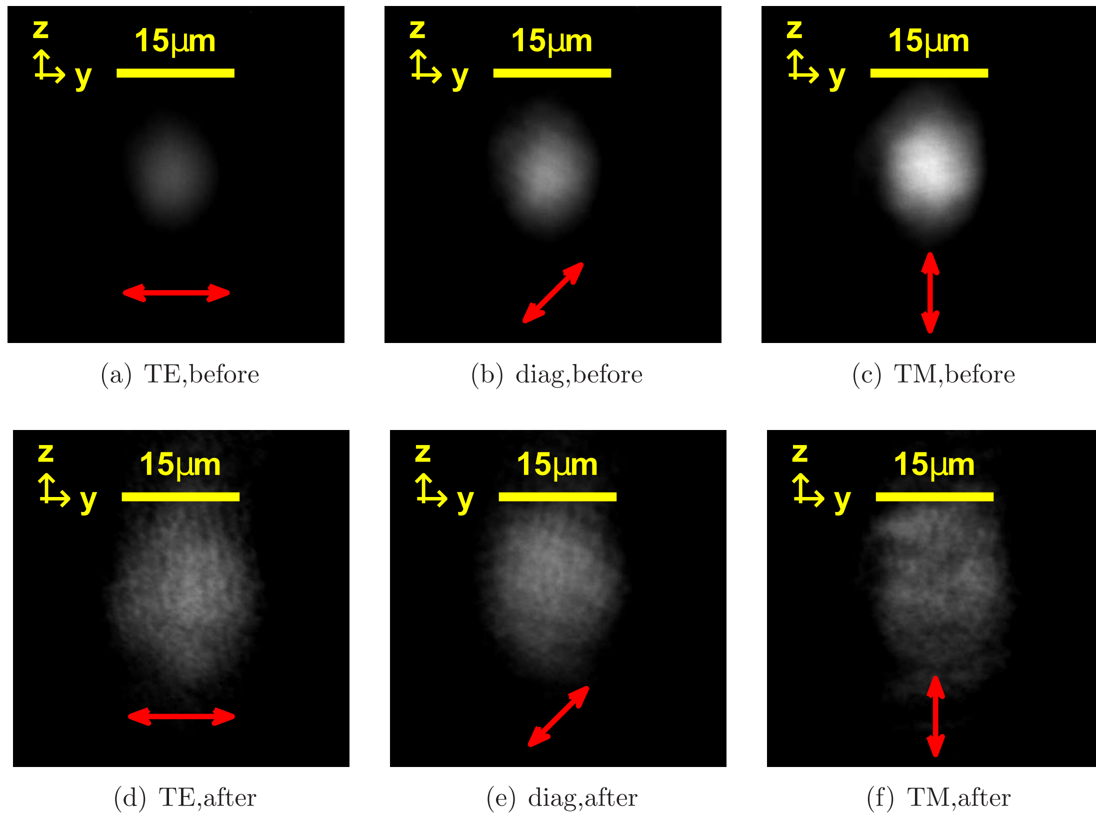

(a) TE,before (b) diag,before (c) TM,before

(d) TE,after (e) diag,after (f) TM,after

Figure 6.11: Optical mode of type II elongated double-line waveguide at different polarisations before (a-c) and after (d-f) annealing. (a)(d) horizontal polarisation (TE mode); (b)(e) diagonal polarisation; (c) (f) vertical polarisation (TM mode). Note that the power coupled into the guide is increased by a factor of 1.85 for images (d-f).

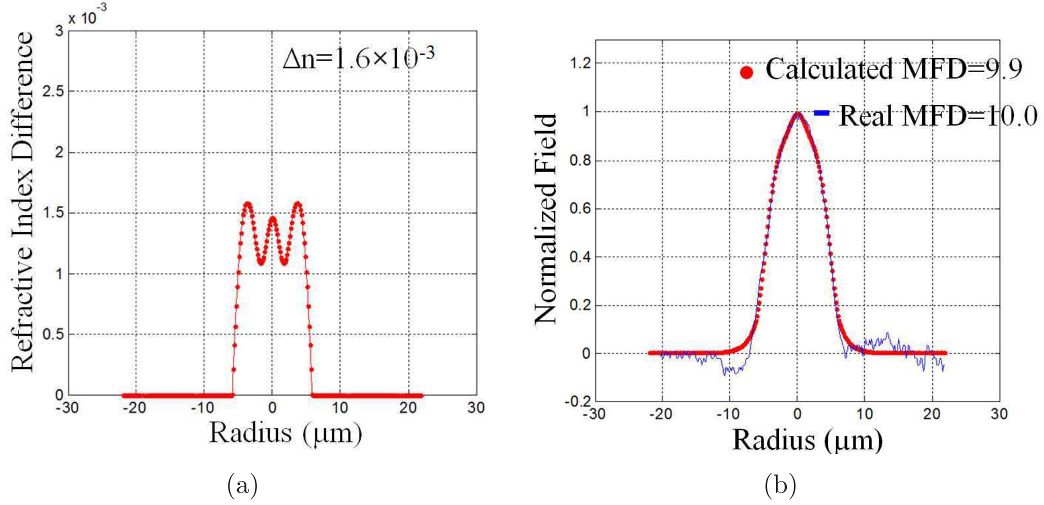

Figure 6.12: Refractive-index modification of type II elongated double-line waveguide after annealing. (a) calculated refractive-index profile using propagation mode near-field method; (b) measured and calculated field distribution of the fundamental mode.

PMNFM. The calculated refractive-index profile of the type II waveguide is shown in Figure 6.12(a), with a refractive-index difference of 1.6×10^{-3} at the center of the peak. The field distribution of the fundamental mode for the calculated refractive-index profile has a mean square error of 4×10^{-3} from the measured field profile. The main contributor to the error is the measurement noise from the background around the boundary.

6.4 Ultrafast Laser Fabrication in $LiNbO_3$

Lithium niobate ($LiNbO_3$) has been widely used for active optical applications, because of its excellent electro-optic, acousto-optic and nonlinear optical properties. Due to its applicability to integrated optical devices, $LiNbO_3$ is one of the first crystals to be investigated for DLW waveguides. Compared with KDP or fused silica, two significant shortcomings exist for $LiNbO_3$. First, it has been reported that type I waveguides in $LiNbO_3$ are not stable after low-temperature annealing or even have a gradual decay of light guidance at room temperature [85]. As a result, type II waveg-

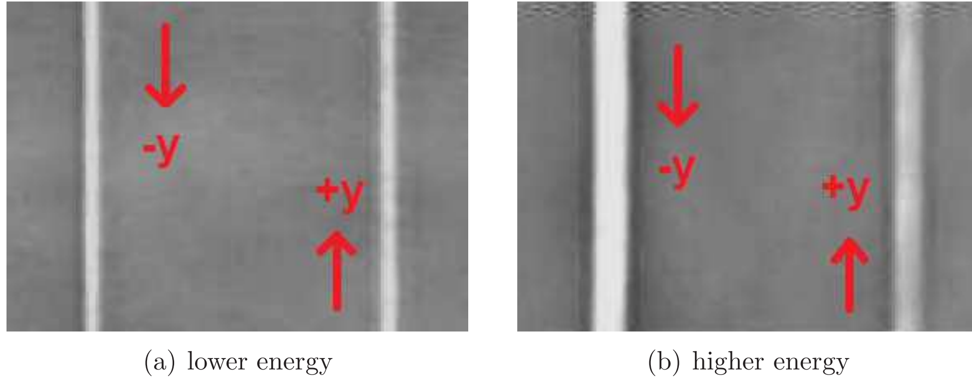

(a) lower energy (b) higher energy

Figure 6.13: Non-reciprocal phenomenon of double-line type II waveguide in $LiNbO_3$.

uides seem to be more commonly used than type I in $LiNbO_3$. The second drawback of DLW fabrication in $LiNbO_3$ is its relatively higher refractive index (n≈2.3 at a wavelength of 600 nm), resulting in highly-aberrated laser pulses, especially deep below the surface.

During the fabrication, it is observed that the DLW fabrication in $LiNbO_3$ is direction-dependent. Normally, for a double-line structure, one waveguide can be finished by going down (-y) for the first track and down (+y) for the second one. An obvious difference is observed by writing in opposite directions, which is called the non-reciprocal phenomenon [86]. Asymmetric writing in opposite directions is not observed in fused silica or in $LiNbO_3$ when the pulse energy is low ($< 4\mu$J in Figure 6.13(a)). However, at high pulse energy ($> 9\mu$J), fabrication along -y direction results in much higher refractive-index modification than +y direction (Figure 6.13(b)).

This non-reciprocal phenomenon is very rare in optics. It appears in $LiNbO_3$ because of the asymmetry in the crystal structure, and the beam interacts with the crystal differently with different directions of light propagation. When the direction of the laser beam is reversed from +z to -z directions, fabrication along +y direction results in higher refractive-index modification than -y direction. More tests into this non-reciprocal phenomenon are required for further investigation.

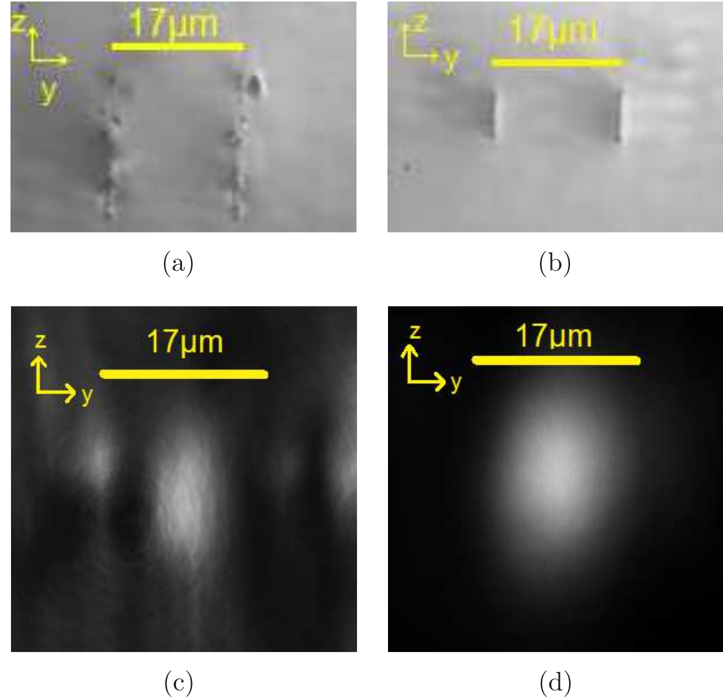

Figure 6.14: Microscope and optical mode images of type II double-line waveguide in $LiNbO_3$ before and after aberration correction. (a)(c) cross-sectional view and optical mode image before aberration correction; (b)(d) cross-sectional view and optical mode image after aberration correction.

Therefore, the double-line structures in $LiNbO_3$ are fabricated in identical direction (+y) in order to obtain symmetric waveguide profiles. Figure 6.14(a) shows a double-line type II waveguide fabricated in $LiNbO_3$ without any aberration correction. Under inspection with a transmission microscope, it is found that the laser-induced damage tracks (Figure 6.14(a)) have great non-uniformity. This results in poor confinement of the transmitted mode and poor guiding performance (Figure 6.14(c)).

By taking advantage of the DLW with adaptive optics offering aberration correction, the resulting type II waveguide and its optical mode are obtained as shown in Figure 6.14(b) and Figure 6.14(d). Similar to KDP, a proper separation distance of 17 μm (in the y-axis) between two adjacent lines is chosen to achieve optimal guiding. Results show that type II waveguides in $LiNbO_3$ are stable at room temperature for

over 1 month. A total loss of 6.7 dB at 535 nm is measured for the double-line type II waveguide. Again, this is mainly due to the high coupling loss and the estimated loss of the waveguide is approximately 2.1 dB/cm.

6.5 Conclusion

I have demonstrated femtosecond written waveguides in KDP for the first time. Depending on the incident fabrication pulse energy, structures supporting both type I (guided mode contained within the fabricated region) and type II (guided mode adjacent to the fabricated region) waveguides are formed. Note that, to the best of my knowledge, this is the first ever demonstration of waveguides in KDP crystal. Smooth and room-temperature stable type I waveguides have been created with the appropriate pulse energy. However, type I waveguides are highly polarisation-dependent with only the TM mode being transmitted. In addition, they are also found to disappear after annealing at 150 ℃ for 2 hours. Conversely, type II waveguides with an elongated double-line structure persist after annealing and demonstrate polarisation-independent waveguiding. The type II waveguides also have the advantage of easy fabrication compared to type I waveguides, which require careful control over the pulse energy. Finally, type II waveguides with aberration-correction have also been fabricated in $LiNbO_3$, enabling substantial improvement in the quality of DLW-fabricated waveguides and their resulting guiding properties.

Chapter 7

Quantum Random Number Generation

A high-speed quantum random number generation (QRNG) scheme on the basis of quantum phase fluctuations is proposed in this chapter. Although the QRNG system is not directly related to the previous chapters, the potential application of the direct laser writing (DLW) to quantum information area has attracted considerable interest. This project is done in collaboration with the quantum information group at the University of Science and Technology of China. With the possibility of a more stable and compact interferometer provided by DLW, the QRNG scheme can be implemented at an ultrahigh speed and eventually integrated onto a chip. The result has recently been published [87] and highlighted in the MIT Technology Review as the World's Fastest Quantum Random Number Generator[1].

First, the background on the development of QRNG is reviewed and a discussion on how the DLW technique can play a key role in miniaturization of the QRNG system is presented. A 68-Gbps high-speed QRNG system on the basis of quantum phase fluctuations is then introduced. The randomness analysis is discussed to quantify

[1]http://www.technologyreview.com/view/538406/worlds-fastest-quantum-random-number-generator-unveiled-in-china

the quantum randomness of the raw data and data post-processing is applied for randomness extraction [88]. Finally, experiment shows that the generated random number files can pass the standard randomness tests, which indicates a good level of true randomness.

7.1 Introduction

In the modern information society, random numbers play an indispensable role in various areas, ranging from lotteries to high-tech national security. A random string is a sequence of numbers generated by a physical or computational method that is hard (or even impossible) to predict. In classical information theory, computational algorithms are used for random number generation (RNG), based solely on deterministic logic. This type of RNG is often known as pseudo RNG, and can never produce “true” random numbers because its output can be predicted when sufficient computational power are performed. Clearly, when the key is predictable, no secure cryptosystem can exist.

True RNGs can only be on the basis of physical processes. Some naive physical approaches such as dice-tossing and coin-flipping, might be useful in applications that do not require high-speed bit rates such as lotteries. Hardware RNGs originating from physical processes such as noise in electric devices, nuclear fission, and circuit and radial decay, are believed to be able to offer better random numbers. However, the origins of the randomness from these approaches are unclear, because these schemes normally involve complicated Newtonian processes that may produce no randomness.

QRNG provides means to generate randomness stemming from the nondeterministic nature of quantum physics. In QRNG, true randomness can be guaranteed by the fundamental laws of quantum mechanics [89]. In the early development of QRNG schemes, single-photon detectors were normally required [90–92]. For example, by

simply measuring the path selection of single photons while passing through a beam splitter, random numbers can be generated. The generation speed can be improved by extracting more than one bit of information from a single-detection event. The bottle neck for such schemes lies in the time-resolution of the single-photon detector and the detector dead time. For a single-photon detector, after detection, the device is set to "inactive" for a short period of time in order to allow the system recover to the initial stage. This "inactive" time is called detector dead time.

Bit rate is the key parameter for characterising the performance of QRNG, especially for some special applications. For instance, given a 10 GHz clocked quantum key distribution system [93], a random bit stream beyond 40 Gbps is required. In order to solve these application issues for QRNG, various schemes have been proposed to replace expensive and low-performance single-photon detectors with low-cost and highly efficient photodetectors. Such schemes require the exploitation of another physics principle – vacuum fluctuation [94–96]. This scheme can be implemented by sending a strong local oscillator through a beam splitter and detecting the differential signal of the two output beams with a balanced optical receiver. The input of the unused port of the beam splitter can be regarded as a vacuum state. The randomly chosen quadrature of the vacuum state is measured by beating it with the local oscillator. The output interference signal is strong enough to be detected with a high-speed and low-cost photodiode operated at room temperature.

In practice, the photodiode itself contributes access noise, which may introduce bias into the output random numbers. To acquire reliable random numbers, it is thus important to operate the detector in the shot-noise limit, where the overall observed noise is dominated by the vacuum noise. However, building a broadband shot-noise limited homodyne detector beyond a few hundred MHz is technically challenging.

In order to go beyond the bandwidth limitation of a shot-noise limited homodyne detector, QRNG schemes on the basis of quantum phase fluctuations have been devel-

oped [97,98]. The phase noise of a single-mode laser can be attributed to spontaneous emission, which is random according to quantum mechanics [99]. The phase noise of a macroscopic laser field can be easily measured via an interferometer by converting phase into intensity. The intensity output from the interferometer is measured by conventional low-cost and high-speed photodetectors rather than single-photon detectors. This removes the speed limitation of single-photon detectors, and can significantly increase the bit rate of the QRNG system. The reported QRNG systems using the quantum phase fluctuations have demonstrated bit rates of 500 Mbps [97] and 6 Gbps [98]. In the system, a high-speed of 68 Gbps and low-cost QRNG is achieved, which is one order-of-magnitude improvement compared with the previous work. To achieve this rate, the laser is operated at its threshold level when quantum noise is dominant. The stable interferometer is designed with active feedback, which eliminates the phase fluctuation of the interferometer without any temperature control. After modelling and quantifying the contribution of quantum noise, quantum random bits are finally generated.

The key device in the high-speed QRNG system is an actively stabilized interferometer, which can be potentially replaced by a more stable and compact interferometer using DLW in the near future. Note that the size of QRNG is an important factor for its applications. Modularization and miniaturization is the future direction of QRNG, where waveguide will be widely employed.

7.2 Experimental Realisation

The experimental setup is shown in Figure 7.1(a). A 1,550 nm continuous wavelength (CW) laser diode (LD), driven by a constant current, is operated slightly above its threshold. This ensures that the main contribution to the phase fluctuations comes from spontaneous emission, rather than from the chaotic evolution of the macroscopic

field [100]. The laser beam enters a homemade polarisation-insensitive Michelson interferometer after passing through a circulator. The interferometer comprises a three-port circulator, a 50/50 beam splitter (BS), a phase shifter (PS) and two Faraday rotator mirrors (FRMs). The fiber length of the homemade interferometer is approximately a few meters, and can be potentially replaced by a more stable and compact DLW written waveguide interferometer in the near future. A time delay of approximately 3.735 ns between the two arms of the interferometer is much smaller than the coherence time of the laser. With such a configuration, two FRMs can effectively remove polarisation effects, making the interferometer polarisation-insensitive. The interferometer has two output ports, i.e., OUT1 and OUT2, as shown in Figure 7.1(a). OUT1 is monitored by an optical power meter (PM). The measurement results of the PM are uploaded to a computer, in which a proportional-integral-derivative (PID) algorithm is implemented. The PID program sends feedback signals to an open-loop piezo controller (PC, Thorlabs MDT694B) to precisely tune the PS in real-time. In this way, phase stabilisation in the interferometer can be maintained at a high level and conventional temperature control for the interferometer is not required.

When there are no feedback signals, the phase drifts over the whole [$-\pi$,$+\pi$] range, making the phase-measurement results invalid. In this case, temperature control is required for the stability of the interferometer. After applying feedback signals, a typical measurement result of OUT1 over 20 minutes is shown in Figure 7.1(b), and no temperature control is needed in our case. The phase of the interferometer maintains at a high level and OUT1 is almost constant, which indicates that the interferometer is stable over a reasonable amount of time. The small fluctuations of the signal can be regarded as classical noise. OUT2 is detected by a 15 GHz photodetector (PD, EOT ET3500F). The voltage output of the PD is sampled by an 8-bit analog-to-digital converter (ADC) in a 12 GHz oscilloscope (Agilent DSA91204A) and raw data are generated. Limited by the memory size of the oscilloscope, 20.5 million points or 164

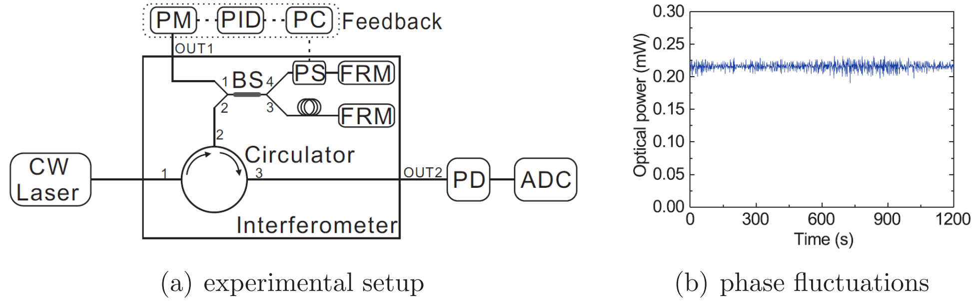

(a) experimental setup (b) phase fluctuations

Figure 7.1: (a) Experimental setup of the quantum random number generation system. Photons emitted from a CW laser enter a polarisation-insensitive Michelson interferometer after passing through a circulator. OUT1 is monitored by a PM, and OUT2 of the interferometer is detected by a PD. A computer reads the PM signal and uses the PID algorithm to send feedback signals to a PC for PS control. The outputs of PD are sampled by an 8-bit ADC in a high-speed oscilloscope. BS: beam splitter; PS: phase shifter; PM: power meter; PC: piezo controller; FRM: Faraday rotator mirror; PID: proportional-integral-derivative control; PD: photodetector; ADC: analog-to-digital converter. (b) Optical power measured at OUT1 of the interferometer over 20 minutes with feedback signals, indicating that the active phase stabilisation for the interferometer works well.

million bits are acquired each time to form one raw data file. At a sampling rate of 10 GSa/s, the corresponding data acquisition period is 2.05 ms. The raw data is then transferred to a computer for post-processing.

From Figure 7.1, one can see that all parts except the interferometer can be simply integrated on a small printed circuit board, implying that compact and high-speed QRNG modules or components are not far from realisation. The size of the interferometer is the bottleneck for performing QRNG on a chip. The DLW technique can provide more compact interferometers and reduce the size of components significantly. This technology can greatly promote the miniaturization and practicality of high-speed QRNGs.

The quantum phase fluctuations measured are often mixed with classical noise. The min-entropy of the raw data is evaluated by modelling the system and is used to quantify the quantum randomness. Thus, the bias of the raw data caused by other signals, such as classical and detection noises, can be removed by Toeplitz-matrix

hashing randomness extraction [88]. The final random numbers should be examined through standard randomness tests.

7.3 Analysis and Data Post-processing

Photons emitted from a laser normally come from two sources: stimulated and spontaneous emission. In the standard quantum optics model, photons from stimulated emission are assumed to have fixed phases, whereas the ones from spontaneous emission have random phases and can be used as a quantum random source. However, when the total phase of photons is measured, quantum phase fluctuations are often mixed with classical noise. It is necessary to make the ratio between quantum noise and classical noise as high as possible. Therefore, an experiment was performed which reveals that when the laser is operated around its threshold level, spontaneous emission is high enough to dominate the phase fluctuations. With an interferometer, the phase fluctuations are transmitted into intensity fluctuations and then measured by the photodetector. Compared with previous schemes, the quantum phase noise can be easily measured by classical photodetectors rather than low-speed single-photon detectors, which therefore greatly increases the bit rate of QRNG.

Once the raw data is obtained, its randomness is evaluated by the model described in [97, 98]. First, the electric field of the CW laser can be modelled as follows:

$$E(t) = E_0 \exp[i(\omega_0 t + \theta(t))] \tag{7.1}$$

Subsequently, the interferometer output intensity (after interference) with a time delay of ΔT is given by

$$2E_0^2 + 2E_0^2 \cos\left[\omega_0 \Delta T + \theta(t + \Delta T) - \theta(t)\right] \tag{7.2}$$

Here, the phase fluctuations of the laser source are measured by the phase difference between times t and $t + \Delta T$, defined as $\Delta\theta(t) = \theta(t + \Delta T) - \theta(t)$. After subtracting the direct current signal, the measured signal can be described by

$$I(t) \propto P \cos(\omega_0 \Delta T + \Delta\theta(t)) \tag{7.3}$$

As shown in Figure 7.1(a), the PS in the interferometer is constantly tuned such that $\omega_0 \Delta T$ maintains $2m\pi + \pi/2$ (m is an integer). Because $\Delta\theta(t)$ is small, we have

$$I(t) \propto P \sin(\Delta\theta(t)) \approx P\Delta\theta(t) \tag{7.4}$$

Therefore, the phase fluctuations of the laser source can be measured directly by the intensity of the interferometer output. In addition to the signals from phase fluctuations, the variance of the photodetector output also contains background noise as follows:

$$\langle V(t)^2 \rangle = AP^2 \langle \Delta\theta(t)^2 \rangle + F \tag{7.5}$$

where A is the linear response constant between the optical input signal and the photodetector voltage output. Meanwhile, as mentioned before, the total phase fluctuations can be divided into signals from quantum fluctuations (Q/P) and classical fluctuations (C) [97, 98],

$$\langle \Delta\theta(t)^2 \rangle = Q/P + C \tag{7.6}$$

Finally, there are three contributors to the intensity variance:

$$\langle V(t)^2 \rangle = AQP + ACP^2 + F \tag{7.7}$$

where AQP is the quantum signal of interest that should be maximised, compared with the classical counterpart $ACP^2 + F$. The classical noise can be removed with

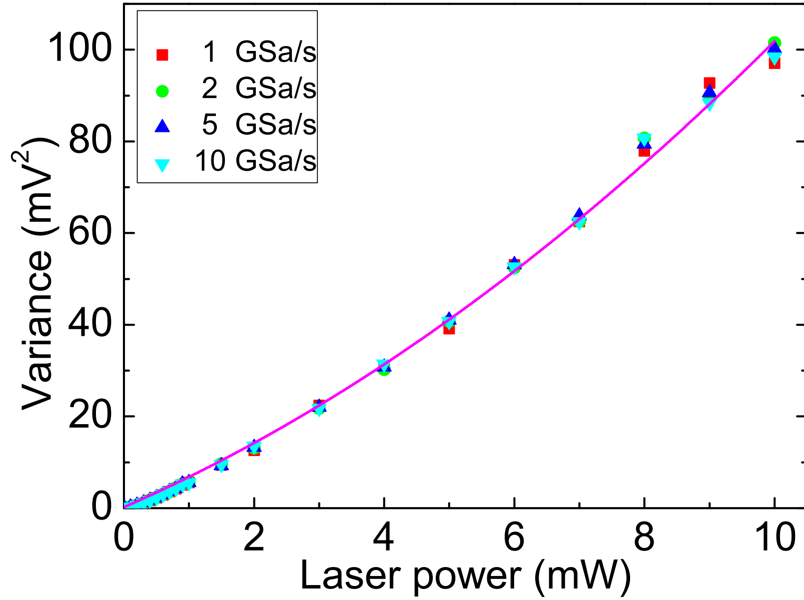

Figure 7.2: The PD amplitude variance as a function of LD power at different sampling rate ranging from 1 GSa/s to 10 GSa/s. The solid line represents the theoretical fit at a sampling rate of 10 GSa/s.

randomness extraction to obtain the final random bits.

According to Equation (7.7), by changing the laser power P, the parameters of AQ, AC and F can be estimated via data fitting. In experiments, different amplitude variances of the PD output are measured by precisely tuning the LD power from minimum to 10 mW. The PD output is sampled by the oscilloscope with different sampling rates. The results are shown in Figure 7.2. The signal variances response to the laser power at four different sampling rates consistently. The minor differences are caused by the access noise of the measurement, such as the bandwidth and resolution of the oscilloscope. The measured values are then fitted, and the results are listed in Table 7.1. As one can see, the fitting values are consistent in the four different sampling cases.

In order to quantify the randomness of the raw data, a min-entropy evaluation model is developed on the basis of the QRNG system. To maximise the min-entropy of the raw data, one can optimise the ratio of the quantum signals to other noises [88,98],

Table 7.1: The theoretical fitting values of the parameters at four sampling rates.

Parameter	1 GSa/s	2 GSa/s	5 GSa/s	10 GSa/s
AQ (mV^2/mW)	6.0142	5.8581	6.0569	6.2068
AC (mV^2/mW^2)	0.4201	0.4563	0.4279	0.3958
F (mV^2)	0.1714	0.2052	0.2200	0.2162
R^2	0.9977	0.9988	0.9989	0.9982

which is defined as

$$\gamma = \frac{AQP}{ACP^2 + F} \tag{7.8}$$

This allows the value of γ to be calculated on the basis of the fitted values of parameters listed in Table 7.1. Meanwhile, to verify that the calculated γ is accurate, an experimental approach [98] is employed to directly measure this parameter. Because the classical noise should dominate the phase fluctuation when the laser power is sufficiently high; therefore one can assume that the quantum signal to classical noise ratio, γ, is close to 0 when the LD is operated at its maximum power. Then the classical noise, AC, can be directly measured (upper bounded). Note that any finite value of γ in the high-power regime would result in an underestimation of the min-entropy evaluation, which is allowed because it is the lower bound of the min-entropy that is used for data post-processing.

In the experiment, the laser is operated at its maximum power (around 12 mW) and a digital variable attenuator is used before the interferometer to tune the incident power from minimum to 12 mW. Note that the key difference between this setup and the one to acquire data for Figure 7.2 lies on the position of the variable attenuator. With this setup, the voltage variance caused by the classical noise at each power can be directly measured. Combining the total voltage variance as measured in Figure 7.2, the experimental values of γ with different laser powers and different sampling rates are obtained and shown in Figure 7.3. The experimental results are consistent with the theoretically calculated values. For our QRNG, the signal-noise ratio reaches its peak value, $\gamma = 5.46$, at a power of 0.9 mW. Under this optimal condition, signals caused

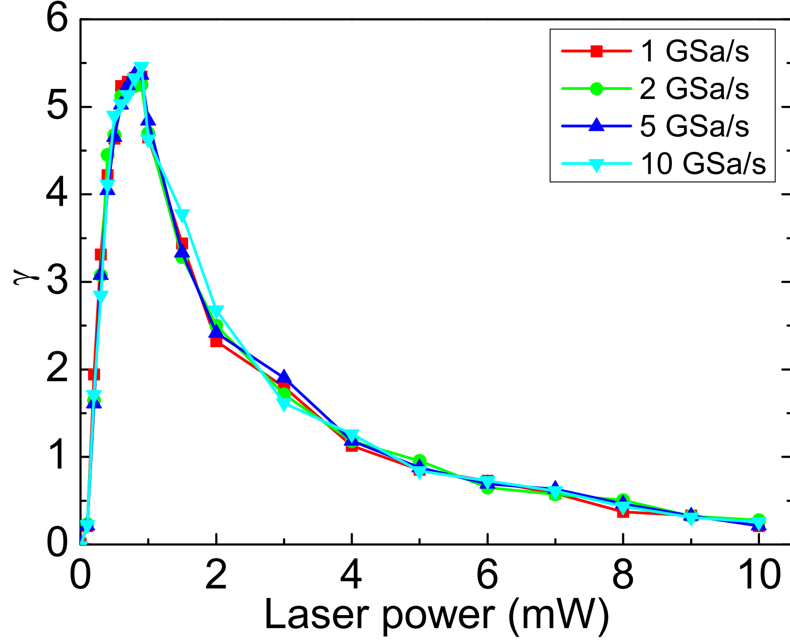

Figure 7.3: The quantum signal to classical noise ratio γ as a function of LD power at different sampling rates. When the LD power is around 0.9 mW, γ reaches the maximum value, 5.46.

by quantum phase fluctuations dominate the sampling output. In the experiment, the LD is always operated at the optimal power to generate raw random data.

According to a theoretical model in [88], the quantum signal follows a Gaussian distribution. By combining Equation (7.7) and Equation (7.8), the variance of the Gaussian quantum signal is given as follows:

$$\sigma^2_{quantum} = AQP = \frac{\gamma}{\gamma+1}\langle V(t)^2\rangle \tag{7.9}$$

which gives complete knowledge about the distribution of the quantum signal.

The min-entropy is then defined as follows:

$$H_\infty(X) = -\log_2(\max_{x\in\{0,1\}^n} P_r[X = x]). \tag{7.10}$$

The maximum probability, $P_r[X = x]$, should be calculated according to the

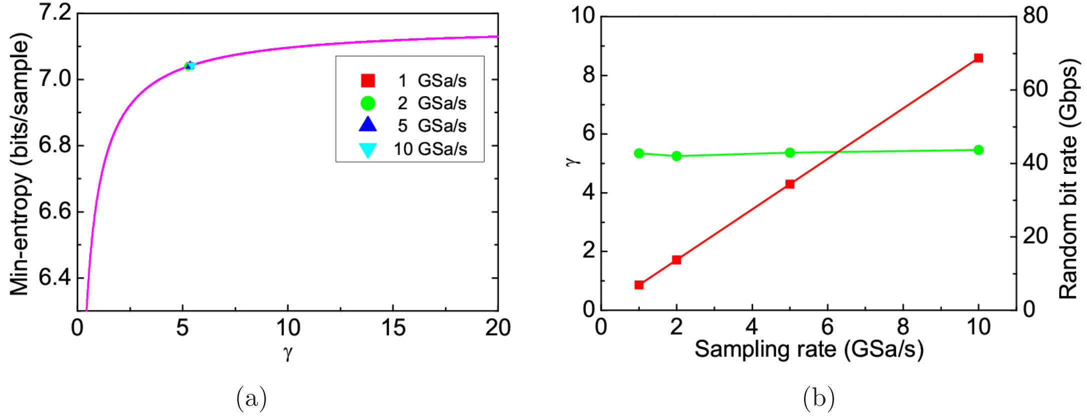

(a)

(b)

Figure 7.4: (a) The plot of min-entropy versus γ. Symbols and line represent experimental values and theoretical calculation, respectively. (b) Optimal values of γ (green curve) and corresponding final random bit rates (red curve) in the cases of four sampling rates. At a sampling rate of 10 GSa/s, the random bit rate reaches 68 Gbps.

Gaussian distribution. This is done by an experiment whose procedure is as follows. The raw sampling data acquired in the oscilloscope is transferred to a computer for post-processing offline. A Matlab program in the computer reads the data of 10 million points each time. The program first sorts all the data, and finds the minimum and the maximum values to form the voltage range of $[V_{min}, V_{max}]$. Both data in the ranges of the top 0.1% and bottom 0.1% is manually set to the corresponding boundaries so that the effective range is changed to $[V_1, V_2]$. This effective range is further digitised with 8 bits corresponding to 256 bins, and all the remaining points are sorted out in these bins. In this way, the probability distribution of the raw data is formed and the bin that has the maximal probability can be easily found. Therefore, the min-entropy can be calculated. The relationship between γ and the min-entropy is shown as the solid line in Figure 7.4(a). The increase in the slope of min-entropy is steep when γ is small, but becomes rather flat when $\gamma > 5$.

In the cases of four sampling rates, the values of γ are measured as shown on the left y-axis of Figure 7.4(b), and the values of min-entropy are obtained as well. In the case of a 0.9 mW laser power and a 10 GSa/s sampling rate, the total voltage

variance is $\langle V(t)^2 \rangle = 5.24\ mV^2$ while the quantum part is $\sigma^2_{quantum} = 4.49\ mV^2$. The effective voltage range is 10.2 mV and the maximum probability is $P_{max} = 7.6 \times 10^{-3}$.

According to Equation (7.10), the min-entropy in this case is 7.04 bits per sample point or 0.88 bits per bit, implying that 7.04 random bits can be generated from each sample. At a sampling rate of 10 Gsa/s, the resulting random bit rate is 70.4 Gbps. A Toeplitz matrix hash function on the basis of the fast Fourier transform (FFT) [88] with a size of $n \times m$ ($n = 3.36 \times 10^7$ and $m = 2.88 \times 10^7$) is applied, implying that m final random bits are generated from n raw random bits. Therefore, the min-entropy is slightly decreased to 0.86 bits per bit (m/n) so that the final bit rate reaches 68 Gbps. Note that the real-time QRNG speed might be further limited by the implementation of data post-processing.

Compared with previous schemes on the basis of quantum phase fluctuations [97, 98] and other QRNG implementations [90–92, 101–106], the bit rate of our QRNG has been drastically increased. Since the values of γ are almost constant regardless of the sampling rates, the final random bit rate is linearly proportional to the sampling rate, as shown on the right y-axis of Figure 7.4(b).

7.4 Randomness Test

In the early development stage of RNG, many researchers were devoted to verifying randomness by examining the observed random bit strings. Unfortunately, a strict verification method for a RNG outputs does not exist, since it can never prevent a malicious device from outputting a predetermined string that passes all of the tests. From this point of view, true randomness can only exist in physical processes involving inherent randomness. Nevertheless, there exists statistical toolboxes one can use to test the randomness of RNG outputs with a high confidence from a statistical point of view.

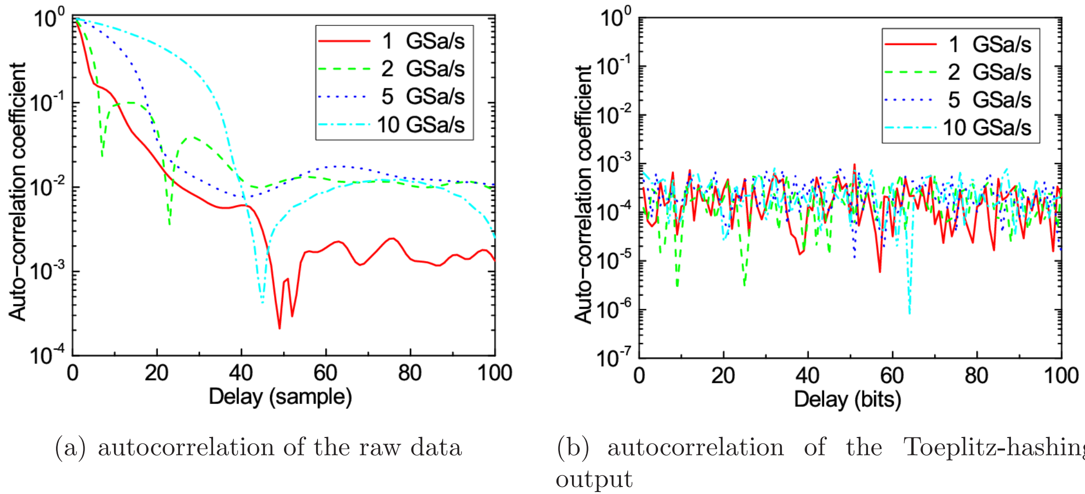

(a) autocorrelation of the raw data

(b) autocorrelation of the Toeplitz-hashing output

Figure 7.5: (a) The autocorrelation of raw data at different sampling rates. Data size of each file is 1×10^7 samples, and each sample comprises 8 bits. (b) The autocorrelations of the Toeplitz-hashing output. Data size of each file is 1×10^7 bits. The autocorrelations are substantially reduced by Toeplitz-hashing.

The autocorrelation diagrams of the raw data and the Toeplitz-hashing output are shown in Figure 7.5(a) and Figure 7.5(b). There are no significant differences among different sampling rates ranging from 1 GSa/s to 10 GSa/s. The autocorrelation of the raw data is caused by the following reason: in the experiment, the sampling rate is faster than the time delay between two arms of the interferometer. The result is consistent with theory and does not affect the randomness [99]. After Toeplitz-hashing, the autocorrelation is substantially reduced and consistent with the expectation, which indicates that Toeplitz-hashing is suitable for post-processing and the sampling rate ranging from 1 to 10 GSa/s is appropriate in the experimental setup.

To further test and verify the quality of the final output random bits, the standard NIST statistical tests [107] are implemented. The p-values and the proportions of all the test items in four cases are listed in Table 7.2. For the test items that produce multiple outcomes, a Kolmogorov-Smirnov (KS) uniformity test is further performed for the p-values, and the proportions are averaged. Clearly, all the data pass the NIST tests.

Table 7.2: The results of the standard NIST tests for final random bits. The data size of each bit string is 1 Gbit. In tests producing multiple outcomes, a Kolmogorov-Smirnov (KS) uniformity test has been further performed for p-values and the corresponding proportions are averaged. All the p-values are larger than 0.01 and all the proportions (PROP) are larger than 0.98, indicating that the random bits pass the NIST tests well.

Statistical test	1 GSa/s		2 GSa/s		5 GSa/s		10 GSa/s	
	P-value	PROP	P-value	PROP	P-value	PROP	P-value	PROP
Frequency	0.4731	0.991	0.6288	0.994	0.1209	0.987	0.6288	0.990
Block Frequency	0.5728	0.985	0.4172	0.991	0.2940	0.991	0.2925	0.992
Cumulative Sum	0.5667	0.988	0.3770	0.993	0.6662	0.985	0.4313	0.991
Runs	0.8360	0.986	0.9915	0.992	0.9932	0.992	0.6121	0.993
Longest Run	0.2983	0.992	0.5362	0.993	0.0401	0.986	0.0904	0.991
Rank	0.3299	0.992	0.1495	0.993	0.7792	0.990	0.2111	0.992
FFT	0.9335	0.983	0.0259	0.988	0.3056	0.989	0.5281	0.992
Non Overlapping	0.0662	0.990	0.0507	0.990	0.1331	0.990	0.0599	0.990
Overlapping	0.4065	0.991	0.6080	0.987	0.8963	0.987	0.0707	0.984
Universal	0.0366	0.992	0.1917	0.990	0.4885	0.987	0.7157	0.986
Approx. Entropy	0.0721	0.986	0.2417	0.988	0.0469	0.991	0.5141	0.994
Random Excursions (RE)	0.3666	0.991	0.2875	0.989	0.1214	0.989	0.3026	0.991
RE Variant	0.1849	0.991	0.1810	0.991	0.2557	0.987	0.1407	0.991
Serial	0.7439	0.994	0.6579	0.989	0.5997	0.990	0.6559	0.992
Linear Complexity	0.9229	0.992	0.3086	0.993	0.1816	0.990	0.5976	0.991

7.5 Conclusion

In conclusion, a 68-Gbps QRNG on the basis of quantum phase fluctuations has been demonstrated. This generation rate is one order of magnitude faster than the maximum previously obtained rate. With the help of feedback signals, the interferometer in the QRNG system is very stable, and no temperature control is required anymore. The calculation of the min-entropy and randomness of the raw data is modelled based on the experimental setup, and the autocorrelation of the raw data can be removed by applying the Toeplitz matrix hashing. The final generated random bits pass the standard NIST tests, indicating a good level of randomness. The QRNG scheme improves the generation rate dramatically compared to existing QRNG implementations and becomes a practical solution for some high-speed random number applications.

A physical RNG is naturally composed of two parts: the source of randomness and the means of measuring it. The source is the key part to ensure the quality of the random numbers, thus needs to be carefully calibrated to achieve information-theoretically proven randomness. Existing implementations of QRNGs indeed have relied on ad hoc quantum source models to quantify the source [99]. In practice, however, the source is a complicated physical system that can easily deviate from these theoretical models and affect the output randomness without control. To close this gap, a loss-tolerant source-independent QRNG has recently been proposed [108] with an output randomness that can be certified even when the source is uncharacterised or untrusted. Note that the loss tolerance is an important property because practical detectors usually have low efficiencies. The proposed protocol makes no assumptions about the dimensions of the source and takes account of practical issues, including loss and finite-key effects. It can also be viewed as an exponential random expansion scheme. In order to design a high-speed experimental setup to realise the source-independent QRNG scheme, both a reliable interferometer and a fast optical switch are required. With the development of DLW technology, such a task can be realized

in near future.

As aforementioned, the key element in the QRNG system is a stable interferometer. Currently, all interferometers are either free-space or fiber-based. The length difference between two paths in the interferometer is normally in the range of a few meters, and it is difficult to control the length accurately. An active feedback system or temperature control is needed to maintain phase drift over the experimental time. The implementation of interferometer using DLW is under investigation, which can be accurately controlled and has very stable performance. The potential application of the DLW technology in developing more compact and stable QRNG system is interesting and promising. Considerable progress has been made on intriguing applications of the DLW inscribed waveguide in crystalline materials, especially in the area of quantum photonics [9, 16, 17, 109, 110]. The advantages of the ultrafast DLW technology pave an efficient way to produce integrated circuits on chip scales for future QRNG, and show its powerful ability and unique capability in diverse waveguide-fabrication with high quality in dielectric materials.

Chapter 8

Summary

8.1 Conclusion

In summary, the work discussed in this dissertation explores how to fabricate and characterise optical waveguides with ultrafast direct laser writing (DLW). Specifically, it focuses on using a spatial light modulator (SLM) to actively correct aberrations during the fabrication process. Experimental results have shown that, compared with previous work, the quality of the waveguides can be dramatically improved by applying adaptive optics in the DLW system. Two different aberration correction techniques, the plasma emission sensing method and the Shack–Hartmann wavefront sensing method, have been explored and evaluated. Plasma emission sensing method is chosen because of its high-accuracy. The use of an SLM in a DLW system facilitates the manufacturing process of more complex and higher-quality three-dimensional (3D) waveguides, and adds more control of the beam shaping and geometry during fabrication. Equipment, fabrication procedures and control parameters of the DLW system have been explained in detail in order to fully understand the process.

By measuring the intensities of the near-field modes, refractive-index profiles of the fabricated waveguides have been well-evaluated using an improved propagation-

mode near-field method (PMNFM) and an equivalent-step-index (ESI) method. In addition, results of the quantitative phase microscopy have also provided valuable refractive-index information for the fabrication system. Although there are still a lot of limitations and challenges in predicting more accurate transmission characteristics, sufficient propagation properties of the waveguides have been obtained during the experiment.

With the understanding of the DLW system, waveguides written in different transparent materials have been successfully demonstrated with different structures and properties. Homogenous waveguides deep into fused silica glasses have been fabricated with adaptive optics. Aberration correction applied to the DLW system enables the demonstration of single-mode waveguides with circular cross-section over a significant depth range (>1 mm), while the accuracy of the fabrication position is maintained. In addition, the designed y-splitters can split the optical signal evenly based on the experiment. Results of the y-splitters and parallel writing show a bright future for fabrication of more complex 3D waveguides.

Two types of optical waveguides have been fabricated in the potassium dihydrogen phosphate (KDP) crystal by ultrafast laser pulses, for the first time to my knowledge. Unlike fused silica, type I waveguides can be easily damaged in KDP without aberration correction, and the pulse energy should be carefully controlled to obtain homogeneous refractive-index modifications. Conversely, type II waveguides can be created without much control at high pulse energies. However, the structures of the type II waveguides can be adaptively modified with an SLM in the DLW system, resulting in stronger mode-confinement. The polarisation sensitivity, thermal annealing effects and transmission properties of the written waveguides have been well-characterised, showing that high-quality waveguides can be obtained in KDP crystal. Type II waveguides have also been demonstrated with improved quality by aberration correction in $LiNbO_3$ crystal, whose refractive index is relatively high and

difficult to fabricate at greater depths.

Finally, a quantum random number generation (QRNG) system on the basis of quantum phase fluctuations have been presented with a high speed of 68 Gbps. This demonstration successfully increased the reported bit rate by one order of magnitude higher than the ones in the existing literature. The min-entropy has been used to evaluate the randomness of the raw data by a system model, followed by the Toeplitz hashing for randomness extraction. The key element in the QRNG system is an actively stabilized interferometer, which can be replaced by a more stable and compact DLW written interferometer in the near future.

8.2 Outlook

Ultrafast DLW of waveguides in transparent materials offers a promising future for 3D optical device fabrication. The advantages of ultrafast DLW with respect to time, cost, flexibility and 3D capability continuously inspire more research interest in the area. As technology moves forward, increasing attention is received and more applications of the ultrafast laser fabrication will be discovered.

Limited by the equipment (stages, photodetector, laser sources) used for waveguide characterisation, the propagation losses of the waveguides have not been accurately measured in the project. Research funding has been obtained and the experimental setup will soon be improved by higher-quality equipment. It is important to obtain more reliable data with better equipment, which will provide more accurate understanding of the optical properties of the waveguides using the DLW technique.

Further optimisation of the DLW system can be applied by incorporating the technique with more understanding of the fabrication parameters. Different qualities and characteristics of the written waveguide can be demonstrated with the effect of different parameters. Research and experimental work so far have been focused on the

direct fabrication and characterisation of optical waveguides by adjusting parameters manually. For future work, the goal is to explore the detail relationship between the control parameters (pulse energy, focus shape, scan speed, etc.) and the refractive-index modification. The objective of building a modelling-fabrication-characterisation cycle for a high-confidence well-characterised fabrication process is of great interest.

Experiment has shown that the adaptive optics can improve the performance of the DLW system. Future investigation can be done to fabricate optical waveguides with more complicated structures, such as mode convertors, electro-optic modulators, frequency converters. Potential applications in integrated optics, quantum information circuits, optical communications and optical storage should also be explored in future work. Further improvement is under investigation to implement the laser-written interferometer in quantum random generation. The main challenge faced in the QRNG design is a stable interferometer and the DLW technique can be a potential solution. Unfortunately, because of the lack of facilities, no I/O interference could be made for the interferometer in the waveguide sample to be compatible with the other components in the QRNG system.

Additional work on parallel and multi-spot writing should be also conducted. Simply parallel writing has been demonstrated but more research needs to be performed, especially on the design of hologram algorithms considering depth-dependent aberration. In the experiment, aberrations have been reduced by applying proper holograms while retaining the degree of parallelization.

The study of DLW fabrication in different transparent materials will undoubtedly continue. One of the greatest advantages of the DLW approach is that by simply changing the control parameters instead of the experimental setup, waveguides can be directly written in different substrates. This will make flexible fabrication in compound substrates possible, showing great future for integrated optics.

Bibliography

[1] K. M. Davis, K. Miura, N. Sugimoto, and K. Hirao, "Writing waveguides in glass with a femtosecond laser," *Optics Letters*, vol. 21, no. 21, pp. 1729–1731, 1996.

[2] S. Nolte, M. Will, J. Burghoff, and A. Tuennermann, "Femtosecond waveguide writing: a new avenue to three-dimensional integrated optics," *Applied Physics A*, vol. 77, no. 1, pp. 109–111, 2003.

[3] F. Chen and J. R. V. de Aldana, "Optical waveguides in crystalline dielectric materials produced by femtosecond-laser micromachining," *Laser & Photonics Reviews*, vol. 8, no. 2, pp. 251–275, 2014.

[4] D. Du, X. Liu, G. Korn, J. Squier, and G. Mourou, "Laser-induced breakdown by impact ionization in sio2 with pulse widths from 7 ns to 150 fs," *Applied Physics Letters*, vol. 64, no. 23, 1994.

[5] I.-B. Sohn, M.-S. Lee, and J.-Y. Chung, "Fabrication of optical splitter and passive alignment technique with a femtosecond laser," *Photonics Technology Letters, IEEE*, vol. 17, no. 11, pp. 2349–2351, 2005.

[6] J. Liu, Z. Zhang, S. Chang, C. Flueraru, and C. P. Grover, "Directly writing of 1-to-n optical waveguide power splitters in fused silica glass using a femtosecond laser," *Optics Communications*, vol. 253, no. 4–6, pp. 315–319, 2005.

[7] D. Grobnic, S. Mihailov, C. Smelser, M. Becker, and M. Rothhardt, "Femtosecond laser fabrication of bragg gratings in borosilicate ion-exchange waveguides," *Photonics Technology Letters, IEEE*, vol. 18, no. 13, pp. 1403–1405, 2006.

[8] P. Herman, "Direct femtosecond laser writing of 3-d waveguides and gratings for optical communications," in *Optical Fiber Communication Conference/National Fiber Optic Engineers Conference*, p. OThV4, Optical Society of America, 2008.

[9] G. D. Marshall, A. Politi, J. C. F. Matthews, P. Dekker, M. Ams, M. J. Withford, and J. L. O'Brien, "Laser written waveguide photonic quantum circuits," *Optics Express*, vol. 17, no. 15, pp. 12546–12554, 2009.

[10] M. Sakakura, T. Sawano, Y. Shimotsuma, K. Miura, and K. Hirao, "Fabrication of three-dimensional 1 x 4 splitter waveguides inside a glass substrate with spatially phase modulated laser beam," *Optics Express*, vol. 18, no. 12, pp. 12136–12143, 2010.

[11] G. Cerullo, "Femtosecond-laser-written optical waveguides for optical communications and biophotonic applications," in *Lasers and Electro-Optics and the European Quantum Electronics Conference*, 2009.

[12] D. Miller, "Rationale and challenges for optical interconnects to electronic chips," *Proceedings of the IEEE*, vol. 88, no. 6, pp. 728–749, 2000.

[13] E. N. Glezer, M. Milosavljevic, L. Huang, R. J. Finlay, T.-H. Her, J. P. Callan, and E. Mazur, "Three-dimensional optical storage inside transparentmaterials," *Optics Letters*, vol. 21, no. 24, pp. 2023–2025, 1996.

[14] K. Miura, J. Qiu, S. Fujiwara, S. Sakaguchi, and K. Hirao, "Three-dimensional optical memory with rewriteable and ultrahigh density using the valence-state change of samarium ions," *Applied Physics Letters*, vol. 80, no. 13, 2002.

[15] A. Politi, M. J. Cryan, J. G. Rarity, S. Yu, and J. L. O'Brien, "Silica-on-silicon waveguide quantum circuits," *Science*, vol. 320, no. 5876, pp. 646–649, 2008.

[16] A. Crespi, R. Osellame, R. Ramponi, L. Sansoni, F. Sciarrino, and P. Mataloni, "Femtosecond laser written photonic circuits for quantum simulation," in *Lasers and Electro-Optics Europe and International Quantum Electronics Conference*, 2013.

[17] A. W. Schell, J. Kaschke, J. Fischer, R. Henze, J. Wolters, M. Wegener, and O. Benson, "Three-dimensional quantum photonic elements based on single nitrogen vacancy-centres in laser-written microstructures," *Scientific Reports*, vol. 3, 2013.

[18] K. O. Hill, Y. Fujii, D. C. Johnson, and B. S. Kawasaki, "Photosensitivity in optical fiber waveguides: Application to reflection filter fabrication," *Applied Physics Letters*, vol. 32, no. 10, 1978.

[19] R. F. Kydd and F. J. Bryant, "The photosensitivity of cadmium telluride," *Physica Status Solidi A*, vol. 23, no. 1, pp. K49–K54, 1974.

[20] S. C. Jones, P. Braunlich, R. T. Casper, X.-A. Shen, and P. Kelly, "Recent progress on laser-induced modifications and intrinsic bulk damage of wide-gap optical materials," *Optical Engineering*, vol. 28, no. 10, p. 281039, 1989.

[21] B. C. Stuart, M. D. Feit, S. Herman, A. M. Rubenchik, B. W. Shore, and M. D. Perry, "Nanosecond-to-femtosecond laser-induced breakdown in dielectrics," *Physics Review B*, vol. 53, pp. 1749–1761, 1996.

[22] C. B. Schaffer, A. Brodeur, and E. Mazur, "Laser-induced breakdown and damage in bulk transparent materials induced by tightly focused femtosecond laser pulses," *Measurement Science and Technology*, vol. 12, no. 11, p. 1784, 2001.

[23] W. G. Roeterdink, L. B. F. Juurlink, O. P. H. Vaughan, J. Dura Diez, M. Bonn, and A. W. Kleyn, "Coulomb explosion in femtosecond laser ablation of si(111)," *Applied Physics Letters*, vol. 82, no. 23, 2003.

[24] D. Ashkenasi, G. Mller, A. Rosenfeld, R. Stoian, I. Hertel, N. Bulgakova, and E. Campbell, "Fundamentals and advantages of ultrafast micro-structuring of transparent materials," *Applied Physics A*, vol. 77, no. 2, pp. 223–228, 2003.

[25] G. D. Valle, R. Osellame, and P. Laporta, "Micromachining of photonic devices by femtosecond laser pulses," *Journal of Optics A: Pure and Applied Optics*, vol. 11, no. 1, p. 013001, 2009.

[26] D. Homoelle, S. Wielandy, A. L. Gaeta, N. F. Borrelli, and C. Smith, "Infrared photosensitivity in silica glasses exposed to femtosecond laser pulses," *Optics Letters*, vol. 24, no. 18, pp. 1311–1313, 1999.

[27] D. Grobnic, S. Mihailov, C. Smelser, F. Genereux, G. Baldenberger, and R. Vallee, "Bragg gratings made in reverse proton exchange lithium niobate waveguides with a femtosecond ir laser and a phase mask," *Photonics Technology Letters, IEEE*, vol. 17, no. 7, pp. 1453–1455, 2005.

[28] J. Burghoff, S. Nolte, and A. Tünnermann, "Origins of waveguiding in femtosecond laser-structured $LiNbo_3$," *Applied Physics A*, vol. 89, no. 1, pp. 127–132, 2007.

[29] L. Gui, B. Xu, and T. C. Chong, "Microstructure in lithium niobate by use of focused femtosecond laser pulses," *Photonics Technology Letters, IEEE*, vol. 16, no. 5, pp. 1337–1339, 2004.

[30] V. Mizeikis, V. Purlys, L. Maigyte, K. Staliunas, and S. Juodkazis, "Direct laser writing and applications of dielectric microstructures with low refractive index contrast," 2011.

[31] D. Paipulas, V. Kudriašov, M. Malinauskas, V. Smilgevičius, and V. Sirutkaitis, "Diffraction grating fabrication in lithium niobate and kdp crystals with femtosecond laser pulses," *Applied Physics A*, vol. 104, no. 3, pp. 769–773, 2011.

[32] C. R. Pollock, *Fundamentals of Optoelectronics*. McGraw-Hill Inc., 1994.

[33] H. M. Presby, W. Mammel, and R. M. Derosier, "Refractive index profiling of graded index optical fibers," *Review of Scientific Instruments*, vol. 47, pp. 348–352, 1976.

[34] M. Tateda, "Single-mode-fiber refractive-index profile measurement by reflection method," *Applied Optics*, vol. 17, no. 3, pp. 475–478, 1978.

[35] K. White, "Practical application of the refracted near-field technique for the measurement of optical fibre refractive index profiles," *Optical and Quantum Electronics*, vol. 11, no. 2, pp. 185–196, 1979.

[36] D. Marcuse and H. M. Presby, "Index profile measurements of fibers and their evaluation," *Proceedings of the IEEE*, vol. 68, no. 6, pp. 666–688, 1980.

[37] K. Morishita, "Refractive-index-profile determination of single-mode optical fibers by a propagation-mode near-field scanning technique," *Journal of Lightwave Technology*, vol. 1, no. 3, pp. 445–449, 1983.

[38] M. Ikeda, M. Tateda, and H. Yoshikiyo, "Refractive index profile of a graded index fiber: Measurement by a reflection method," *Applied Optics*, vol. 14, no. 4, pp. 814–815, 1975.

[39] K. Morishita, "Measurement of refractive-index profile of single-mode optical fibers by the propagation-mode near-field method," *Journal of Lightwave Technology*, vol. 3, no. 2, pp. 244–247, 1985.

[40] K. Morishita, "Index profiling of three-dimensional optical waveguides by the propagation-mode near-field method," *Journal of Lightwave Technology*, vol. 4, no. 8, pp. 1120–1124, 1986.

[41] Y. Wu, *Planar waveguides of Y2O3, Y2O3 Tb3+ and YAG prepared by sol-gel analysis, structure and optical*. PhD thesis, Claude Bernard University, 2005.

[42] G. Cerullo, R. Osellame, S. Taccheo, M. Marangoni, D. Polli, R. Ramponi, P. Laporta, and S. D. Silvestri, "Femtosecond micromachining of symmetric waveguides at 1.5 µm by astigmatic beam focusing," *Optics Letters*, vol. 27, no. 21, pp. 1938–1940, 2002.

[43] M. Ams, G. D. Marshall, D. J. Spence, and M. J. Withford, "Slit beam shaping method for femtosecond laser direct-write fabrication of symmetric waveguides in bulk glasses," *Opt. Express*, vol. 13, pp. 5676–5681, Jul 2005.

[44] Y. Nasu, M. Kohtoku, and Y. Hibino, "Low-loss waveguides written with a femtosecond laser for flexible interconnection in a planar light-wave circuit," *Opt. Lett.*, vol. 30, pp. 723–725, Apr 2005.

[45] R. R. Thomson, A. S. Bockelt, E. Ramsay, S. Beecher, A. H. Greenaway, A. K. Kar, and D. T. Reid, "Shaping ultrafast laser inscribed optical waveguides using a deformable mirror," *Opt. Express*, vol. 16, pp. 12786–12793, Aug 2008.

[46] P. S. Salter, A. Jesacher, J. B. Spring, B. J. Metcalf, N. Thomas-Peter, R. D. Simmonds, N. K. Langford, I. A. Walmsley, and M. J. Booth, "Adaptive slit beam shaping for direct laser written waveguides," *Optics Letters*, vol. 37, no. 4, pp. 470–472, 2012.

[47] R. D. Leonardo, F. Ianni, and G. Ruocco, "Computer generation of optimal holograms for optical trap arrays," *Optics Express*, vol. 15, no. 4, pp. 1913–1922, 2007.

[48] A. Jesacher and M. J. Booth, "Parallel direct laser writing in three dimensions with spatially dependentaberration correction," *Optics Express*, vol. 18, no. 20, pp. 21090–21099, 2010.

[49] E. H. Waller, M. Renner, and G. von Freymann, "Active aberration- and point-spread-function control in direct laser writing," *Optics Express*, vol. 20, no. 22, pp. 24949–24956, 2012.

[50] R. W. Bowman, A. J. Wright, and M. J. Padgett, "An SLM-based Shack–Hartmann wavefront sensor for aberration correction in optical tweezers," *Journal of Optics*, vol. 12, no. 12, p. 124004, 2010.

[51] P. S. Salter, Z. Iqbal, and M. J. Booth, "Analysis of the three-dimensional focal positioning capability of adaptive optic elements," *International Journal of Optomechatronics*, vol. 7, no. 1, pp. 1–14, 2013.

[52] A. Jesacher, G. D. Marshall, T. Wilson, and M. J. Booth, "Adaptive optics for direct laser writing with plasma emission aberration sensing," *Optics Express*, vol. 18, no. 2, pp. 656–661, 2010.

[53] L. Huang and F. Payne, "Determination of the equivalent step index of direct laser written waveguides," 2014.

[54] P. S. Salter, A. Jesacher, L. Huang, X. Liu, M. Baum, I. Alexeev, M. Schmidt, and M. J. Booth, "Structural analysis of direct laser written waveguides," 2014.

[55] A. M. Streltsov and N. F. Borrelli, "Fabrication and analysis of a directional coupler written in glass by nanojoule femtosecond laser pulses," *Optics Letters*, vol. 26, no. 1, pp. 42–43, 2001.

[56] H. S. MacKenzie, *Evanescent-Field Devices for Non-Linear Optical Applications*. PhD thesis, University of Cambridge, 1990.

[57] A. Savitzky and M. J. E. Golay, "Smoothing and differentiation of data by simplified least squares procedures.," *Analytical Chemistry*, vol. 36, no. 8, pp. 1627–1639, 1964.

[58] R. W. Shafer, "What is a savitzky-golay filter," in *IEEE Signal Processing Magazine*, p. 111, 2011.

[59] A. W. Snyder and R. A. Sammut, "Fundamental (HE11) modes of graded optical fibers," *Journal of the Optical Society of America*, vol. 69, no. 12, pp. 1663–1671, 1979.

[60] K. Okamoto, *Fundamentals of Optical Waveguides.* 2nd ed., 2006.

[61] M. Miyagi and S. Nishida, "An approximate formula for describing dispersion properties of optical dielectric slab and fiber waveguides," *Journal of the Optical Society of America*, vol. 69, no. 2, pp. 291–293, 1979.

[62] M. R. Teague, "Irradiance moments: their propagation and use for unique retrieval of phase," *Journal of the Optical Society of America*, vol. 72, no. 9, pp. 1199–1209, 1982.

[63] M. R. Teague, "Deterministic phase retrieval: a green's function solution," *Journal of the Optical Society of America*, vol. 73, no. 11, pp. 1434–1441, 1983.

[64] K. A. Nugent, "The measurement of phase through the propagation of intensity: an introduction," *Contemporary Physics*, vol. 52, no. 1, pp. 55–69, 2011.

[65] A. Jesacher, P. S. Salter, and M. J. Booth, "Refractive index profiling of direct laser written waveguides: tomographic phase imaging," *Optics Material Express*, vol. 3, no. 9, pp. 1223–1232, 2013.

[66] L. Huang, P. Salter, F. Payne, and M. Booth, "Laser written waveguides at depths over 1mm using adaptive optics," *Optics Materials Express (Manuscript in Preparation)*, 2015.

[67] B. P. Cumming, M. D. Turner, G. E. Schröder-Turk, S. Debbarma, B. Luther-Davies, and M. Gu, "Adaptive optics enhanced direct laser writing of high refractive index gyroid photonic crystals in chalcogenide glass," *Optics Express*, vol. 22, no. 1, pp. 689–698, 2014.

[68] D. Marcuse, "Curvature loss formula for optical fibers," *Journal of the Optical Society of America*, vol. 66, no. 3, pp. 216–220, 1976.

[69] L. Huang, P. Salter, M. Karpiński, B. Smith, F. Payne, and M. Booth, "Waveguide fabrication in KDP crystals with femtosecond laser pulses," *Applied Physics A*, vol. 118, no. 3, pp. 831–836, 2015.

[70] M. Karpiński, L. Huang, P. S. Salter, B. Smith, F. Payne, and M. J. Booth, "Second harmonic generation of optical waveguides in KDP crystals," *Optics Express (Manuscript in Preparation)*, 2015.

[71] R. R. Gattass and E. Mazur, "Femtosecond laser micromachining in transparent materials," *Nature Photonics*, vol. 2, pp. 219–225, 2008.

[72] A. M. Kowalevicz, V. Sharma, E. P. Ippen, J. G. Fujimoto, and K. Minoshima, "Three-dimensional photonic devices fabricated in glass by use of a femtosecond laser oscillator," *Optics Letters*, vol. 30, no. 9, pp. 1060–1062, 2005.

[73] A. M. Streltsov and N. F. Borrelli, "Study of femtosecond-laser-written waveguides in glasses," *Journal of the Optical Society of America B*, vol. 19, no. 10, pp. 2496–2504, 2002.

[74] R. D. Simmonds, P. S. Salter, A. Jesacher, and M. J. Booth, "Three dimensional laser microfabrication in diamond using a dual adaptive optics system," *Optics Express*, vol. 19, no. 24, pp. 24122–24128, 2011.

[75] G. Salamu, F. Jipa, M. Zamfirescu, and N. Pavel, "Laser emission from diode-pumped Nd:YAG ceramic waveguide lasers realized by direct femtosecond-laser writing technique," *Optics Express*, vol. 22, no. 5, pp. 5177–5182, 2014.

[76] A. Benayas, W. F. Silva, C. Jacinto, E. Cantelar, J. Lamela, F. Jaque, J. R. V. de Aldana, G. A. Torchia, L. Roso, A. A. Kaminskii, and D. Jaque, "Thermally resistant waveguides fabricated in Nd:YAG ceramics by crossing femtosecond damage filaments," *Optics Letters*, vol. 35, no. 3, pp. 330–332, 2010.

[77] M. Hentschel, H. Hübel, A. Poppe, and A. Zeilinger, "Three-color Sagnac source of polarization-entangled photon pairs," *Optics Express*, vol. 17, no. 25, pp. 23153–23159, 2009.

[78] Z. Huang, C. Tu, S. Zhang, Y. Li, F. Lu, Y. Fan, and E. Li, "Femtosecond second-harmonic generation in periodically poled lithium niobate waveguides written by femtosecond laser pulses," *Optics Letters*, vol. 35, no. 6, pp. 877–879, 2010.

[79] R. R. Thomson, S. Campbell, I. J. Blewett, A. K. Kar, and D. T. Reid, "Optical waveguide fabrication in z-cut lithium niobate ($LiNbO_3$) using femtosecond pulses in the low repetition rate regime," *Applied Physics Letters*, vol. 88, no. 11, p. 111109, 2006.

[80] R. Osellame, M. Lobino, N. Chiodo, M. Marangoni, G. Cerullo, R. Ramponi, H. T. Bookey, R. R. Thomson, N. D. Psaila, and A. K. Kar, "Femtosecond laser writing of waveguides in periodically poled lithium niobate preserving the nonlinear coefficient," *Applied Physics Letters*, vol. 90, no. 24, 2007.

[81] S. N. J. Thomas, M. Heinrich and A. Tünnermann, "Laser direct writing: Enabling monolithic and hybrid integrated solutions on the lithium niobate platform," *Physica Status Solidi A*, vol. 208, no. 2, pp. 276–283, 2011.

[82] E. Neyra, S. Suarez, and G. A. Torchia, "Light coupling in single-track guiding structures obtained by femtosecond laser writing in lithium niobate," *Optics Letters*, vol. 39, no. 5, pp. 1125–1128, 2014.

[83] P. J. Mosley, J. S. Lundeen, B. J. Smith, and I. A. Walmsley, "Conditional preparation of single photons using parametric downconversion: a recipe for purity," *New Journal of Physics*, vol. 10, no. 9, p. 093011, 2008.

[84] P. J. Mosley, J. S. Lundeen, B. J. Smith, P. Wasylczyk, A. B. U'Ren, C. Silberhorn, and I. A. Walmsley, "Heralded generation of ultrafast single photons in pure quantum states," *Physical Review Letters*, vol. 100, p. 133601, 2008.

[85] M. Heinrich, K. Rademaker, and S. Nolte, *Femtosecond-laser micromachining: Photonic and Microfluidic Devices in Transparent Materials*, ch. 11. Springer, Berlin, 2012.

[86] W. Yang, P. G. Kazansky, and Y. P. Svirko, "Non-reciprocal ultrafast laser writing," *Nature Photonics*, pp. 99–104, Jan 2008.

[87] Y.-Q. Nie, L. Huang, Y. Liu, F. Payne, J. Zhang, and J.-W. Pan, "The generation of 68 Gbps quantum random number by measuring laser phase fluctuations," *Review of Scientific Instruments*, vol. 86, no. 6, p. 063105, 2015.

[88] X. Ma, F. Xu, H. Xu, X. Tan, B. Qi, and H.-K. Lo, "Postprocessing for quantum random-number generators: Entropy evaluation and randomness extraction," *Physical Review A*, vol. 87, p. 062327, 2013.

[89] X. Yuan, H. Zhou, Z. Cao, and X. Ma, "Inherent randomness as a measure of quantum coherence," *ArXiv e-prints*, 2015.

[90] J. G. Rarity, P. Owens, and P.R.Tapster, "Quantum random-number generation and key sharing," *Journal of Modern Optics*, vol. 41, no. 12, pp. 2435–2444, 1994.

[91] A. Stefanov, N. Gisin, O. Guinnard, L. Guinnard, and H. Zbinden, "Optical quantum random number generator," *Journal of Modern Optics*, vol. 47, no. 4, pp. 595–598, 2000.

[92] T. Jennewein, U. Achleitner, G. Weihs, H. Weinfurter, and A. Zeilinger, "A fast and compact quantum random number generator," *Review of Scientific Instruments*, vol. 71, no. 4, pp. 1675–1680, 2000.

[93] H. Takesue, E. Diamanti, C. Langrock, M. M. Fejer, and Y. Yamamoto, "10-Ghz clock differential phase shift quantum key distribution experiment," *Optics Express*, vol. 14, no. 20, pp. 9522–9530, 2006.

[94] C. Gabriel, C. Wittmann, C. Marquardt, and G. Leuchs, "A generator for unique quantum random numbers based on vacuum states," *Nature Photonics*, vol. 4, pp. 711–715, 2010.

[95] T. Symul, S. M. Assad, and P. K. Lam, "Real time demonstration of high bitrate quantum random number generation with coherent laser light," *Applied Physics Letters*, vol. 98, no. 23, 2011.

[96] M. Jofre, M. Curty, F. Steinlechner, G. Anzolin, J. P. Torres, M. W. Mitchell, and V. Pruneri, "True random numbers from amplified quantum vacuum," *Optics Express*, vol. 19, no. 21, pp. 20665–20672, 2011.

[97] B. Qi, Y.-M. Chi, H.-K. Lo, and L. Qian, "High-speed quantum random number generation by measuring phase noise of a single-mode laser," *Optics Letters*, vol. 35, no. 3, pp. 312–314, 2010.

[98] F. Xu, B. Qi, X. Ma, H. Xu, H. Zheng, and H.-K. Lo, "Ultrafast quantum random number generation based on quantum phase fluctuations," *Optics Express*, vol. 20, no. 11, pp. 12366–12377, 2012.

[99] H. Zhou, X. Yuan, and X. Ma, "Randomness generation based on spontaneous emissions of lasers," *Physical Review A*, vol. 91, p. 062316, 2015.

[100] A. Uchida, K. Amano, M. Inoue, K. Hirano, S. Naito, H. Someya, I. Oowada, T. Kurashige, M. Shiki, S. Yoshimori, *et al.*, "Fast physical random bit generation with chaotic semiconductor lasers," *Nature Photonics*, vol. 2, no. 12, pp. 728–732, 2008.

[101] H.-Q. Ma, Y. Xie, and L.-A. Wu, "Random number generation based on the time of arrival of single photons," *Applied Optics*, vol. 44, no. 36, pp. 7760–7763, 2005.

[102] M. A. Wayne, E. R. Jeffrey, G. M. Akselrod, and P. G. Kwiat, "Photon arrival time quantum random number generation," *Journal of Modern Optics*, vol. 56, no. 4, pp. 516–522, 2009.

[103] M. A. Wayne and P. G. Kwiat, "Low-bias high-speed quantum random number generator via shaped optical pulses," *Optics Express*, vol. 18, no. 9, pp. 9351–9357, 2010.

[104] M. Wahl, M. Leifgen, M. Berlin, T. Rohlicke, H.-J. Rahn, and O. Benson, "An ultrafast quantum random number generator with provably bounded output bias based on photon arrival time measurements," *Applied Physics Letters*, vol. 98, no. 17, 2011.

[105] S. Li, L. Wang, L.-A. Wu, H.-Q. Ma, and G.-J. Zhai, "True random number generator based on discretized encoding of the time interval between photons," *Journal of the Optical Society of America A*, vol. 30, no. 1, pp. 124–127, 2013.

[106] Y.-Q. Nie, H.-F. Zhang, Z. Zhang, J. Wang, X. Ma, J. Zhang, and J.-W. Pan, "Practical and fast quantum random number generation based on photon arrival time relative to external reference," *Applied Physics Letters*, vol. 104, no. 5, 2014.

[107] J. D. A. Rukhin, J. Soto and S. Vo, "A statistical test suite for random and pseudorandom number generators for cryptographic application," NIST Special Publication 800–22, Revision 1a, NIST, 2010.

[108] X. Ma, Z. Cao, and X. Yuan, "Source-independent quantum random number generation," *arXiv preprint arXiv:1508.04880*, 2015.

[109] Z. Chaboyer, T. Meany, L. Helt, M. Steel, and M. J. Withford, "Laser written multiport quantum circuits," in *SPIE OPTO*, vol. 93770Y, International Society for Optics and Photonics, 2015.

[110] N. Chiodo, G. D. Valle, R. Osellame, S. Longhi, G. Cerullo, R. Ramponi, P. Laporta, and U. Morgner, "Imaging of bloch oscillations in erbium-doped curved waveguide arrays," *Optics Letters*, vol. 31, no. 11, pp. 1651–1653, 2006.